NAVAL POSTGRADUATE SCHOOL

MONTEREY, CALIFORNIA

THESIS

NPSAT1 MEMS 3-AXIS RATE SENSOR SUITE PERFORMANCE, CHARACTERIZATION, AND FLIGHT UNIT ACCEPTANCE TESTING

by

Veronica V. Badescu

September 2011

Thesis Advisor:	James Horning
Second Reader:	James H. Newman

Approved for public release; distribution is unlimited

THIS PAGE INTENTIONALLY LEFT BLANK

REPORT DOCUMENTATION PAGE			Form Approved OMB No. 0704–0188

Public reporting burden for this collection of information is estimated to average 1 hour per response, including the time for reviewing instruction, searching existing data sources, gathering and maintaining the data needed, and completing and reviewing the collection of information. Send comments regarding this burden estimate or any other aspect of this collection of information, including suggestions for reducing this burden, to Washington headquarters Services, Directorate for Information Operations and Reports, 1215 Jefferson Davis Highway, Suite 1204, Arlington, VA 22202–4302, and to the Office of Management and Budget, Paperwork Reduction Project (0704–0188) Washington DC 20503.

1. AGENCY USE ONLY *(Leave blank)*	2. REPORT DATE September 2011	3. REPORT TYPE AND DATES COVERED Master's Thesis

4. TITLE AND SUBTITLE NPSAT1 MEMS 3-AXIS Rate Sensor Suite Performance, Characterization, and Flight Unit Acceptance Testing	5. FUNDING NUMBERS
6. AUTHOR(S) Veronica V. Badescu	
7. PERFORMING ORGANIZATION NAME(S) AND ADDRESS(ES) Naval Postgraduate School Monterey, CA 93943–5000	8. PERFORMING ORGANIZATION REPORT NUMBER
AGENCY NAME(S) AND ADDRESS(ES) N/A	10. SPONSORING/MONITORING AGENCY REPORT NUMBER

11. SUPPLEMENTARY NOTES The views expressed in this thesis are those of the author and do not reflect the official policy or position of the Department of Defense or the U.S. Government. IRB Protocol number NA.

12a. DISTRIBUTION / AVAILABILITY STATEMENT Approved for public release; distribution is unlimited	12b. DISTRIBUTION CODE A

13. ABSTRACT (maximum 200 words)

NPSAT1 is a small satellite providing education and hands-on experience to NPS students; it also serves as a platform for small satellite technology proof-of-concept demonstrations and experiments. One of these experiments is the MEMS rate sensor experiment. Comprising a triad of COTS MEMS devices, this experiment will use the MEMS rate sensors to measure angular rates for NPSAT1.

The NPSAT1 MEMS 3-Axis rate sensor was originally characterized and tested in 2007. Subsequently, the decision was made to fly the MEMS subsystem unpressurized. This new requirement, along with the replacement of a damaged sensor, necessitated the recalibration of the MEMS subsystem.

In addition, the rate compensation algorithm has been updated by determining the systematic errors of the subsystem—bias, thermal and pressure in-run drift, scale factor errors, and nonorthogonality through thermal ramp tests and rate transfer tests. Furthermore, other inertial sensor error sources such as hysteresis, repeatability, run-to-run error, and noise have been investigated. Acceptance testing was also performed to investigate vibration sensitivity and screen for workmanship defects.

The performance and characterization results verify that the MEMS subsystem is able to meet the flight requirements for rates >0.1°/sec, while the acceptance tests demonstrate the robustness and reliability of the unit.

14. SUBJECT TERMS NPSAT1, Small Satellites, Micro-Electro-Mechanical Systems, MEMS, COTS, Rate Sensors, Calibration, Sensor Errors	15. NUMBER OF PAGES 187
	16. PRICE CODE

17. SECURITY CLASSIFICATION OF REPORT	18. SECURITY CLASSIFICATION OF THIS PAGE	19. SECURITY CLASSIFICATION OF ABSTRACT	20. LIMITATION OF ABSTRACT
Unclassified	Unclassified	Unclassified	UU

NSN 7540–01–280–5500

Standard Form 298 (Rev. 2–89)
Prescribed by ANSI Std. 239–18

THIS PAGE INTENTIONALLY LEFT BLANK

Approved for public release; distribution is unlimited

NPSAT1 MEMS 3-AXIS RATE SENSOR SUITE PERFORMANCE, CHARACTERIZATION, AND FLIGHT UNIT ACCEPTANCE TESTING

Veronica V. Badescu
Civilian, United States Navy
B.S., University of Washington, 2003

Submitted in partial fulfillment of the
requirements for the degree of

MASTER OF SCIENCE IN SPACE SYSTEMS OPERATIONS

from the

NAVAL POSTGRADUATE SCHOOL
September 2011

Author: Veronica V. Badescu

Approved by: James Horning
Thesis Advisor

Dr. James H. Newman
Second Reader

Dr. Rudolf Panholzer
Chair, Space Systems Academic Group

THIS PAGE INTENTIONALLY LEFT BLANK

ABSTRACT

NPSAT1 is a small satellite providing education and hands-on experience to NPS students; it also serves as a platform for small satellite technology proof-of-concept demonstrations and experiments. One of these experiments is the MEMS rate sensor experiment. Comprising a triad of COTS MEMS devices, this experiment will use the MEMS rate sensors to measure angular rates for NPSAT1.

The NPSAT1 MEMS 3-Axis rate sensor was originally characterized and tested in 2007. Subsequently, the decision was made to fly the MEMS subsystem unpressurized. This new requirement, along with the replacement of a damaged sensor, necessitated the recalibration of the MEMS subsystem.

In addition, the rate compensation algorithm has been updated by determining the systematic errors of the subsystem—bias, thermal and pressure in-run drift, scale factor errors, and nonorthogonality through thermal ramp tests and rate transfer tests. Furthermore, other inertial sensor error sources such as hysteresis, repeatability, run-to-run error, and noise have been investigated. Acceptance testing was also performed to investigate vibration sensitivity and screen for workmanship defects.

The performance and characterization results verify that the MEMS subsystem is able to meet the flight requirements for rates >0.1°/sec, while the acceptance tests demonstrate the robustness and reliability of the unit.

THIS PAGE INTENTIONALLY LEFT BLANK

TABLE OF CONTENTS

I. INTRODUCTION....1
A. BACKGROUND....1
B. NPSAT1 OVERVIEW....2
C. COTS MICRO-ELECTROMECHANICAL 3-AXIS RATE SENSOR EXPERIMENT, REQUIREMENTS REVIEW AND UPDATE....7
1. Performance Requirements....7
a. Rate Performance Requirements....7
b. Temperature Performance Requirements....7
c. BIT Performance Requirements....8
2. Operational Requirements....8
a. Vibration Requirements....8
b. Thermal Requirements....10
c. Radiation Requirements....10
d. Vacuum Pressure Decay....10
e. Input Requirements....11
f. Output Requirements....11
D. ACS, MEMS, AND C&DH OPERATION....11

II. MICROMACHINED VIBRATORY GYROSCOPES....15
A. BEI SYSTRON DONNER QRS11 SENSOR....15
B. ERROR SOURCES....16
1. General Error Sources....17
2. MEMS Inertial Sensor Errors....17
a. Bias....18
b. Scale Factor....19
c. Nonorthogonality/Misalignment....20
C. GYROSCOPE ERROR COMPENSATION....20

III. TEST PREPARATIONS....23
A. TEST UNIT DESCRIPTION AND CHANGES....23
B. TEST FLOW....25
C. TEST EQUIPMENT....27
1. Hardware....27
2. Software....28
D. DATA FLOW....28

IV. PERFORMANCE AND ACCEPTANCE EVALUATION TESTS....31
A. STARTUP PROFILE AND SHORT TERM BIAS TESTING....32
B. NOMINAL VOLTAGE TESTS....34
1. Setup....35
2. Results....36
3. Limitations of Temperature Model....38
C. THERMAL RAMP TESTING IN AMBIENT PRESSURE....40
1. Setup....40

a. Thermal Vacuum Chamber Setup *40*
b. Cold Plate and Recirculator Setup *42*
2. Results **42**
a. Hysteresis Test Results *42*
b. Effect of Startup Temperature on the MEMS Rate Bias *44*
c. Polynomial Generation *46*
d. Algorithm Testing *49*
D. THERMAL RAMP TESTING IN VACUUM **51**
1. Noise Test **51**
2. Testing at Different Vacuum Degrees **53**
3. Thermal Ramp Tests in Vacuum **56**
a. Hysteresis Testing, Conversion to Volts, and Effect of Different Startup Temperatures in Vacuum *56*
b. Polynomial Generation *59*
c. Polynomial Testing and Bias drift *62*
E. RATE TRANSFER TESTING **64**
1. Setup **64**
2. Results **66**
a. B_{cons}, Scale Factor and Nonorthogonality *75*
F. RANDOM VIBRATION TESTING **79**
1. Setup **80**
2. Results **81**
a. Accelerometer Measurements *81*
b. Visual Inspection *87*
c. Functional Test Results *87*
G. ADDITIONAL TESTS AND CHARACTERIZATION **91**
1. ACS Data Save Interval **91**
2. Variability within Tests **91**
3. Drift Characterization Using Allan Variance **94**
a. Results *96*
H. SUMMARY **100**

V. CONCLUSIONS AND FOLLOW-ON WORK **105**
A. CONCLUSIONS **105**
B. FOLLOW-ON TOPICS **106**
1. Warm-Up Drift **106**
2. Allan Variance Characterization **106**
3. Noise Filtering **107**
4. Verification and Validation of Final Error Compensation Algorithm **107**
5. Initial Alignment **107**
a. Gyro Bias Calibration from Three-Axis Magnetometer Measurements *108*

APPENDICES **109**
A. QRS11 PERFORMANCE SPECIFICATION **110**
B. MAIN TEST LIST **111**

C. SCHEMATICS 121
D. HYSTERESIS TEST RESULTS 124
E1. S_{FX} RESULTS 138
E2. M_{XY} RESULTS 139
E3. M_{XZ} RESULTS 140
F1. S_{FY} RESULTS 141
F2. M_{YX} RESULTS 142
F3. M_{YZ} RESULTS 143
G1. S_{FZ} RESULTS 144
G2. M_{ZX} RESULTS 145
G3. M_{ZY} RESULTS 146
H1. S_{FX} RESULTS (NO REF) 147
H2. M_{XY} RESULTS (NO REF) 148
H3. M_{XZ} RESULTS (NO REF) 149
I1. S_{FY} RESULTS (NO REF) 150
I2. M_{YX} RESULTS (NO REF) 151
I3. M_{YZ} RESULTS (NO REF) 152
J1 S_{FZ} RESULTS (NO REF) 153
J2. M_{ZX} RESULTS (NO REF) 154
J3. M_{ZY} RESULTS (NO REF) 155
K. ERROR OF CURVE FIT FOR MEMS ELASED TIME < 5 MINUTES 156
L. EARTH RATE COMPONENT 158

LIST OF REFERENCES 159

BIBLIOGRAPHY 163

INITIAL DISTRIBUTION LIST 167

THIS PAGE INTENTIONALLY LEFT BLANK

LIST OF FIGURES

Figure 1. NPSAT1 Modular Component Model (From [4]) 6
Figure 2. ACS, MEMS, and CD&H Data Processing Diagram (After [5]) 13
Figure 3. QRS11 unit 15
Figure 4. Tuning Fork Principle of Operation (From [15]) 16
Figure 5. MEMS Flight Subsystem 23
Figure 6. MEMS subsystem without cover 24
Figure 7. ACS 24
Figure 8. Test Flow 25
Figure 9. Python Data Acquisition Readout 28
Figure 10. MEMS–ACS Data Processing Flowchart (After [2]). 30
Figure 11. Typical Startup Temperature Profile 32
Figure 12. Typical Startup Rate (Bias) Profile 33
Figure 13. Example of Startup Bit Output 34
Figure 14. Cold Plate Test Setup 36
Figure 15. Cold Plate Setup 36
Figure 16. T_m values for the total length of test 37
Figure 17. Comparison of thermocouple and calculated MEMS output 38
Figure 18. Temperature Comparison 39
Figure 19. Thermal Vacuum Chamber 41
Figure 20. TVAC Test Setup 42
Figure 21. Column 1) Rate bias hysteresis result for X sensor showing path misalignment after voltage conversion and column 2) Y sensor showing path misalignment before voltage conversion 43
Figure 22. Sensor startup temperature effects on rate bias: (a,c,e) as seen in raw output form, and (b,d,f) after conversion to volts with R_{shift} correction 45
Figure 23. R_{shift} Dependence on Temperature 46
Figure 24. Thermal-dependent in-run biases for polynomial generation 47
Figure 25. Curve Fit Residual Plots 48
Figure 26. Residual bias after compensation 50
Figure 27. Pump On Test Results 52
Figure 28. Pump Off Test Results 52
Figure 29. String of Beads Model of a Tuning Fork (From [25]) 54
Figure 30. Rate (in-run bias) vs. Interpolated Pressure 55
Figure 31. Hysteresis (thermal and pressure in-run bias) test results in vacuum (row 1 in bits and row 2 in volts) 57
Figure 32. Startup temperature effects/run-to-run bias (column 1) and correction after conversion (column 2) 58
Figure 33. Comparison of ambient/TVAC2–1a and vacuum/FL2–1a Thermal Ramp data (in-run bias): a) before and b) after conversion. FL2–3a data set shows half in ambient and half in vacuum 59
Figure 34. Vacuum thermal ramp data for spacecraft compensation polynomial generation 60

Figure 35. Comparison of Ground and Spacecraft Polynomials 61
Figure 36. (a) Uncompensated Rates, (b) Temperature Compensated Rates, and (c) Temperature and Pressure Compensated Rates 63
Figure 37. Rotary Table Test Setup 65
Figure 38. HAAS Test Setup 65
Figure 39. Example Output of Rate Testing (Z Sensor) 66
Figure 40. Absolute Errors (no reference) 73
Figure 41. Sensor Relative Output Error in Percent (with reference) 74
Figure 42. Bias and Scale Factor from the Input-Output Plot (Z) 75
Figure 43. Example of misalignment errors for the X & Y sensors during a Z axis test. 76
Figure 44. X, Y and Z Misalignment Errors 77
Figure 45. MEMS Random Vibration Test Flow 79
Figure 46. Component Minimum Workmanship Random Vibration Test Levels 80
Figure 47. Random Vibe Test Setup 81
Figure 48. Sine Sweep (Pre Random Vibe) along the Z-Axis 82
Figure 49. Random Vibration along the Z-Axis 82
Figure 50. Low-level Sine Sweep (Pre-Random vibe) along the Y-Axis 83
Figure 51. Random Vibration along the Y-Axis 84
Figure 52. Low-level Sine Sweep (Post Random Vibe) along the Y-Axis 84
Figure 53. Low-Level Sine Sweep (Pre Random Vibe) along the X-Axis 85
Figure 54. Random Vibration along the X-Axis 86
Figure 55. Low-Level Sine Sweep (Post Random Vibe) along the X-Axis 86
Figure 56. Functional Tests of Z Sensor 88
Figure 57. Functional Tests of Y Sensor 88
Figure 58. Functional Tests of X Sensor 89
Figure 59. Short Duration Tests (1-10) 92
Figure 60. Variance of the 200 point averages in Test 1 92
Figure 61. Variance of the 200 point averages in Test 2. The first few points right after turn on are typically very large variances and will not be used by the ACS. 93
Figure 62. Variance between tests 93
Figure 63. Sample Plot of Allan Variance Analysis Results Showing Different Noise Components (From [33]). 95
Figure 64. Allan Deviation of 2 hour data 97
Figure 65. Sample Plot Showing Noise Components from Slope of Fitted Line 98

LIST OF TABLES

Table 1. Component Minimum Workmanship Random Vibration Test Levels.....9
Table 2. New Nominal Voltage Values.....37
Table 3. Cubic Bias Compensation Values in Volts (for ground tests).....47
Table 4. Cubic Bias Compensation Values in °C vs. °/sec (for ground tests).....48
Table 5. Noise Test Results.....53
Table 6. Pressure Bias Test Results.....56
Table 7. Spacecraft Cubic Bias Compensation Values in Volts.....60
Table 8. Spacecraft Cubic Bias Compensation Values in °C vs. °/sec.....61
Table 9. Z Sensor Output Error in Percent.....69
Table 10. X Sensor Output Error in Percent.....70
Table 11. Y Sensor Output Error in Percent.....71
Table 12. Comparison of Sf and b_{cons}.....90
Table 13. Summary of Initial Noise Analysis.....99
Table 14. Summary of Results, Comparison to Previous Research and Manufacturer Data.....100
Table 15. MEMS Output.....103

THIS PAGE INTENTIONALLY LEFT BLANK

LIST OF ABBREVIATIONS AND ACRONYMS

A/D	Analog to Digital
ACS	Attitude Control System
ADC	Analog to Digital Converter
ARW	Angle Random Walk
BIT	Built-in-Test
CD&H	Command and Data Handling System
CERTO	Coherent Electromagnetic Radio Tomography
CFTP	Configurable Fault-tolerant Processor
COTS	Commercial Off-the-Shelf
EDU	Engineering Development Unit
EELV	Expandable secondary payload adapter
EPS	Electrical Power Subsystem
ESPA	EELV Secondary Payload Adapter
FPGA	Field Programmable Gate Array
GEVS	General Environmental Verification Standard
GSFC	Goddard Space Flight Center
ITJ	Improved Triple-Junction
LEO	Low Earth Orbit
MEMS	Micro-Electro-Mechanical Systems
NASA	National Aeronautics and Space Administration
NPS	Naval Postgraduate School
NPSAT1	NPS Spacecraft Architecture and Technology Demonstration Satellite
NRL	Naval Research Laboratory
PANSAT	Petite Amateur Navy Satellite
PCFB	Power Control and Filter Board
PRCB	Power Regulation and Control Board
PSC	Planetary Systems, Corp.
PSD	Power Spectral Density

RFS	Radio Frequency Subsystem
SMS	Solar Cell Measurement System
SSAG	Space Systems Academic Group
TRT	Tilt and Rotation Table
TVAC	Thermal Vacuum Chamber
VISIM	Visible Wavelength Imager

ACKNOWLEDGMENTS

I would like to thank the Space Systems Academic Group for the opportunity to conduct this research at NPS. I am grateful to Jim Horning and Professor Jim Newman, for their guidance and for agreeing to be my advisor and co-advisor. I would also like to thank Ron Phelps, Dan Sakoda, David Rigmaiden, Professor Barry Leonard, Professor Panholzer, and Professor Rhoades for their valuable assistance during the completion of this project. I acknowledge NSWC and AWTAP for making the research trip and this degree possible.

Finally, I would like to thank my husband, Stefan, for his support, understanding, and encouragement throughout this Master's program.

THIS PAGE INTENTIONALLY LEFT BLANK

I. INTRODUCTION

A. BACKGROUND

The Naval Postgraduate School Spacecraft Architecture and Technology Demonstration Satellite (NPSAT1) program is an effort belonging to the growing trend toward smaller spacecrafts, driven by the need to develop simpler and modular systems [1]. The primary goal of this thesis is to certify and characterize the commercial off-the-shelf (COTS) MEMS devices for flight on NPSAT1 and possible implementation into future missions.

This research builds on and extends the thesis titled "Characterization, Optimization, and Test for the NPSAT1 MEMS 3-Axis Rate Sensor Suite for use in Small Satellite Attitude Control," by Maj. Thomas S. Pugsley, USA, published in September 2007 [2]. In Maj. Pugsley's thesis, the MEMS 3-axis rate sensor suite was fully tested and characterized. The experimental results proved the sensor suite's effectiveness as a relatively low-cost, low mass augmentation to the magnetometer for satellite rate determination, as well as its ability to measure very low rates. He then modified the original design and operations of the sensor suite to maximize its accuracy and utility. A complete flight-like subsystem was built and tested. After the completion of [2], this MEMS subsystem was processed for flight and was considered the flight unit for NPSAT1.

In this research, similar tests were conducted on the MEMS subsystem proto-flight unit. Since the writing of [2], one of the rate sensors was replaced due to damage in handling; this required performance and characterization re-testing due to the unique compensation equations of each sensor. Furthermore, it has been recommended by the program leads that the MEMS unit fly unpressurized, as pressure changes result in a rate bias, and there is no way to verify the pressure integrity of the MEMS unit on-orbit. This new requirement needed consideration and testing to determine the unpressurized bias as a function of temperature.

This thesis sought to improve the polynomials for the rate error compensation, and to accomplish this using the MEMS and ACS as an integrated system. By testing the subsystems together, the quality of the tests was enhanced and the interface errors were reduced. Example of interface errors include offset voltages of operational amplifiers, parasitic capacitance, and measurement noise [3]. The tests were aimed to gain an understanding of error sources including, but not limited to, those identified in [2]. Finally, 3-axis vibration acceptance testing was conducted to screen for workmanship defects prior to spacecraft integration.

B. NPSAT1 OVERVIEW

NPSAT1 is the follow-on satellite project after the small, digital communications satellite Petite Amateur Navy Satellite (PANSAT), launched aboard the *Discovery* Space Shuttle in October 1998. NPSAT1 was conceived and developed by the Naval Postgraduate School Space Systems Academic Group (SSAG) with the primary objective of providing education and hands-on experience to NPS Space Systems Engineering and Space Systems Operations students. Its secondary objective is to provide a platform for small satellite technology proof-of-concept demonstrations and to provide a platform for space flight experiments [4]. NPSAT1 was unable to meet its last launch opportunity in March 2007. Until a new launch vehicle is selected, the program will continue to test to a booster launch profile of an Atlas V. Once in orbit, NPSAT1 will provide more opportunities for student involvement, in operations and in earth observations.

NPSAT1 is an 82 kg, 12-sided cylindrical satellite configured to interface with the expendable launch vehicle (EELV) secondary payload adapter. It is designed for a 2-year mission life and its reference mission is chosen to be a circular low Earth orbit. It is a gravity gradient friendly, nadir pointing, three-axis stabilized body. In addition to the base plate, two equipment decks will host six experiments. The onboard experiments according to [2], [5], [6] are:

1. Coherent Electromagnetic Radio Beacon Tomography (CERTO)

CERTO is a Naval Research Laboratory (NRL)-sponsored test that will measure the integrated electron density of the ionosphere in the observation plane. CERTO will

also be used to (1) develop and test tomographic algorithms for reconstruction of ionospheric irregularities, (2) provide a database for global models of the ionosphere, (3) characterize the ionosphere for geolocation, and (4) perform scintillation studies of the ionosphere.

2. Langmuir Probe

This is also an NRL-sponsored test designed to augment the CERTO data by taking on-orbit measurements at spacecraft altitude. The data can be processed for correlation with the ground observation results of the CERTO beacon.

3. Configurable Fault-tolerant Processor (CFTP)

The CFTP is a NPS SSAG-sponsored experiment that will use a Field Programmable Gate Array (FPGA) to test an adaptable and redundant computer architecture for reliable computing for space applications.

4. COTS Visible Wavelength Imager (VISIM)

The VISIM experiment consists of a COTS color digital camera and a camera controller board to produce less than one kilometer of optic resolution. It is primarily to be used to generate data for on-board processing by the CFTP experiment and for ground operations by students through an Internet-based user interface. This is an NPS SSAG sponsored experiment.

5. Solar Cell Measurement System (SMS)

The SMS will experiment with Improved Triple-Junction (ITJ) solar cells, perform current-voltage measurements, and produce I-V characterization plots. In addition, the experimental control hardware will be investigated and provide flight demonstration of the ITJ [2]. This is experiment will also be provided by NPS.

6. COTS Micro-electromechanical 3-axis Rate Sensor Suite

The purpose of the MEMS experiment is to provide flight experience with MEMS devices. The MEMS rate sensor is a three-axis rate sensor using three COTS MEMS devices. Studies, calibration, and tests on non-flight units conducted by E. Okano (2001) and T. Pugsley (2007) showed the feasibility of BEI Systron Donner QRS11 high

performance rate sensor to measure below its ±5°/s design range specification. The 2007 results demonstrated that the MEMS could accurately resolve rates as low as 1/7 of the orbital rate; it was also demonstrated in [2] that this resolution could be further improved to 1/16 of the orbital rate using extended averaging. Although the sensor may be capable of measuring suborbital rates, the working resolution is limited by the interface electronics and the software. The Attitude Control System (ACS) is not currently set up to perform rate sampling longer than one second. Hence, the resolution of the MEMS is limited by the ACS control algorithm. The MEMS would not meet requirements for space applications at orbital rates, but it will be used at launch vehicle separation where tip-off rates can be high.

A new packaging requirement has been added to this experiment, requiring recalibration of the flight sensors. In this thesis, retesting was conducted on the MEMS subsystem, as it would be configured in the flight setup with the ACS. Acceptance testing was also performed. This is an NPS sponsored experiment.

In addition to the experiments above, NPSAT1 will also include NPS-built technology demonstration payloads. NPSAT1 has four major subsystems that will utilize experimental components [2], [5], [6].

1. Command and Data Handling Subsystem (C&DH)

The Command and Data Handler will demonstrate the ability of COTS, PC-compatible and open source technology for space applications. This subsystem contains a motherboard, a mass storage and A/D and digital output board, the configurable fault tolerant processor (CFTP) experiment board, a power supply and modem and radio frequency component which are housed in one box and attached to a PC/104 bus.

2. Radio Frequency Subsystem (RFS)

The radio frequency subsystem is a full duplex communication system providing 100 kbps for uplink and downlink to the ground communication station. The uplink channel operates at 1767.565 MHz and the downlink channel operates at 2207.3 MHz. NPSAT1 has antennae pairs for both nadir-pointing and zenith-pointing capabilities [4].

3. Electrical Power Subsystem (EPS)

The electrical power subsystem consists of advanced triple junction solar cells, experimental lithium (Li-ion) battery, and the power distribution and control electronics composed of a digital processor board and an analog switching board [4], [5].

4. Attitude Control Subsystem (ACS)

The attitude control subsystem is used for three-axis stabilization; it consists of three magnetic torquer coils for actuators, a three-axis magnetometer as the sensor, and the ACS controller. The magnetic control approach of NPSAT1 relies on favorable moments of inertia by optimum equipment placement and ballast [7].

Figure 1 depicts an expanded view of the experiments and subsystems located within the spacecraft.

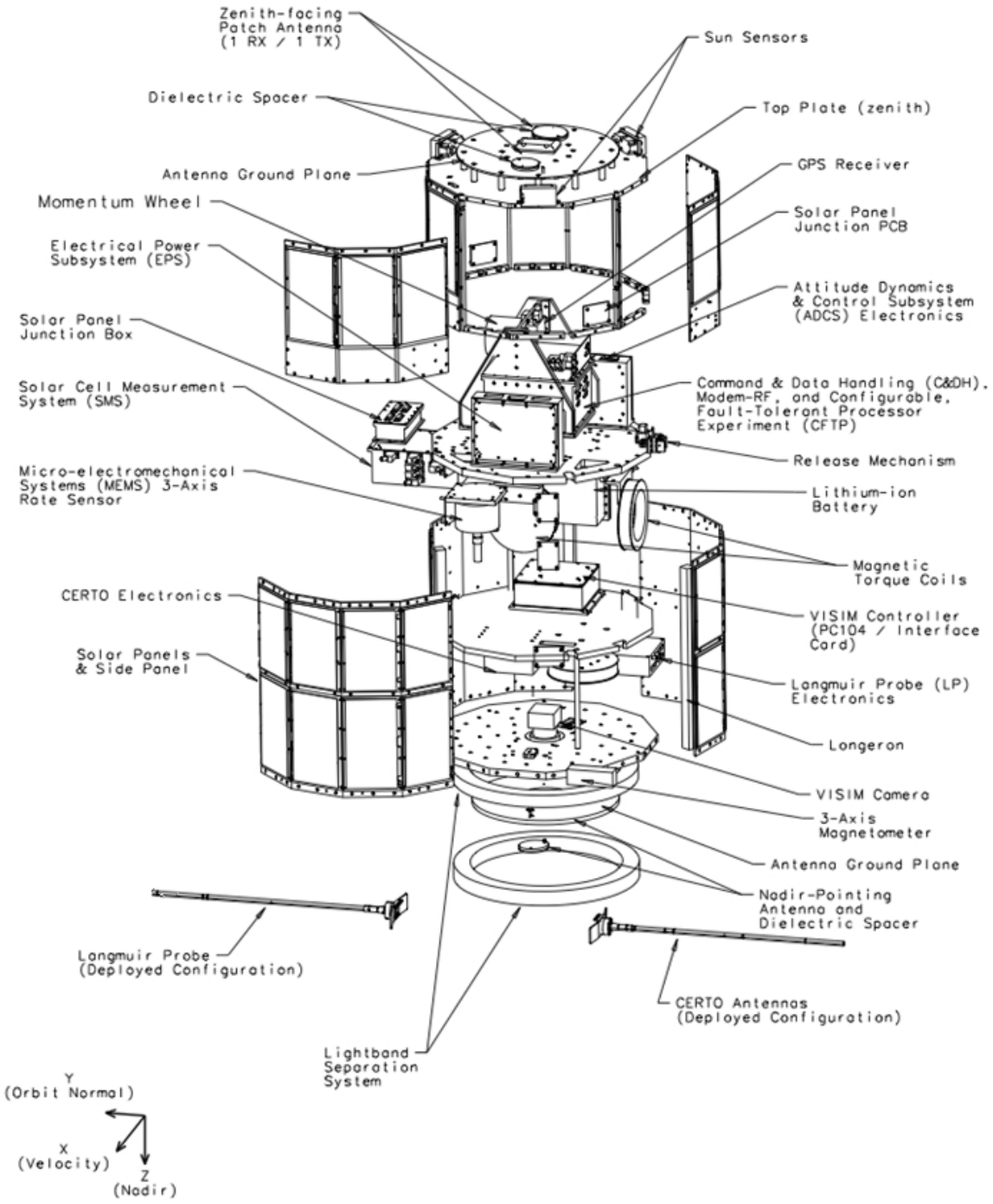

Figure 1. NPSAT1 Modular Component Model (From [4])

C. COTS MICRO-ELECTROMECHANICAL 3-AXIS RATE SENSOR EXPERIMENT, REQUIREMENTS REVIEW AND UPDATE

There are no changes to the MEMS performance requirements. On the other hand, the operational requirements have an additional requirement of operating in an unpressurized package. These are discussed in detail below.

1. Performance Requirements

a. Rate Performance Requirements

Initially, there were two ranges of rotational rates during which the MEMS would be used: 1) tip-off rates right at launch vehicle separation and 2) sub-orbital rates to monitor rates of the spacecraft during attitude control. In [2], the results showed that the MEMS rate sensors can measure rates as low as 1/16 of the orbital rate but requires extended averaging and filtering to do so. The current ACS control algorithm is not set up to allow rate determination longer than one second. Consequently, the attitude control mode using the MEMS has become a low priority, but the possibility was kept open depending on the time and resources available to perform the necessary changes to the ACS control algorithm. Primarily, the MEMS will be used shortly after tip-off, while the ACS uses its B-dot damping algorithm to reduce the rates from approximately 5 °/sec to twice the orbital rate or 0.132 °/sec. B-dot dampening is a rate damping scheme using magnetometers and magnetic torquers to detumble and align the spacecraft with the local B-field. The B-dot control mode is a two-second cycle, which executes one second of magnetic field measurement and processing, followed by another second of torquing. During the torque phase, the magnetometer's measurements of the earth's magnetic field may be contaminated by the torque coils magnetic field. It is during the torque phase that the MEMS will augment the ACS and provide more accurate rate data. The MEMS is required to be able to provide an accuracy of within ±5% of the actual rate.

b. Temperature Performance Requirements

The internal temperature of the MEMS is used in the algorithm for the thermal compensation of the rate output. For space operations, a calibrated temperature output in °C is not necessary since the voltage output corresponding to the temperature

values[1] can be used directly for the compensation. However, for ground testing, the temperature in °C is not only preferred, but also essential in monitoring the MEMS, especially during the thermal chamber tests. The temperature output of the MEMS sensor suite had previously been limited to -40°C to +55°C; this is not an issue for space operations since the expected temperature range of the sensor is -11°C to +9°C. However, the compensation polynomials must span the entire qualification range and requires an upper limit of +66°C. Prior to flight testing, a small modification was made to the MEMS circuit to increase the dynamic range and meet this derived requirement. In [2], the accuracy of the temperature output was set to ±2% of the actual temperature. In this thesis, the modified circuit was tested and the accuracy of the temperature output was evaluated.

c. BIT Performance Requirements

The built-in-test (BIT) output is a simple indicator of the operational status of the sensor. If the sensor is in an operational state, the BIT output would display ≥ 2.4 V; otherwise, it would display ≤ 0.8 V. The BIT output on each device is collected and will be stored and sent as spacecraft telemetry. If the ACS uses the MEMS for attitude control, the BIT will be used to determine if the MEMS data is valid.

2. Operational Requirements

2.1 The Launch Environment

a. Vibration Requirements

NPSAT1 was not ready for the last launch opportunity in March 2007 with the Space Test Program 1 (STP-1) mission aboard an Atlas V, using the Evolved Expendable Launch Vehicle (EELV) Secondary Payload Adapter (ESPA). Until a new launcher is selected, the program will continue to test using the launch profile for an Atlas V [2] as the next ESPA ring is expected to fly in 2014 on an Atlas V. In 2005, qualification tests were performed on the NPSAT1 engineering development unit (EDU).

[1] See Equation (5).

The NPSAT1 EDU was similar in dimension to the flight vehicle structure with dummy masses used in place of subsystems or components [8]. Acceptance tests are required both at the component and system levels on separate flight units.

For the component acceptance test, the MEMS flight unit must be tested to the levels based on the NASA-STD-7000, GSFC General Environmental Verification Standard (GEVS), 2.4.2.5.a [9]. Accordingly, the test sequence shall start with a sine sweep of 4 oct/min, followed by the random vibration test using the levels shown in Table 1 for 1 minute/axis; a functional test shall be performed after each vibration test in the three orthogonal axes. The QRS11 is specified to operate at 8 g_{rms} 20 Hz to 2 kHz random, survive 20 g_{rms} at 20 Hz to 2 kHz random for 5 minutes/axis, with a maximum shock of 200 g in any axis [14].

Table 1. Component Minimum Workmanship Random Vibration Test Levels

Frequency (Hz)	ASD Level (g^2/Hz)
20	0.01
20–50	+3dB/oct
50–500	0.04
500–2000	-3 dB/oct
2000	0.01
Overall	6.8 g_{rms}

Once all component tests are completed, system-level acceptance tests using all flight parts would be conducted in accordance with the policy statement promulgate by the STP-1 mission office [8].

2.2 The Operational Environment

b. Thermal Requirements

Initial worst-case thermal simulations produced an operating temperature range for the MEMS between -11°C to +9°C, and predicted that the MEMS temperature would remain fairly constant around 5°C. A safety margin was added to these simulation results and the operating temperature range was set to ±20°C. This operating range will be used until a new reference orbit is determined and new thermal analyses can be performed [2].

The flight acceptance and qualification of a non-operating flight-unit is -29°C to +66°C. The MEMS subsystem must meet this temperature range and survive with no catastrophic failures. The QRS11 has an operating temperature range of -40°C to +80°C, hence the sensor specification provides sufficient margin during characterization testing.

c. Radiation Requirements

The QRS11 sensor was originally designed for missile guidance and control applications; it was not designed for space applications and the space environment where radiation is an issue. Due to its recent applications in space, however, radiation tests have been performed by one of SDI's customers [2]. Testing included total dose (Cobalt 60, increments up to 80 Krad), and heavy particle (Californium 252 to a fluence of 1.9×10^6 particles/cm^2). No effects due to radiation were noted in these tests and their results suggest that the risks from on-orbit radiation are negligible [2]. No further radiation tests are planned for the MEMS subsystem.

d. Vacuum Pressure Decay

The vacuum pressure for a typical mission can be expected to decrease from 1.013×10^5 N/m^2 (760 Torr) on Earth to 1.33×10^{-3} N/m^2 (1×10^{-5} Torr) in deep space [10]. This change in pressure would result in rate bias offsets, as was observed in the tests conducted by A. Cropp, et al in 2006 [11]. A permanent hermetic seal is very difficult to achieve. Additionally, NPSAT1 has no system capability to check the

pressure integrity of the MEMS; there is no feature to verify that all the seals of the MEMS assembly will hold and maintain a certain pressure level set on ground. Due to these vacuum effects, a recommendation was made after the writing of [2] that the MEMS unit would fly unpressurized. This requires a new set of compensation polynomials that would correct the effects of changes in pressure in addition to changes in temperature. The MEMS unit must meet the performance requirements in vacuum.

2.3 Spacecraft Interface

e. Input Requirements

The MEMS sensor suite will be provided by the spacecraft bus with ±6 VDC and a common return through three pins of a 15-pin connector, linking the MEMS wiring harness to the ACS. The QRS11 sensors require an input of ±5 VDC, with a tolerance of ±3%. The sensor is sensitive to power line noise and noise must be minimized in the 7 kHz to 10 kHz band. In [2], a Power Regulation and Control Board (PRCB) was built to regulate and filter the input to the MEMS. The PRCB was tested and the results yielded a voltage regulation error of only ±0.2%. Furthermore, all power and signal grounds must be connected at only one point to avoid ground loops, which would result in bias shifts [12].

f. Output Requirements

The MEMS must provide the ACS with rate, temperature, and BIT data for all 3-axes using the single 15-pin connector allocated to the MEMS device. It must also interface with the wiring harnesses.

D. ACS, MEMS, AND C&DH OPERATION

The ACS uses the change of magnetic field to align the spacecraft with the local B-field. Figure 2 depicts the processing diagram for the ACS, MEMS, and C&DH. The process starts with the sampling phase. Within this block, the analog magnetometer signals are converted into digital signals. Temperature compensation computation is done on the ACS board. Data processing, as explained in [5], begins with the field measurement phase where the ACS calculation of the mean of the last four magnetic field

measurements. This average is used as an input to the control torque algorithm run on the C&DH, which includes attitude and requested torque calculation. This torque request is sent from the C&DH to the ACS and converted back into an analog signal, which actuates the torque coils. The torquers are then allowed to relax and stabilize after actuation. The rate measurements acquired by the magnetometer during torquing may be corrupted by disturbances from the torquer's magnetic field. For this reason, the MEMS sensor suite was selected to augment the system and supply the ACS with more accurate rate data while the torquers are being used. The MEMS operation is similar to the magnetometer. First, the rate measurement averages are sent to the ACS for bias compensation. The rate data are then sent to the CD&H and is used to estimate B-dot. This estimation is described in detail in [13]. The torque request is then sent back to ACS and converted back to analog signal, which actuates the torque coils.

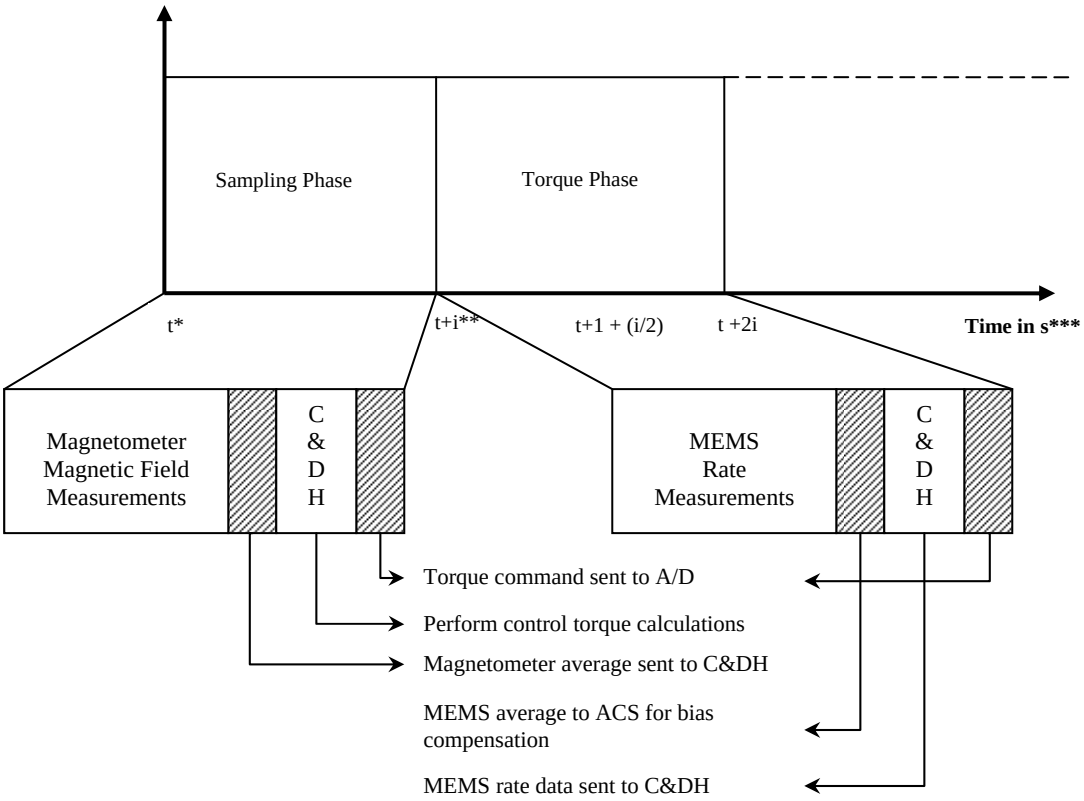

* Current test setup value of t is 300 secs
(Assumes a 5-min initialization time)

** Interval *i* is set at *i*=1 for B-dot damping; TBD for experimental attitude maneuvering

*** ~1000 secs total for B-dot damping

Figure 2. ACS, MEMS, and CD&H Data Processing Diagram (After [5])

THIS PAGE INTENTIONALLY LEFT BLANK

II. MICROMACHINED VIBRATORY GYROSCOPES

MEMS-based gyroscopes are becoming a viable alternative to expensive and bulky conventional sensors. The BEI Systron Donner QRS11 gyrochip, selected for the NPSAT1 experiment, has demonstrated its use in space in several missions, including but not limited to: 1) NASA STS-64, SAFER Experiment, 1994, 2) NASA Mars Rover Mission, Sojourner, 1996, 3) NASA STS-87, AERcam Experiment, 1997, 4) Surrey Satellite Technology Ltd, UoSat12, 1999, 5) ESA Integral Spacecraft, 2002, 6) ESA Smart 1, 2003, 7) ESA GIOVE-A Spacecraft, 2005, 8) ESA Planck Probe, 2009, and 9) ESA Herschel Space Observatory, 2009 [2]. The following covers some of the basics of the QRS11.

A. BEI SYSTRON DONNER QRS11 SENSOR

The QRS11, as shown in Figure 3, is a high performance rate sensor that features Quartz MEMS technology, providing a compact and lightweight sensor. There are no moving parts in this solid-state gyro design, making it reliable and durable with virtually unlimited life [14].

Figure 3. QRS11 unit

The QRS11 sensor's operation is based on the tuning fork principle, shown in Figure 4. The sensing element is made of piezoelectric quartz material configured into an 'H' fork, forming the drive and pickup tines. The input tines are driven at their resonant frequency of about 10 kHz. A Coriolis torque is produced when the sensor is rotated about the input axis, which oscillates with the drive tine mass velocity. Momentum is transferred to the perpendicular plane of the vibrating tines, which bends the pickup tines.

Due to this displacement, an electrical signal is produced proportional to the input rotational rate [15]. The signals are routed through the mount and then amplified and demodulated into a DC signal proportional to the rotation [16].

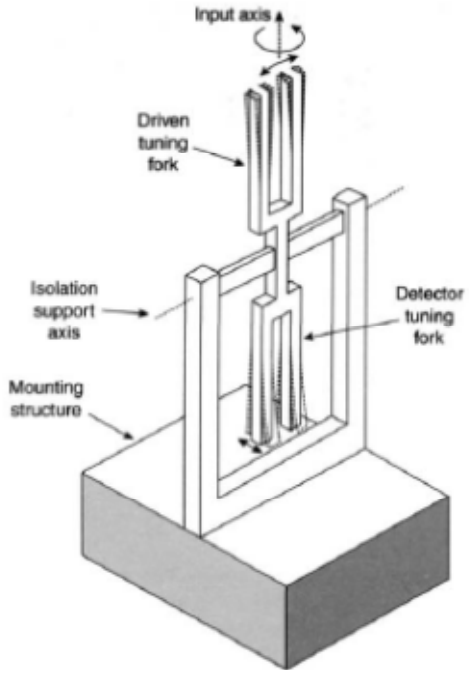

Figure 4. Tuning Fork Principle of Operation (From [15])

The QRS11 general specifications can be found in Appendix A. NPSAT1 uses the high-performance option (-101), non-standard range (±5 °/sec max rate), and the low noise option (-565). Further details about the QRS11 can be found in [2] and [16].

B. ERROR SOURCES

Since this thesis deals with the MEMS rate sensor triad and the ACS measurement system, we address not only the error characteristics of the MEMS alone but also those errors that arise from the experimental setup, methods, and other components of the system. This section begins with some general sources of uncertainties taken after concepts from [17]. Then, a discussion of sensor-specific error fundamentals follows.

1. General Error Sources

Errors in a measurement system include fixed, systematic errors that remain constant in repeated measurements under fixed conditions, and a random error component that can be described by statistical estimates. Measurement errors can be grouped into three error source groups: calibration, data-acquisition, and data-reduction errors.

Calibration errors are those that enter into the measuring system by the errors inherent to the standard used in the calibration and the manner in which the standard is applied. Examples of these elemental errors for this experiment include uncertainties from the laboratory standards, such as the thermometer used in the temperature output calibration, and the turntable used for angular rate tests.

Data-acquisition errors originate during the act of measurement and come from measurement system operating conditions, sensor-transducer stage, signal conditioning stage, output stage, process operating conditions, sensor installation effects, environmental effects, spatial variation error, temporal variation error, etc. Some of the most difficult sensor errors to quantify are in this group.

Lastly, data-reduction errors are introduced into the test results with the use of curve fits and correlations. Uncertainty associated with the calibration curve fit, truncation or other computational operations, and the number of significant figures contributes to this error group.

2. MEMS Inertial Sensor Errors

The previous section briefly discusses general error sources in a measurement system. These potential error sources were addressed as much as possible during the test setup, measurement, and data analysis in support of determining the error components for the gyroscope model that will be presented in Section C. However, it is not feasible to eliminate all errors. Hence, the main results are focused on selected sensor-specific error characteristics from the facts and definitions below, according to [15], [18], [19], [20], and [22]:

a. Bias

Bias or the zero rate output is defined as the average over a specified time of gyro output measured at specified operating conditions that have no correlation with input rotation, typically expressed in °/sec or °/hr. Several factors affect bias; the four components that this thesis is mainly focused on are [19], [22]:

1. Systematic or constant portion of the bias: This constant error is independent of force or angular rate and is sometimes referred to as the g-independent bias. This fixed error contribution can be corrected or estimated by the ACS processor using laboratory data.

2. Run-to-run or repeatability bias: This error contribution is different between runs but remains constant during a particular run. This run-to-run variation cannot be corrected by the processor but it can be eliminated in the alignment or integration algorithms.

3. Systematic portion of the in-run or stability bias: In-run bias has a systematic and random portion. Herein, the systematic contribution is due to the environmentally sensitive components of the drift rate. Specifically, the tests were designed to investigate the effects of temperature, pressure, temperature hysteresis, and vibration. Other examples of environmental parameters (although outside the scope of this thesis) include acceleration sensitivity and temperature gradient sensitivity. The environmentally sensitive component of drift rate can be corrected by the processor using polynomials derived from laboratory tests.

4. Random portion of the in-run or stability errors (also referred to as random drift rate): This is the residual bias after the error compensation of the deterministic portion. It is also the time-varying component of the bias. These random errors can only be modeled as stochastic processes and cannot be corrected by alignment or by the processor. For attitude control applications, periodic recalibration to an external reference would have to be performed to minimize the effects of long-term drift [28].

Random drift rate is commonly modeled using the Allan variance technique. It is described by the following Allan variance components [20]:

a) Angle Random Walk: The angular error buildup with time that is due to white noise in angular rate, typically expressed in °/√hr or °/s/√hr.

b) Bias Instability: The random variation in bias as computed over specified finite sample time and averaging time intervals, characterized by 1/f power spectral density, typically in °/hr.

c) Rate Random Walk: The drift rate error buildup with time that is due to white noise in angular acceleration, typically expressed in °/hr.

b. Scale Factor

Scale factor is defined as the ratio of a change in output to a change in the input intended to be measured, typically specified in mV/(°/sec). Scale factor error is evaluated from the slope of the least squares straight line fit of the input-output data. Scale factor error specifications include [20]:

1. Linearity error: The deviation of the output from least-squares linear fit of the input-output data. It is generally expressed as a percentage of full scale, or percent of output.

2. Nonlinearity: The systematic deviation from the straight line that defines the nominal input-output relationship.

3. Scale factor temperature and acceleration sensitivity: The change in scale factor resulting from a change in steady state operating temperature and a constant acceleration.

4. Asymmetry error: The difference between the scale factor measured with positive input and that measured with negative input, specified as a fraction of the scale factor measured over the input range.

5. Scale factor stability: The variation in scale factor over a specified time of continuous operation. Ambient temperature, power supply, and additional factors pertinent to the particular application should be specified.

c. Nonorthogonality/Misalignment

These errors arise from imperfections in mounting the sensors, resulting in the misalignment of the inertial sensors with respect to the orthogonal axes of the body frame. This misalignment makes the sensors sensitive to the input rates along the respective orthogonal axes. The nonorthogonality factor is evaluated similarly to the scale factor by taking the slope of the fitted line of input-output data of the sensors orthogonal to the input axis.

Other typical specifications include: operating range, resolution, bandwidth, turn-on-time, linear and angular vibration sensitivity, shock resistance, operating life, operating temperature range, thermal shock, thermal cycling, humidity, electrostatic discharge immunity, and electromagnetic emissions and susceptibilities. A full listing of specifications and general test procedures outlines can be found in [18]. Additionally, other factors that can affect the performance of the sensors can be found in [21].

C. GYROSCOPE ERROR COMPENSATION

From [19], the model for a single-axis gyroscope measurement of the angular rate is given by:

$$I_\omega = \omega + b_{cons} + b_{run-to-run} + b_{in-run} + S\omega + N\omega + \varepsilon(\omega) \quad (1)$$

where,

- I_ω is the measurement in °/sec
- ω is the true angular velocity in °/sec
- b_{cons} is the systematic or constant portion of the bias removed by the calibration process

- $b_{run-to-run}$ is the repeatability bias.
- b_{in-run} is the stability bias.
- S is the gyroscope scale factor error in ppm or %. S is the error from the ideal scale factor S_f of 0.5 V/(°/sec).
- N accounts for the nonorthogonalities or misalignment errors of the gyroscope, in ppm or %.
- $\varepsilon(\omega)$ is the gyroscope sensor noise.

The error compensation in this thesis was structured according to Equation (1) above. The compensated rates are then given by:

$$\widetilde{\boldsymbol{\omega}} = \boldsymbol{I}_{\widetilde{\omega}} - (\boldsymbol{b}_{\boldsymbol{in-run}} + \boldsymbol{M}\widetilde{\boldsymbol{\omega}} + \boldsymbol{b}_{\boldsymbol{cons}}) - \boldsymbol{b}_{\boldsymbol{run-to-run}} - \boldsymbol{\varepsilon}(\widetilde{\boldsymbol{\omega}}) \tag{2}$$

Note that the above equation is in bold to indicate the vector form of the processed output with X, Y, and Z components. Tilde is used above to denote the *estimated* angular rate and to distinguish from the ideal value ω, where $\widetilde{\omega} = \omega + \delta\omega$ and $\delta\omega$ represent additional errors unaccounted for by Equation (2)[2]. Also, the scale factor error S and nonorthogonality N are combined into a matrix, represented by the factor M [22]*:*

$$\boldsymbol{M} = \begin{pmatrix} S_x & m_{xy} & m_{xz} \\ m_{yx} & S_y & m_{yz} \\ m_{zx} & m_{zy} & S_z \end{pmatrix} \tag{3}$$

where the diagonal S_α elements are the scale factor errors, the off-diagonal $m_{\alpha\beta}$ elements are the misalignment errors, α is the test axis, and β is the nonorthogonal axis where the error is sensed.

Furthermore, $b_{in\text{-}run}$ is a cubic polynomial for the compensation of temperature and pressure-dependent biases. Finally, the quantities placed in parenthesis are the errors that can be compensated for by the ACS processor using test data.

[2] For example, additional errors such as acceleration dependence, which was not part of the test series.

In addition to fulfilling the NPSAT1 test and specification requirements, the underlying objective of the following tests is to determine the systematic error components of the above equation.

III. TEST PREPARATIONS

A. TEST UNIT DESCRIPTION AND CHANGES

The test unit in this thesis is the modified MEMS flight subsystem assembly used in the preceding thesis. Since the writing of [2], the test unit was processed for flight and minor changes and improvements were made to satisfy the new requirement of flying unpressurized. Flight processing includes standard parts cleanup, wire replacement, conformal coating of boards, and thread locking of fasteners. In addition, three changes to the test assembly were made. First, a new QRS11 sensor was installed to replace the damaged Y sensor. Second, the Power Control and Filter Boards' (PCFB) temperature filter gain for all three sensors were changed from 13 to 8 to increase the MEMS temperature output range. Third, the two vent holes on the housing, as shown in Figure 5, were unsealed to allow the pressure inside the assembly to equalize to the external pressure.

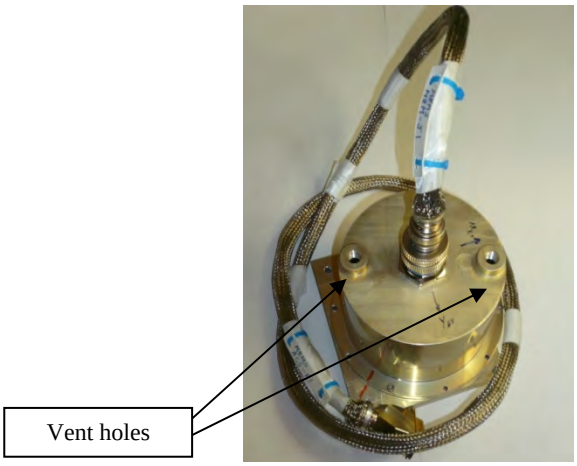

Figure 5. MEMS Flight Subsystem

Figure 6. MEMS subsystem without cover

The changes in the tests conducted in this thesis also extended to the data acquisition method. Previously, the MEMS output was read using a WebDAQ, a data logging and acquisition device. Interface circuit errors must be accounted for in drift bias compensation [3]. While the WebDAQ was sufficient for the initial evaluation tests, the bias compensation equations must account for the sensor biases and the actual flight circuit interface errors. Since the concentration of this thesis is to re-evaluate the sensors for in orbit performance, testing the MEMS and ACS in their flight configuration would render better results. Subjecting the two units in same test environment and using the processed ACS output to obtain the compensation curves would produce the fewest residual errors in the curve fitting. The ACS is shown in Figure 7.

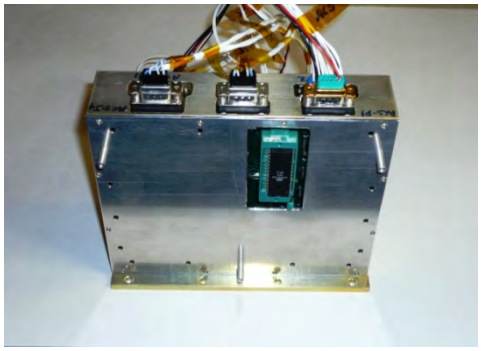

Figure 7. ACS

The data acquisition software operation was also different. In the preceding thesis, the software was started prior to powering the MEMS test unit. This allowed capturing the sensor output from the instant it is turned on until it fully transitioned to its

operational state. The software version used in this thesis required the MEMS electronics to be turned on before software can be enabled to record and save data. This has little impact to the data collection, but it is noted here for the purpose of accounting for an additional delay in the startup or stabilization time of the subsystem.

B. TEST FLOW

A top-level test diagram is provided in Figure 8:

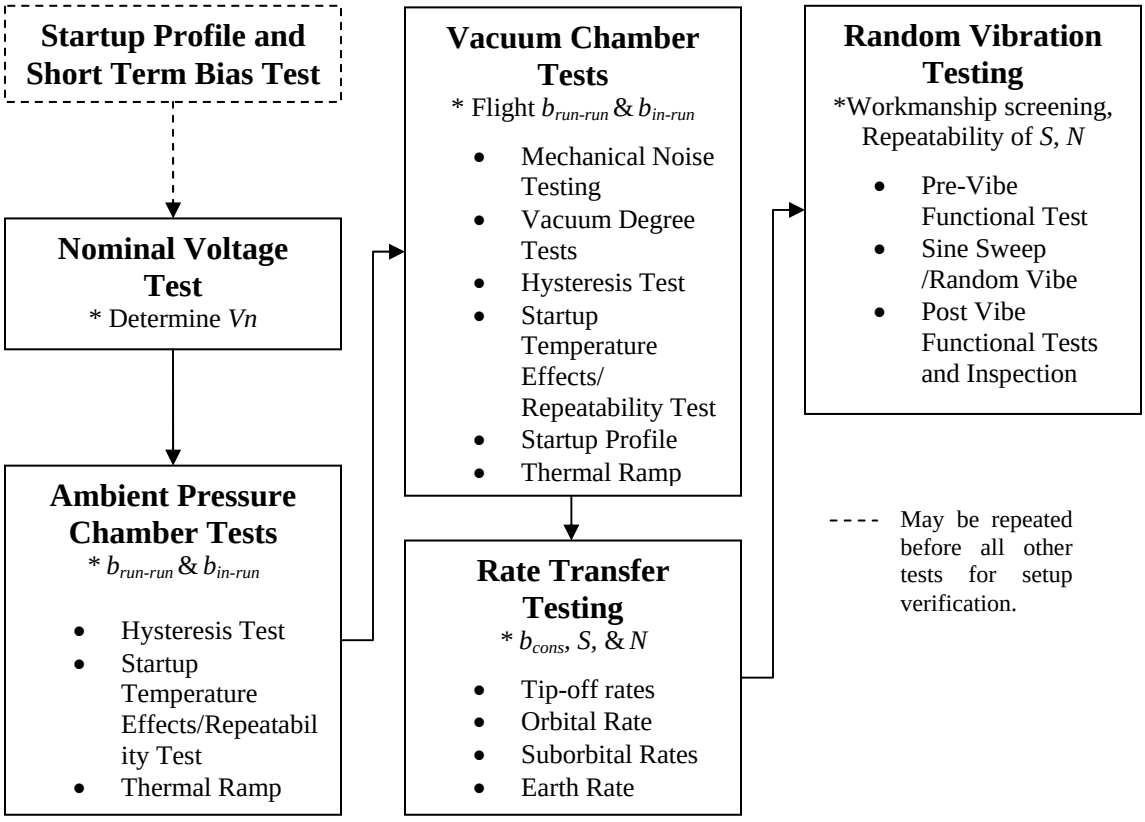

Figure 8. Test Flow

In the diagram above, the test series begins with ambient tests similar to those performed in [2]. First on the list is *Startup Profile and Short Term Bias* testing, which consists of powering the MEMS from the ACS and gathering rate information while the MEMS is stationary to determine the rate output stabilization time. Verification of the built-in-test (BIT) was performed and temperature measurements were noted and compared to what is considered normal values as a way of determining proper operation.

This test was conducted as the first in the series to establish a baseline, and then repeated before conducting each of the other tests to ensure that the setup was correct. In addition to its basic ground testing purposes, a crucial goal of this test is to determine the startup behavior in vacuum. From an operations view, it would be useful to estimate any error introduced to the attitude control system during the warm-up period [23]. The vacuum startup profile test was conducted later in the series.

Nominal Voltage testing was then conducted to calibrate the MEMS temperature output. A calibrated temperature is not necessary for space operations; however, the temperature output was very useful in performing the succeeding chamber tests. The nominal voltage test was performed by setting the MEMS unit on a re-circulator and measuring the steady state temperature output of each sensor at 25°C. The nominal voltage is represented by the symbol *Vn.*

Next, a sequence of chamber tests were conducted—in ambient and under vacuum, to produce two sets of $b_{in\text{-}run}$ compensation polynomials. The *Ambient Pressure Chamber Tests* were performed to determine the thermal compensation polynomials for ground testing[3] and comparative purposes. The ambient $b_{in\text{-}run}$ polynomial represents the deterministic and temperature dependent portion of the in-run bias. The MEMS unit was subjected to the full qualification range of -29°C to +66°C. The temperature dependence of the sensor rate output was eliminated by estimating the zero-rate bias over the full qualification range using a 3rd-order polynomial. The chamber tests also include subtests to investigate and address hysteresis effects noted in [11]. In addition, repeatability tests were conducted to investigate the correlation of rate bias offsets to the startup temperature of the MEMS and electronics ($b_{run\text{-}run}$). In the *Vacuum Chamber Tests*, mechanical noise testing and vacuum degree tests were first conducted to verify the setup. Then, the ambient pressure chamber tests were repeated in vacuum to derive the in-orbit polynomials or the flight $b_{in\text{-}run}$.

After the chamber tests, *Rate Transfer Testing* was conducted to compare the angular rates measured by the MEMS to that given by a rotary table. Rate tests were

[3] Using the flight $b_{in\text{-}run}$ during ground tests would result in rate offsets.

performed at tip-off rates, orbital rates, and at earth rate. The data collected in these tests were thermally compensated using $b_{in\text{-}run}$ and then used to estimate the accuracy of the MEMS per the 5% error requirement set in [2]. Moreover, the data was used to derive the fixed portion of the bias b_{cons} and the scale factor characteristics S and the nonorthogonality constants N in the form of matrix M. Note that the sensors' resolution were estimated using the in-run drift only, since at the time of these tests, the ACS software is only designed to use in-run drift and did not include the rest of compensation terms of Equation (2).

The final test performed in this thesis was the *Random Vibration Test*. This is an environmental test to validate that the MEMS flight unit can withstand the launch vibro-acoustics environment. Testing was performed at acceptance levels in each of three orthogonal axes, followed by a baseline functional test and inspection. Pre- and post-vibe test data were analyzed to determine the vibration sensitivity of the MEMS and the repeatability of its output, scale factor, and nonorthogonality.

C. TEST EQUIPMENT

1. Hardware

The test hardware varies by test. The main test component list is as follows:

- MEMS Rate Sensor Assembly
- Cole Parmer polystat® Recirculator and Cold plate
- Tenney Thermal Vacuum Chamber (TVAC)
- TVAC Harness
- HAAS TRT-7 2 Axis Tilt and Rotation Table (TRT)
- HAAS Harness
- ACS
- MEMS Bracket for HAAS
- Agilent E3236A Power Supply
- Omega Engineering 4 channel Hand Held Thermometer (HH147)
- Precision Level

- RS422 Transceivers
- Computer
- Vibration table
- Camera
- MEMS mounting plate for the vibration table

2. Software

A Python program was used for data acquisition. The program user interface is shown in Figure 9 displaying ACS system outputs. This interface allows the user to enable the test and select database save intervals. FlameRobin, a database administration tool, was used to retrieve information from the database. OriginPro, MS Excel, and MATLAB were used for data analysis and graphing.

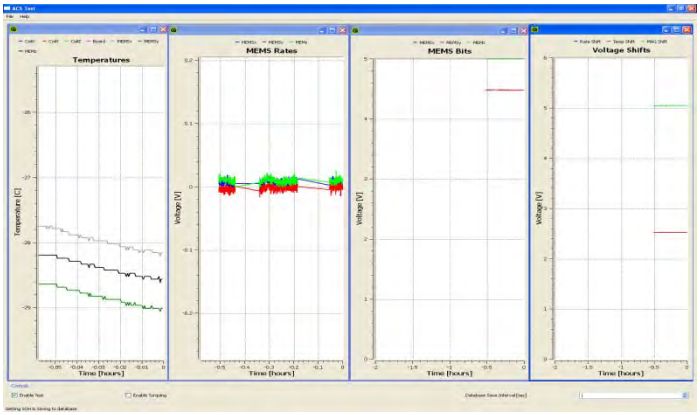

Figure 9. Python Data Acquisition Readout

D. DATA FLOW

The ACS data processing flowchart, updated since the completion of [2], is shown in Figure 10. Rate, temperature, and BIT information from the rate sensors are filtered through a low pass filter. A gain G is applied to the temperature output only. Then, all three data sets are sent to the ACS accumulator program where the rate data are averaged 200 points/sec. The ACS uses a 12-bit analog to digital (A/D) converter with a dynamic range of 0 to 5 V; 2^{12} or 0 to 4095 counts are possible and the resulting step size is 1.22 mV. The output requires that all three data types be measured with respect to ground to obtain the most accurate data. The spacecraft bus voltage of 28 V is regulated down to

±15 V by a DC/DC converter in the ACS. This ±15 V is further regulated down to 2.5V. The MEMS data would all be shifted down by 2.5 V. As the voltage references drift with time and temperature, this 2.5 V reference fluctuates slightly. To correct for the voltage drift, measured values of the temperature (T_{shift}) and rate (R_{shift}) voltage references are used instead of 2.5 V constants [23]. The voltage conversions are summarized in the following equations:

$$T_m\ (\mathrm{V}) = \left(\frac{T_m\ (\mathrm{bits})}{4095} \times 5\right) - T_{shift} \tag{4}$$

$$R_{ave}\ (\mathrm{V}) = \left(\frac{R_{ave}(\mathrm{bits})}{4095} \times 5\right) - R_{shift} \tag{5}$$

$$BIT\ (\mathrm{V}) = \left(\frac{BIT\ (\mathrm{bits})}{4095} \times 5\right) \tag{6}$$

The ideal output vs. applied rate relationship is described by:

$$\mathrm{V_{out}} = S_f * \omega \tag{7}$$

where $\mathrm{V_{out}}$ is the output voltage of the MEMS, S_f is the ideal scale factor, ω is the applied rate in °/sec. Conversely, the measured rate using Equation (5) is then:

$$I_{\tilde{\omega}} = R_{ave} * \frac{1}{S_f} \tag{8}$$

Above, the ideal scale factor of 0.5 V/(°/sec) is used for the output voltage conversion to °/sec. The scale factor error S is taken into account as a separate entity. For the test configuration, the raw MEMS output and voltage references were the minimum data required to perform the analyses. The final form of the MEMS output $\tilde{\omega}$ would use the compensation factors described in Equation (2).

The temperature data, on the other hand, is converted to °C using Equations (10), (11), and (12). The raw and converted data are saved to the database at a user defined interval n and ACS ID number. The variables are saved to the database under more descriptive names, shown in capital letters in Figure 10. The data can be accessed for analysis by date and time stamps or the assigned ACS ID #.

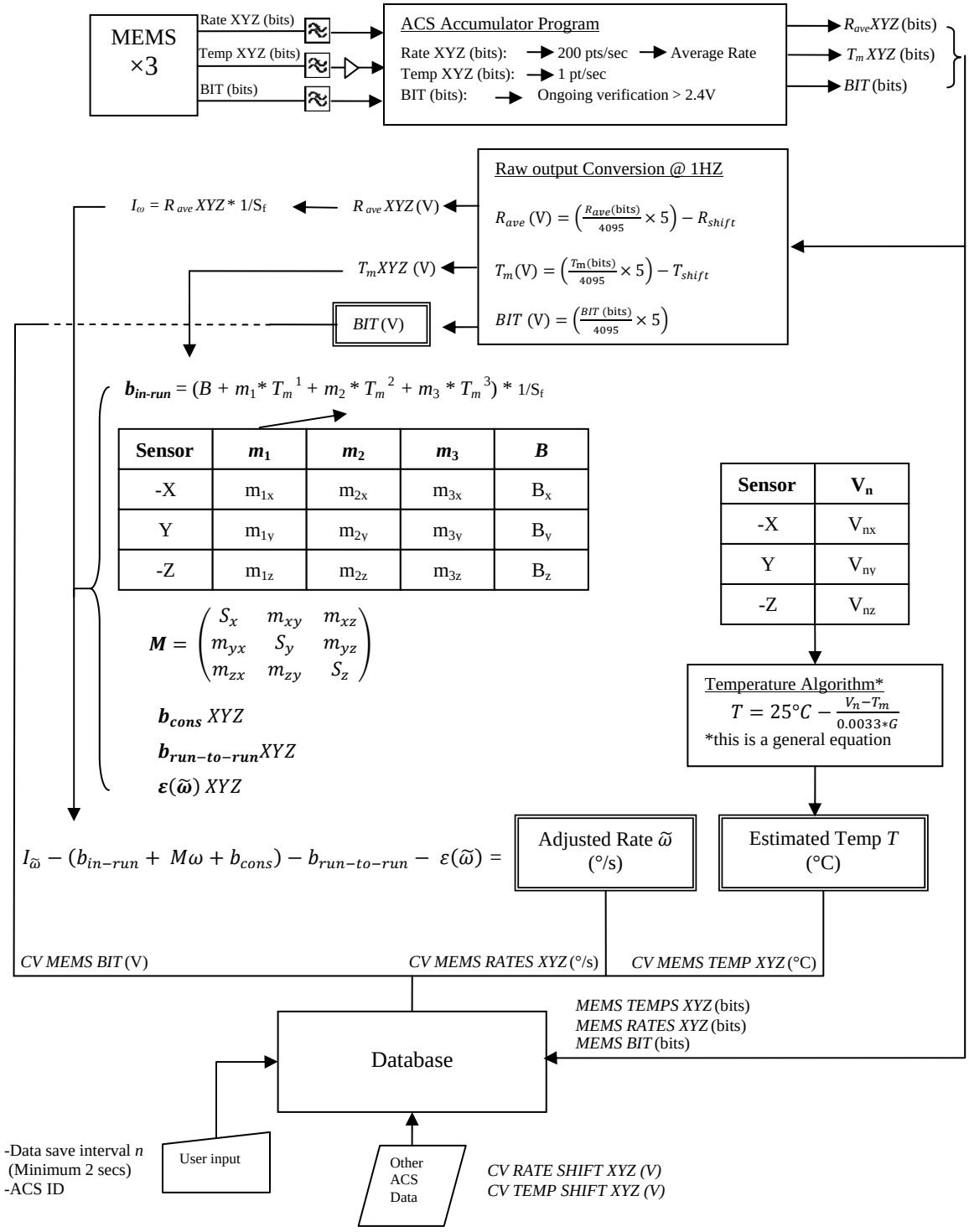

Figure 10. MEMS–ACS Data Processing Flowchart (After [2]).

IV. PERFORMANCE AND ACCEPTANCE EVALUATION TESTS

The performance envelope of the MEMS sensor suite was investigated and characterized using a three-part process [15]: (1) coarse checking or evaluation using simple tests, (2) static testing and/or calibration, and (3) dynamic testing. Coarse checking includes startup tests to verify that all the right electrical connections were made and that the expected signals from the QRS11 output were received. Moreover, it includes simple checks against the manufacturer's data sheets and previous test results. Static tests, such as temperature calibration, thermal, pressure, and earth rate tests, were performed with the sensor assembly kept fixed in one position while observing the response to a specific natural effect. The data collected in these tests were used either for calibration or for compensation. In dynamic tests, such as the rate tests, the sensor suite was subjected to motion and the response of the subsystem to the disturbance was monitored and compared with the stimulus.

Typically, there are three distinct categories of sensor testing: qualification, acceptance, and reliability tests. The definitions of these categories, as well as the testing and calibration schemes, may vary depending on the development phase. In this thesis, the terms "performance" and "acceptance" testing describe the tests performed on the MEMS sensor assembly prior to integration. The objective of the performance and characterization testing is to establish whether the device conforms to the manufacturer's specification and if the MEMS sensor is still appropriate to the project application, given the new requirement of flying unpressurized. On the other hand, the philosophy of acceptance testing is to establish that the sensor system is compatible with the host vehicle, that it will achieve the required accuracy, and comply with the project application objectives. The Lightband separation system from Planetary Systems, Corp. (PSC) is considered the most likely candidate for the launch system [24]; and the tip-off rate performance requirements are based on the rates imparted to the spacecraft at launch vehicle separation by the Lightband system. Acceptance testing is based on the NASA GSFC General Environmental Verification Standard (GEVS).

A. STARTUP PROFILE AND SHORT TERM BIAS TESTING

The objectives of the startup profile and short term bias testing are (1) to develop a basic understanding of the startup behavior of the outputs and (2) to verify the operation of the MEMS unit. The basic setup to run a startup profile requires the 28 V power supply, MEMS, ACS, and network computer. In the next sections, this basic setup is enlarged by adding test equipment—a cold plate, a thermal vacuum chamber, or a rate table, to evaluate the sensor for a specific environmental or dynamic response. For startup characterization purposes, this simple test is performed by turning on the ACS electronics and capturing stationary MEMS data for 30+ minutes. For pretests, short ~5-minute, stationary tests were performed at the beginning of the intended test to check the sensor temperature, rate, and BIT outputs and connections.

Figures 11, 12, and 13 are typical temperature, rate, and BIT output profiles at room temperature and pressure. All profiles agree with results in [2]. The temperature and rate profiles are shown in raw A/D bits. The following sections will show how the conversion process affects these outputs. Since no further examination or compensation was required for the BIT output, it is displayed here in its raw digital output form[4].

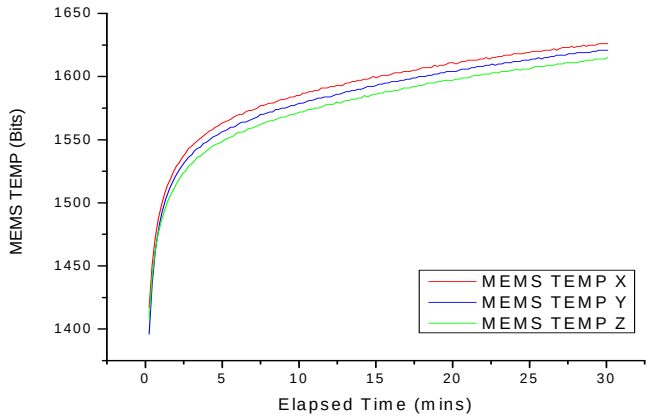

Figure 11. Typical Startup Temperature Profile

The temperature profile shows a nonlinear behavior. Immediately after turn-on up to about 5 minutes, a steep transition can be observed; this period is the warm-up

[4] See Equation **(6)**.

period. Over time, as demonstrated in [2], the graph would naturally follow the ambient temperature and would be cyclical, peaking and bottoming at varying daily temperature highs and lows.

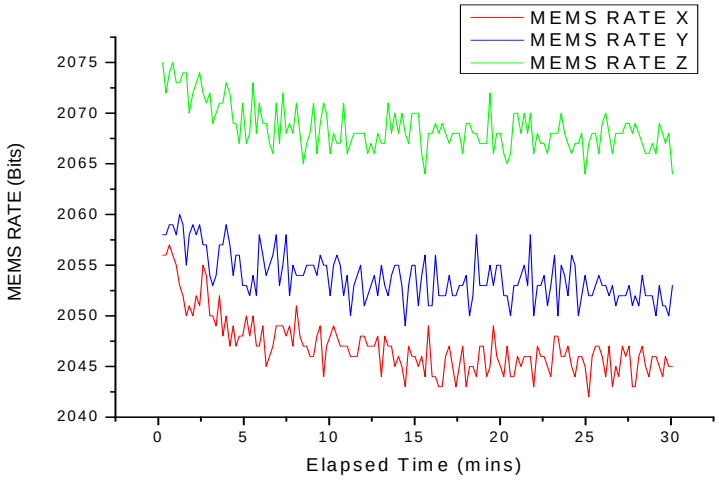

Figure 12. Typical Startup Rate (Bias) Profile

Initial rate transients are also seen immediately after switch-on due to internal heating of the sensor. Under room temperature conditions, the warm-up period seen in the raw A/D output of Figure 12 is approximately from 5 (Z) to 12 (X) minutes. The transition period for each sensor is subject to change with the temperature and humidity conditions of the day. It will also be different in a space environment; internal heating would be faster in vacuum, however, the difference between the starting temperature and operating temperature would be larger, which would result in a longer transition period in vacuum. Using Equation (5), the raw A/D outputs were converted to the equivalent rates. From turn-on until stable, the converted outputs changed by 0.024 °/sec, 0.017 °/sec, and 0.019 °/sec in this particular test. Without correction, these transients settle to X, Y, and Z error averages of -0.006 °/sec, 0.012 °/sec, 0.048 °/sec, correspondingly. These are small but they can be significant in terms of resolving suborbital rates of interest; a small gyroscope bias introduces quadratic errors in velocity and cubic error in the position [19]. It is the goal of the next several sections to reduce these zero rate biases. The warm-up period is a source of error and a possible improvement in the drift compensation for this warm-up period is discussed in the Recommendations Section. For these tests, the

datasets were restricted to t > 5 minutes to simplify the polynomial fitting and data analysis. Note that these biases include orientation-dependent earth rate components, which will be discussed further in later sections.

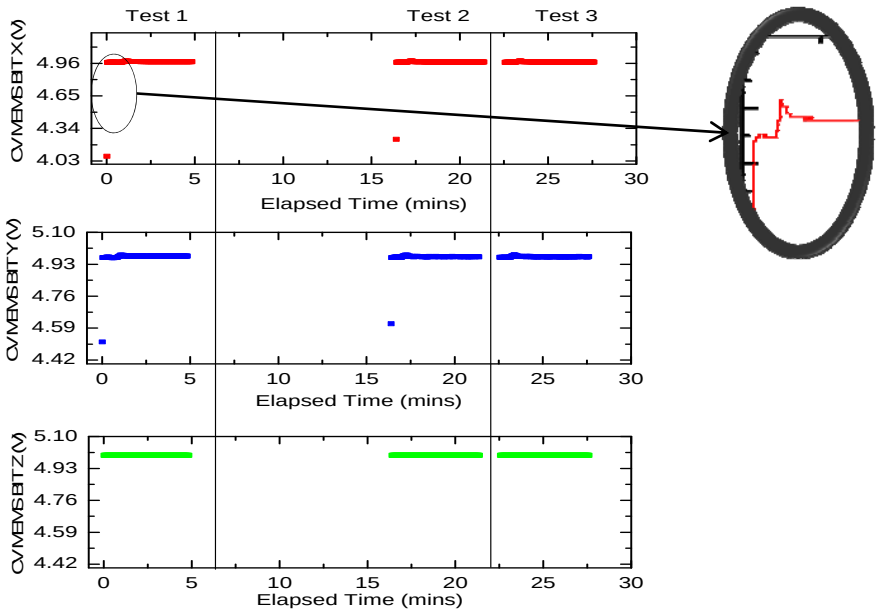

Figure 13. Example of Startup Bit Output

Finally, the BIT outputs, as shown in Figure 13, are all within the requirement of ≥ 2.4 V, indicating that the MEMS are operational. The X and Y BIT outputs display small spikes around the first minute after turn on, and then settles to a constant value; since the output values display above 2.4 V, these spikes do not affect the validity of the BIT data.

B. NOMINAL VOLTAGE TESTS

As described in [2], the spacecraft may perform routine temperature checks of all subsystems on-board. If properly calibrated, the MEMS sensor temperature output to the ACS can be used to compute the actual sensor temperature and to eliminate temperature bias in the rate outputs. Due to the changes in the MEMS assembly, retesting of the sensors was required to determine the nominal voltages and verify that the MEMS temperature output of each sensor is correct.

To determine the nominal temperature voltages of the QRS11 sensors, similar tests were performed as described in [2]. The nominal temperature voltage is defined as the steady state temperature voltage output of each sensor at 25°C. Equation (9) describes the temperature conversion:

$$T = 25°C - \frac{V_n - T_m}{0.0033 * G} \tag{9}$$

where,

T = temperature in °C of the sensor

V_n = nominal voltage value of each sensor[5]

T_m = measured value of the temperature output in Volts

G = new gain of the temperature filter

As mentioned above, the gain G has been changed from $\frac{R4}{R3} + 1 = \frac{120.0\ K\Omega}{10.0\ K\Omega} + 1 = 13$ to $\frac{R4(new)}{R3} + 1 = \frac{70.0\ K\Omega}{10.0\ K\Omega} + 1 = 8$. Hence, the denominator of Equation (9) reduces to 0.0033*8 = 0.0264.

1. Setup

A refrigerator recirculator (Cole Parmer polystat®) and cold plate were used to control the temperature of the sensors. With the MEMS assembly housing removed, thermocouples were attached to each of the three sensors and one to the top surface of the base plate. As shown in Figures 14 and 15, the ACS and the MEMS sensors were set on the cold plate lined with a sheet of thermally conductive elastomer. To offset the internal heating of the sensors when powered on, the recirculator was set at a temperature of 21°C, based on earlier trials, to keep the MEMS as close to 25°C as possible. ACS data was collected over a period of ~7 hours. The thermocouple temperatures were monitored and manually recorded every 15 minutes.

[5] V_n is the T_m value at 25°C.

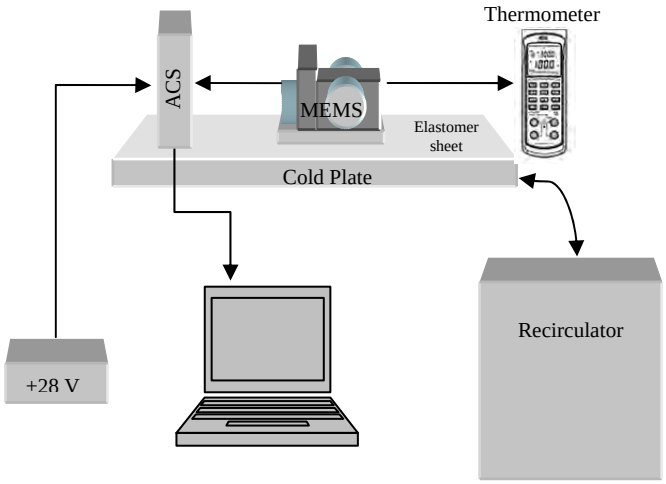

Figure 14. Cold Plate Test Setup

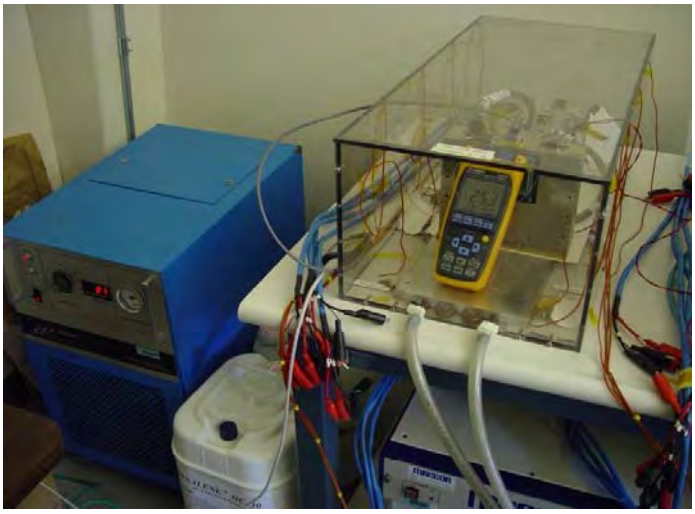

Figure 15. Cold Plate Setup

2. Results

The MEMS outputs are shown in Figure 16 for the total length of the test. Due to the sensitivity of the sensors and the fluctuations in the setup, the extraction of V_n was confined to the most stable region of the test. The region from time t_1 = 120.93 to t_2 = 238.62 mins (~2 hours) was the range used to calculate the nominal voltages of the three sensors. There is a slight slope in the order of 10^{-6} volts/min for all of the lines in this

region. For the purpose of this calibration, this area was considered "flat," recognizing that this could be a source of error and a limitation of the models generated from this experiment (see also Error Sources section). The nominal values were calculated from the raw A/D MEMS temperature output values by first converting to voltage values using Equation (4).

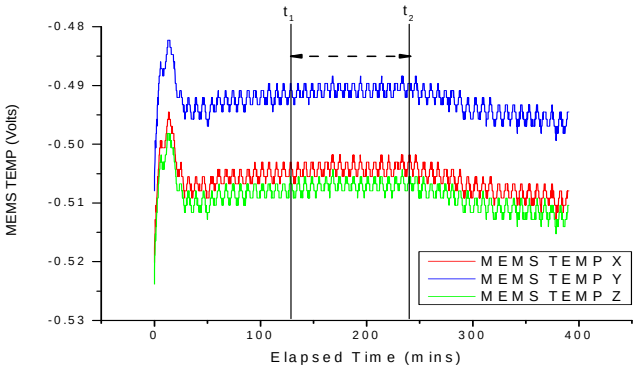

Figure 16. T_m values for the total length of test

T_m values from t_1 to t_2 were then averaged to get the nominal voltage temperature values. The new nominal values along with the corresponding thermocouple temperature average (T_{ave}) are shown in Table 2:

Table 2. New Nominal Voltage Values

Sensor	V_n (V)	STDV V_n (V)	T_{ave} (°C)	STDV T_{ave} (°C)
-X	-0.5042	0.0011	25.7	0.1
Y	-0.4909	0.0011	25.4	0.1
-Z	-0.5071	0.0010	25.3	0.1

To calculate the actual temperature of the MEMS for any value of T_m, Equation (9) was modified for each sensor. The resulting equations are:

$$T_x = 25.7°C + \frac{0.5042 + T_{mx}}{0.0264} \quad (10)$$

$$T_y = 25.4°C + \frac{0.4909 + T_{my}}{0.0264} \tag{11}$$

$$T_z = 25.3°C + \frac{0.5071 + T_{mz}}{0.0264} \tag{12}$$

Using Equations (10) - (12) to convert the MEMS data to °C, the MEMS and thermocouple temperatures were compared as shown in Figure 17. The average difference between the thermocouple and the calculated MEMS temperatures in the "flat" region are: 0.036 °C (-X), 0.034°C (Y), and 0.032°C (-Z). While these results show a very small thermal difference between the MEMS and the calibrating instrument, the precision of this calibration is limited to temperature near or at 25°C. This will be discussed further in the following section.

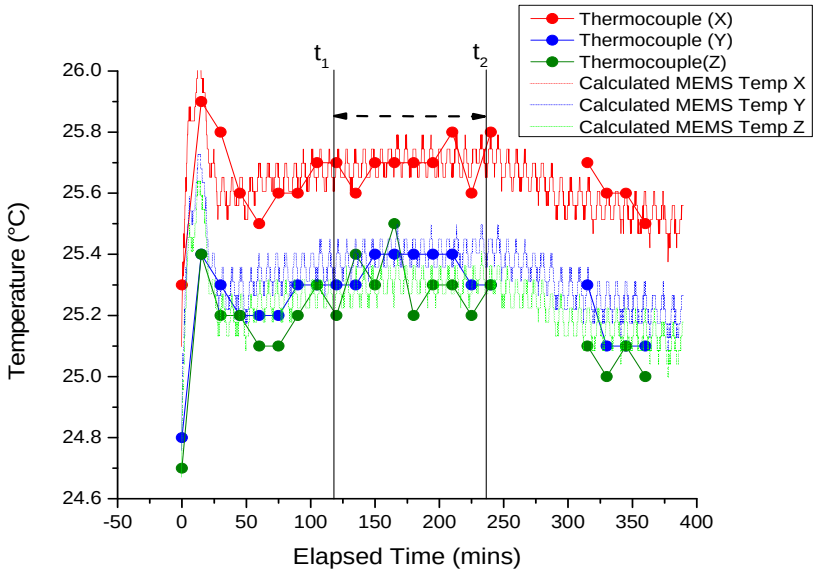

Figure 17. Comparison of thermocouple and calculated MEMS output

3. Limitations of Temperature Model

There are several factors affecting the accuracy of the temperature output calibration. Internal heating of MEMS unit and the thermal gradient between the internal

sensor and the sensor shell where the thermocouples were placed makes a precise calibration difficult. Moreover, Equation (9) assumes a *nominal slope* of +0.0033 V/°C for each sensor. Consequently, output errors can be expected with temperature rise or drop from 25°C. Figure 18 shows a test comparing the MEMS to thermocouple temperatures. The difference between the MEMS and thermocouple seen here is as much as 4°C.

A more extensive calibration process would be required to determine the unique slopes of each sensor by performing additional soak tests at different temperatures to measure the output change of the units per °C. As experienced with the nominal voltage test, stabilization could take several hours to reach. Due to limited time, such tests were not possible. It is, however, not essential to have a precisely calibrated system to perform the ultimate goal of temperature bias compensation. Thus, testing was continued without an accurate temperature output. While not a necessity for space operations, the work performed in this section was very useful in performing the succeeding chamber tests. With issues such as thermocouple adhesion problems and having a limited number of chamber ports, the MEMS temperature output served as a valuable feature for monitoring the unit temperatures during thermal ramp tests.

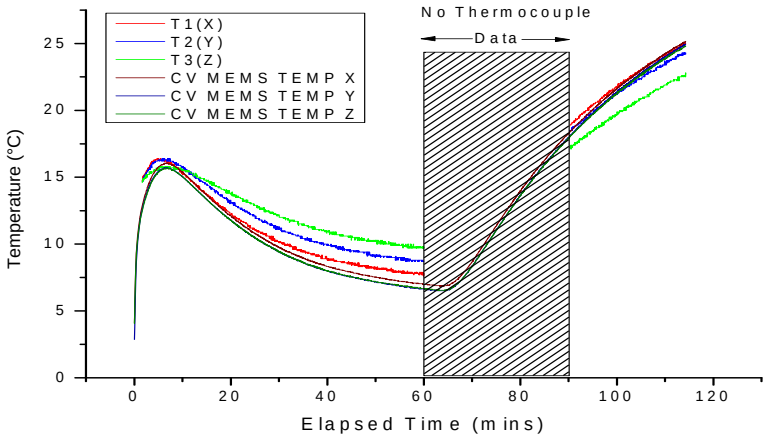

Figure 18. Temperature Comparison

C. THERMAL RAMP TESTING IN AMBIENT PRESSURE

Following the thermal validation, thermal ramp tests were conducted to determine the new temperature-dependent rate bias compensation values for each sensor or the thermal dependent $b_{in\text{-}run}$. Since the dynamic tests involved operating equipment in an ambient environment, separate polynomials were required for ground tests. The polynomials generated in this section/series were used to evaluate data from the rate transfer tests, and pre- and post-vibe functional tests. Similar to the methodology of [2] and [11], the temperature dependence of the sensor rate output was determined by estimating the zero-rate bias over the full qualification range of -29°C to +66°C using a 3rd-order polynomial.

This test series also includes subtests to investigate and address hysteresis effects noted in the tests conducted [11]. While these hysteresis tests were being conducted, rate bias offsets were observed with magnitudes correlated to the startup temperature of the MEMS and electronics. Thus, in conjunction with the hysteresis tests, experiments were run at different starting temperatures to investigate the aforesaid effect.

1. Setup

Due to the different test temperatures, two setups were required to perform the tests in this series: a thermal vacuum chamber (TVAC) setup and a cold plate with recirculator setup. The thermal vacuum chamber was required to meet the full qualification range. On the other hand, the cold plate with recirculator allowed for better temperature control that could not be performed as well by the TVAC.

a. Thermal Vacuum Chamber Setup

The MEMS assembly and ACS were placed in the thermal vacuum chamber shown in Figure 20. The chamber temperature was pre-heated or pre-cooled to the test temperature. The electronics were kept off during the pre-heating period to prevent overstressing the electronics in the event that the TVAC heater overshoots the temperature set point. Thermocouples were used to monitor the MEMS mounting blocks. The electronics were occasionally turned on to check the actual MEMS readout (which

was approximately ±16°C compared to the mounting block). All vent valves were open during tests to keep the chamber at ambient pressure during data collection. The chamber operation by test is as follows:

1. *Thermal Ramp*. For this test, the chamber was preheated so that the MEMS temperature output read +66°C. Then, the chamber temperature was slowly lowered to -29°C while collecting data.

2. *Hysteresis Test*. The temperature was set to the test temperature then reversed up or down while collecting data to determine if the MEMS rate bias output path is reversible.

3. *Repeatability Test.* To test the repeatability of the output with the turn-on temperature, several runs were conducted at different starting temperatures. The chamber temperature was either raised or lowered depending on the startup temperature while collecting data.

The temperature details for the hysteresis and repeatability tests can be found in Appendix B. To avoid inducing noise into the system, data was only recorded in between cooling or heating cycles when the main switch and refrigeration or heater was off.

Figure 19. Thermal Vacuum Chamber

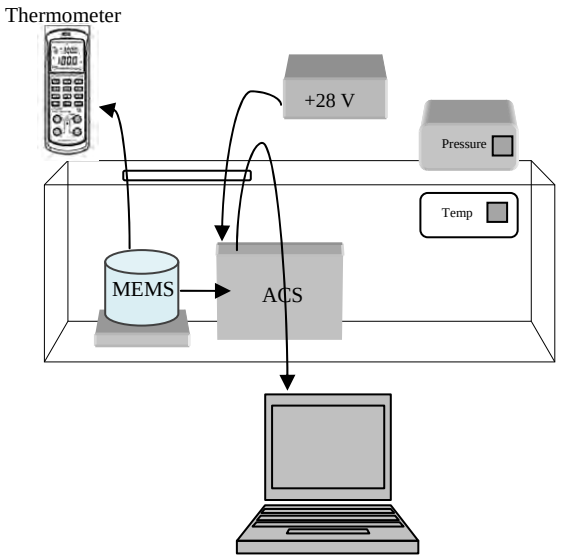

Figure 20. TVAC Test Setup

b. Cold Plate and Recirculator Setup

The refrigerator recirculator and cold plate test setup described in the Nominal Voltage setup was used for hysteresis and startup tests at different temperatures near or within the operating range. Similar to the TVAC operation, the temperature controller was set at the test temperature, lowered or raised, and then reversed (for hysteresis). Data was captured during the thermal ramp up/down.

2. Results

a. Hysteresis Test Results

Path misalignment of up to 0.004 °/sec was observed from the total of five hysteresis tests conducted. The path irreversibility observed in these tests occurred randomly, and was seen both before and after the conversion from raw A/D bits to voltage. This indicates that the variable R_{shift} used in the conversion process may also be affected by the temperature reversal, sometimes causing a shift in the voltage converted values. Sample results from run Recirc2–1 are shown in Figure 21. Each of the top MEMS temperature vs. MEMS Elapsed time plots shows the MEMS temperature reversal with time. The middle plots are Rate bias vs. MEMS temperature in bits and the

bottom plots show the equivalent plots in the unit of volts. Notice that in column 1, the path of the X zero-rate output is reversible in bits but not in the voltage converted form. On the other hand, the opposite is observed in column 2, where the Y rates in bits do not converge at the left endpoints while the rates in voltage form meet at the endpoints. The plots for the rest of the tests can be found in Appendix D.

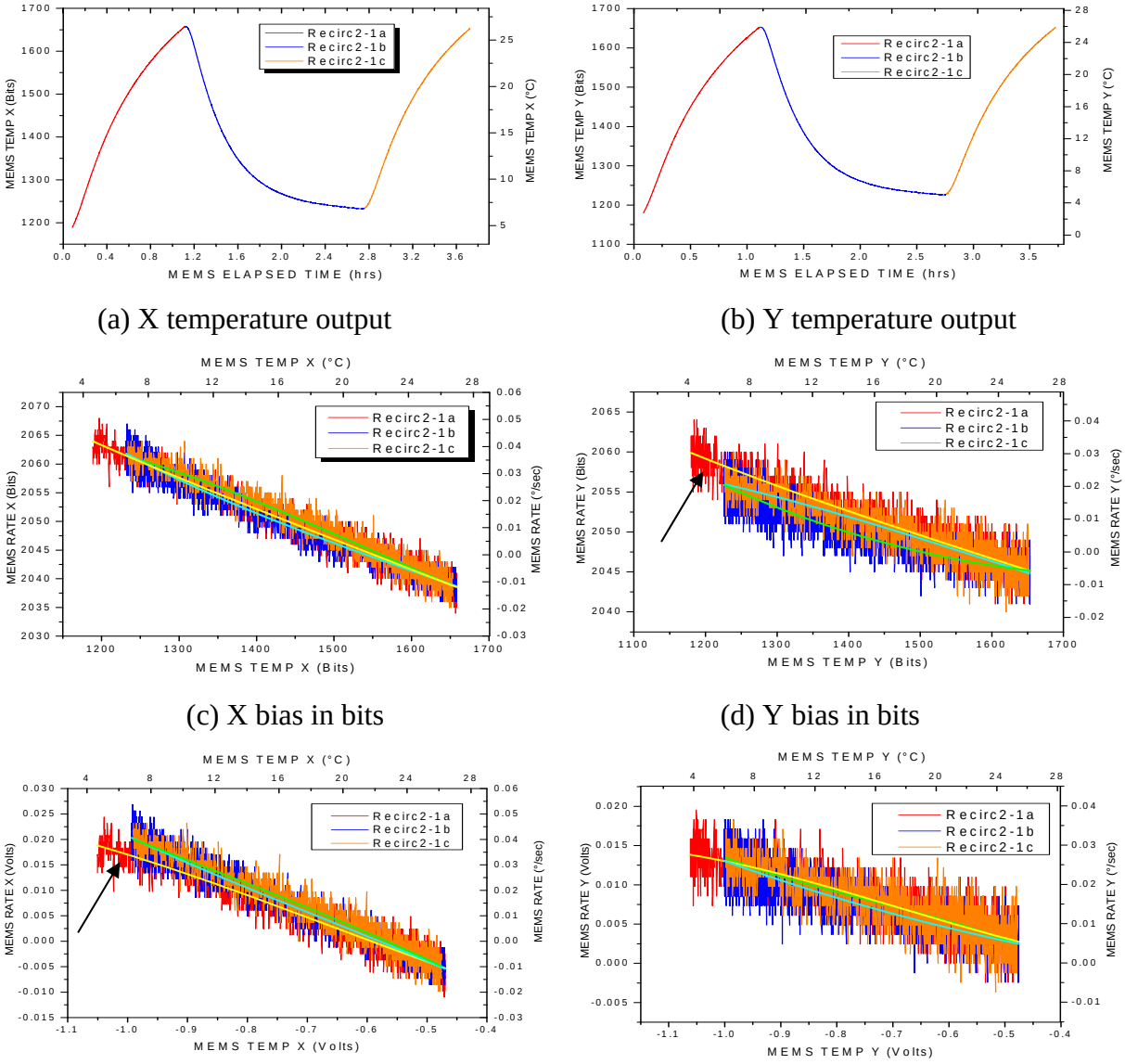

(a) X temperature output

(b) Y temperature output

(c) X bias in bits

(d) Y bias in bits

(e) X bias in volts

(f) Y bias in volts

Figure 21. Column 1) Rate bias hysteresis result for X sensor showing path misalignment after voltage conversion and column 2) Y sensor showing path misalignment before voltage conversion

Since the misaligned plots of Figure 21 (d) and (e) show that two of the three segments in each plot coincide and that the two 'overlapping' segments are warm up and cool down paths, it can be deduced that the random misalignment of the first warm up segment is not due to hysteresis effects.

b. Effect of Startup Temperature on the MEMS Rate Bias

Rate bias offsets were observed in the raw A/D output with magnitudes correlated to the startup temperature of the MEMS and electronics. Similar effects were also observed on the variable R_{shift}, which is used for the conversion of the raw rate output from bits to voltage. While determining the source of these offsets require further study, the variation in R_{shift} indicates that the error source is at the board-level and not directly due to sensor inconsistencies. Other possible explanations are: 1) replication errors and 2) power regulator fluctuations. Nonetheless, the more important point is that these variations are reduced after applying Equation (5). Column 1 of Figure 22 shows several curves with different offsets result when the electronics are started at different temperatures. On the other hand, column 2 of Figure 22 shows that upon conversion, the rate bias offsets with the startup temperature are reduced to millivolts, as demonstrated by the nearly overlaid curves. The R_{shift} temperature dependence is shown in Figure 23. The changes in the R_{shift} are proportional to the changes in the raw A/D bit rates. So, most of the error is corrected during the conversion process using Equation (5). Initially, it was thought that the compensation polynomials could be derived directly from the raw A/D bits to avoid conversion errors. In contrary, the results here show that the compensation polynomials are better derived using the converted values, as done in the following sections.

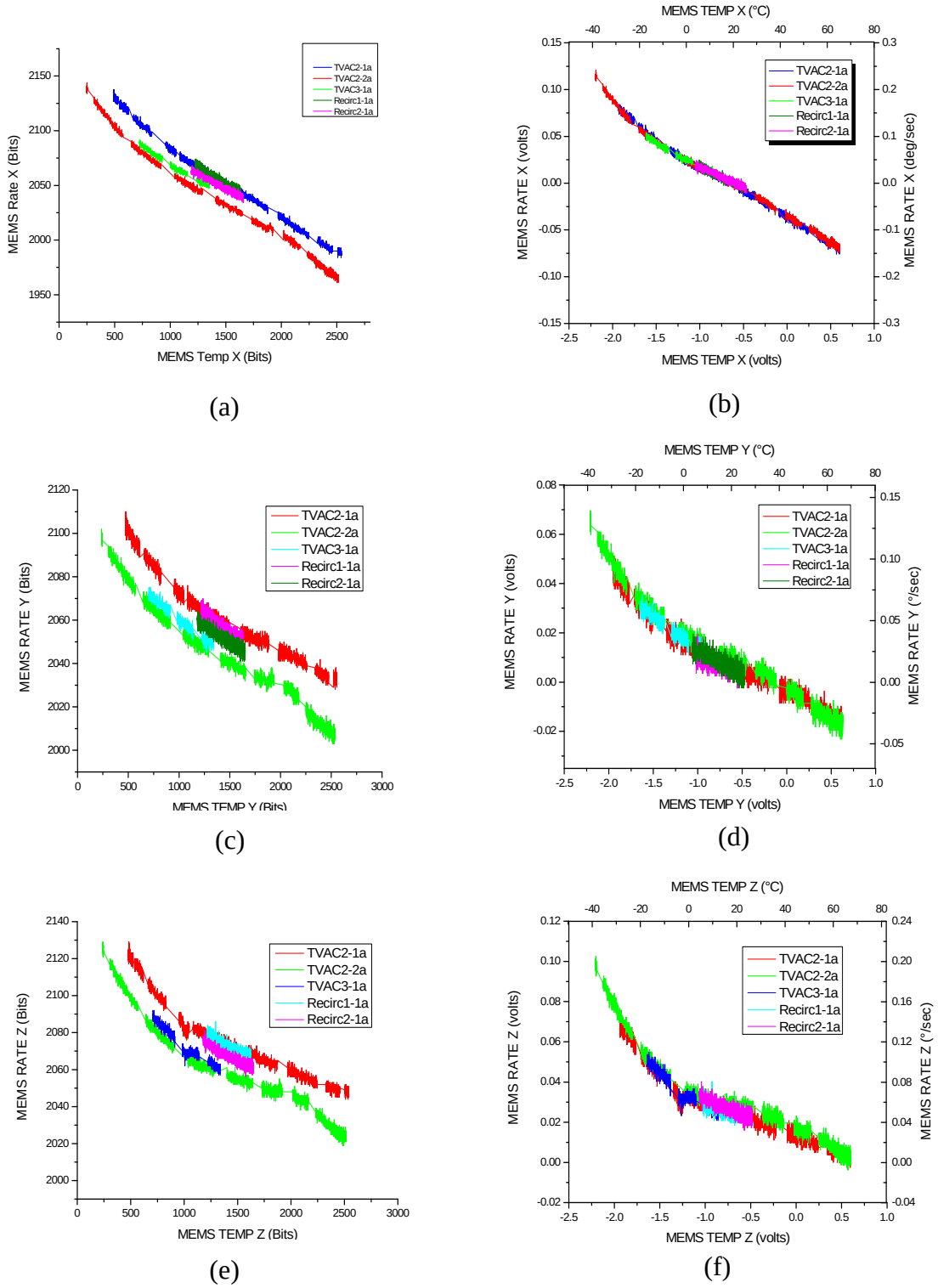

Figure 22. Sensor startup temperature effects on rate bias: (a,c,e) as seen in raw output form, and (b,d,f) after conversion to volts with R_{shift} correction

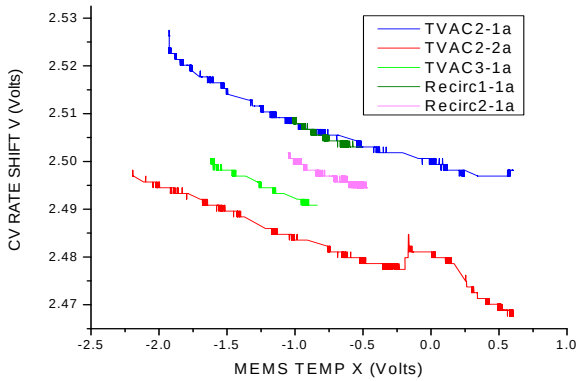

Figure 23. R_{shift} Dependence on Temperature

c. Polynomial Generation

The rate bias compensation polynomials are required to span the entire qualification range. Recall from the previous section that there are two data sets that meet this criterion, TVAC2–1a and TVAC2–2a. While these two data sets span the entire range, it is the Recirc1–1a data that represents the closest startup conditions during ground tests. Being "in line" with the Recirc1–1a raw data, TVAC2–1a was selected to generate the generic polynomials to minimize residual conversion errors. The polynomials for the rate bias vs. temperature plots are shown in Figure 24. The polynomial fits are in the form of $y = B + m_1 * T_m{}^1 + m_2 * T_m{}^2 + m_3 * T_m{}^3$, with the constants shown in Table 3. The thermal ramp curves are fitted in the units of volts instead of °C and °/sec to allow for later changes or fine-tuning of the MEMS Temperature output conversion equations without impact on the compensation equations. For NPS SSAG use, the constants are also provided in units of °/sec vs. °C in Table 4. The number of significant digits was kept as generated by the software. In general, the thermal ramp profiles of the Y and Z sensors are parallel to one another. On the other hand, a larger bias change is observed with temperature change for the X sensor; this is consistent with the results in [2] and the manufacturer specifications sheet, which provides the highest bias stability vs. temperature value for the X sensor (+0.266 °/sec) compared to Y (+0.121°/sec) and Z (0.118 °/sec). The temperature sensitivity difference

between sensors may be attributed to manufacturing variations as MEMS devices may vary slightly from batch-to-batch, even device-to-device due to the nature of MEMS fabrication processes.

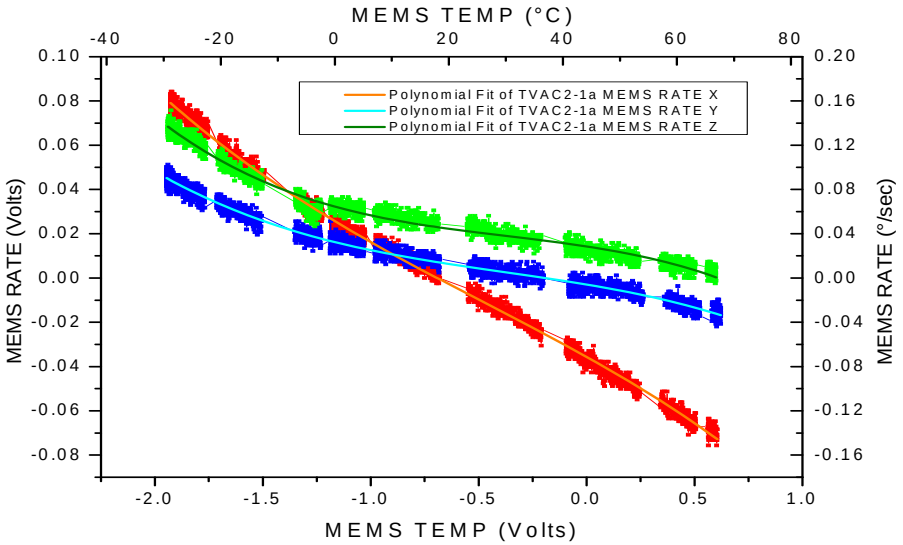

Figure 24. Thermal-dependent in-run biases for polynomial generation

Table 3. Cubic Bias Compensation Values in Volts (for ground tests)

Sensor Bias	Variable	Value (V)	Standard Error (V)	Residual Sum of Squares	Adj. R-Square
X	B	-0.03562	7.29979E-5	0.0206	0.99775
	m_1	-0.05444	1.24357E-4		
	m_2	-0.00816	2.40767E-4		
	m_3	-0.00560	1.03657E-4		
Y	B	-0.00295	7.14013E-5	0.01962	0.98721
	m_1	-0.01634	1.16579E-4		
	m_2	-0.00622	2.25414E-4		
	m_3	-0.00542	9.68825E-5		
Z	B	0.01428	8.37201E-5	0.0272	0.9855
	m_1	-0.01493	1.44301E-4		
	m_2	-0.00899	2.76961E-4		
	m_3	-0.00808	1.18105E-4		

Table 4. Cubic Bias Compensation Values in °C vs. °/sec (for ground tests)

Sensor Bias	Variable	Value (V)	Standard Error (V)	Residual Sum of Squares	Adj. R-Square
X	B	0.05232	1.29755E-4	0.0824	0.99775
	m_1	-0.00309	4.7811E-6		
	m_2	1.61507E-5	2.07221E-7		
	m_3	-2.06176E-7	3.81454E-9		
Y	B	0.03262	1.26206E-4	0.07846	0.98721
	m_1	-0.00127	4.66779E-6		
	m_2	1.7812E-5	1.92079E-7		
	m_3	-1.99291E-7	3.56523E-9		
Z	B	0.06502	1.48798E-4	0.10881	0.9855
	m_1	-0.00144	5.53673E-6		
	m_2	2.71648E-5	2.32928E-7		
	m_3	-2.97345E-7	4.3462E-9		

The residual biases or curve fitting errors were found by subtracting the results of the cubic function to the original rates. The results are plotted in Figure 25. The average mean values and corresponding standard deviations are:

$\bar{X} = -1.0901\text{E} - 6$ V, $\text{STDV}_X = 0.0022633$ V

$\bar{Y} = -6.9658\text{E} - 7$ V, $\text{STDV}_Y = 0.0022091$ V

$\bar{Z} = 4.6997\text{E} - 16$ V, $\text{STDV}_Z = 0.0026016$ V

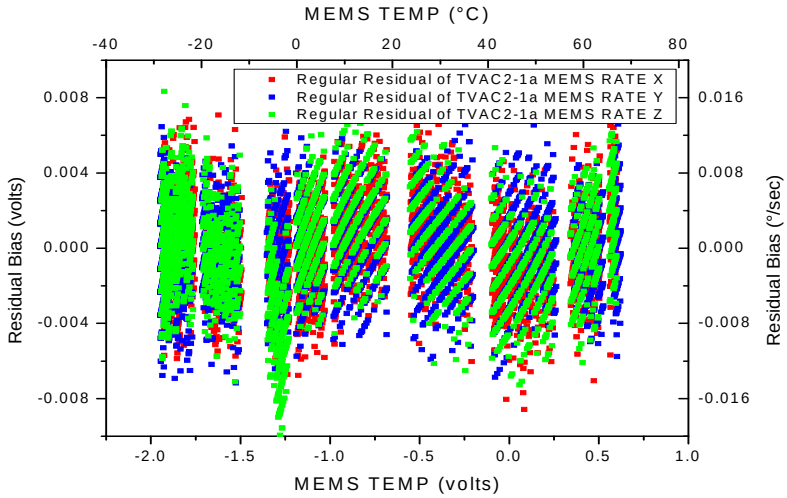

Figure 25. Curve Fit Residual Plots

The residual plots and averages above represent only the goodness of fit of the generated polynomials to the TVAC2–1a X, Y, Z data sets. There are other systematic and random errors in the system, which cannot be easily discerned and cannot be entirely eliminated or compensated for; these would appear as a small initial bias after compensation. Moreover, the polynomials in Table 3 and 4 incorporate earth rate components relative to its particular position inside the TVAC. The sensor orientations would inevitably change between tests. These effects are especially worse for the X & Y, since the orientation angles could vary up to 90°. The worst-case errors due to the component of the earth's rotation *Er* are estimated to be (see Appendix L for details):

$$\begin{aligned} Er_Z &= Er * \cos(53.6°) \\ &= 0.0042°/\text{sec} * \cos(53.6° \pm 3°) \\ &= 0.0025\,°/\text{sec} \pm 0.0002\,°/\text{sec} \end{aligned} \tag{13}$$

and,

$$\begin{aligned} Er_{X,Y} &= Er * \cos(36.4° \pm 90°) \\ &= 0.0042\,{}^{\circ}\!/_{\text{sec}} * \cos(36.4° \pm 90°) \\ &= 0.0034\,°/\text{sec} \pm 0.0034°/\text{sec} \end{aligned} \tag{14}$$

d. Algorithm Testing

To test the polynomials, the compensation was applied to data collected while the MEMS unit was at a stationary position and on a level surface for ~25 minutes. The results are plotted in Figure 26 with the following averages:

X Bias: Mean = 0.0049254 °/sec STDV = 0.0036929 °/sec
Y Bias: Mean = -3.4307E-4 °/sec STDV = 0.0048543°/sec
Z Bias: Mean = 0.0093707 °/sec STDV = 0.004325 °/sec

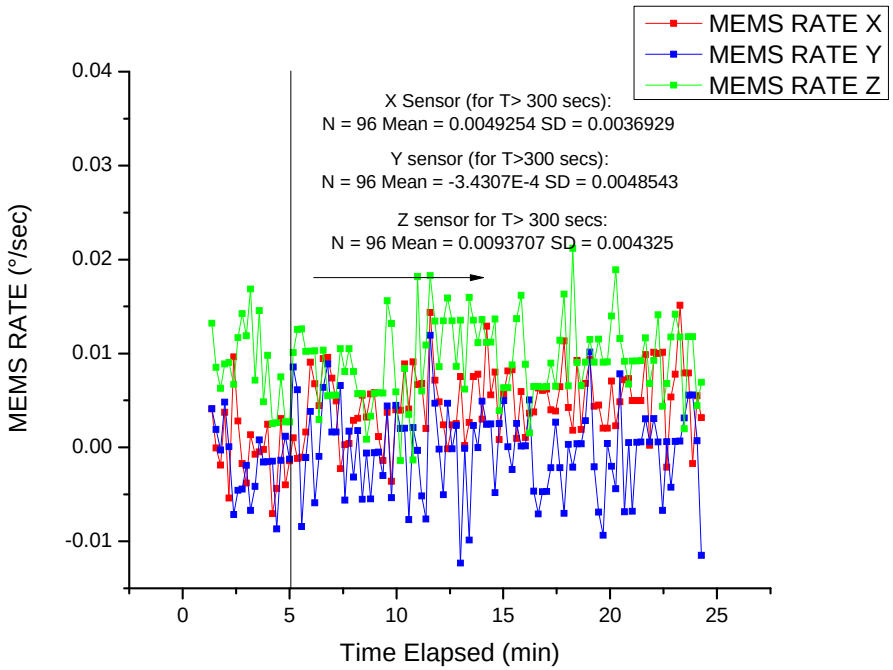

Figure 26. Residual bias after compensation

Calibration or compensation does not eliminate error but only reduces it. In [19], a comparison of calibration methods revealed that the thermal ramp method is the least effective at reducing bias drift compared to soak and multi-position tests. Due to facility and time constraints, the tests here employed the thermal ramp method. As follows, residual biases were observed after thermal compensation, as shown in the above results. These errors also include data reduction errors, earth rate effects, misalignment, and other error sources described in Section II-B. Without filtering or the use of other estimation techniques, the resolution is limited by this bias. In Section E, rate transfer tests will estimate and quantify the output errors due to this bias. First, we proceed with vacuum tests to produce the actual spacecraft polynomials.

D. THERMAL RAMP TESTING IN VACUUM

As discussed in Chapter I, the MEMS unit is planned to be flown unpressurized because pressure changes results in a changing rate bias and there is no system capability to verify the pressure integrity of the MEMS unit in-orbit. Chamber tests were conducted to determine the vacuum effects on the rate output. The first series of tests were performed to determine the noise levels from the test setup. The second and main test series of this section are the thermal ramp tests under vacuum. The third and final tests were longer-term vacuum tests while maintaining the vacuum at $< 10^{-5}$ Torr.

The MEMS and ACS were placed in the thermal vacuum chamber and the chamber was pumped down to the pressure levels desired for each test. The test setup and temperature controls operation are the same as the Thermal Ramp in Ambient Pressure tests.

1. Noise Test

The mechanical pump was identified as the biggest source of physical noise in the TVAC setup [2], [23]. To quantify the noise induced by the pump to the MEMS output, two ~30-minute long tests were performed: one test was run with the mechanical pump on and another with the mechanical pump off. Ideally, the pressure would be constant in these two tests to make a direct comparison of the noise levels. In the effort of doing so, the "pump on" test was conducted with the isolation, mechanical pump, and TVC vent valves open. Even with all the valves open, however, the pressure still decreased by 260 Torr. Once the pressure stabilized (observed at 190 Torr), the ACS was turned on to record data. For the "pump off" test, all valves were closed before turning off the pump to keep the pressure as close to that of the "pump on" test. ACS data and pressure were then recorded. During this test, the pressure raised 60 Torr, from 190 Torr to 250 Torr. The results of the two tests are shown in Figures 27 and 28.

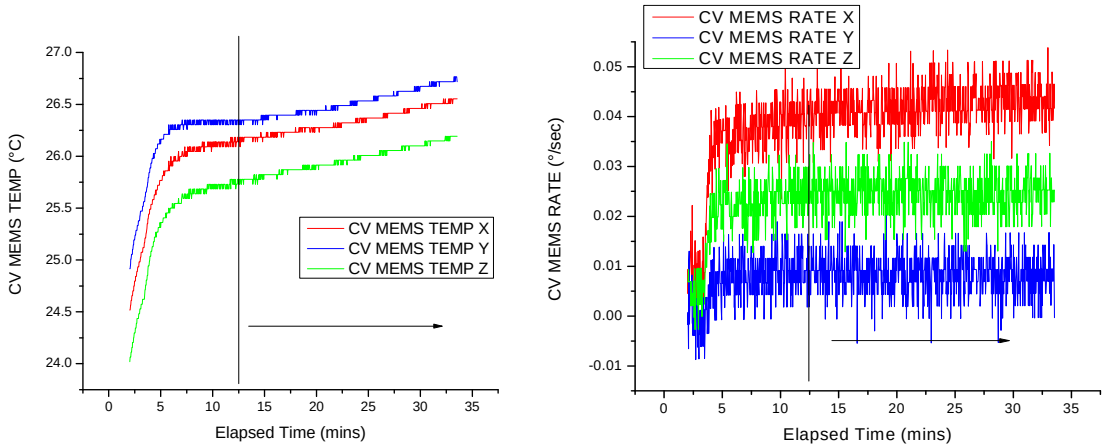

(a) Temperature (b) Bias

Figure 27. Pump On Test Results

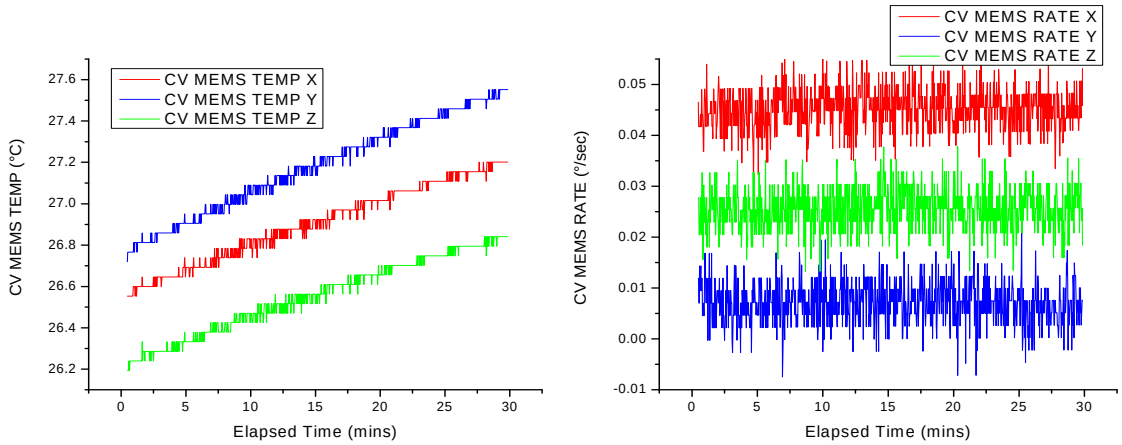

(a) Temperature (b) Bias

Figure 28. Pump Off Test Results [6]

In the "pumps on" test, the X sensor displays a longer stabilization time than the Y and Z sensors. This particular behavior is consistent with the sensitivity of the X sensor rate with temperature, as seen in the steeper slope of the X rate plot of Figure 24 in the ambient thermal ramp section. This will have to be addressed for spacecraft operations. For the purpose of this noise test, the comparison is limited to the Y and Z sensor. The results are summarized in Table 5.

[6] In this test, CV MEMS RATE is the temperature compensated using the ambient pressure polynomials. This will be redefined to include compensation for pressure bias further into this section. Note that the final form of the output will include compensation for factors described in II-B.

Table 5. Noise Test Results

Test	$\bar{Y}_{CV}$ (°/sec)	$\bar{Z}_{CV}$ (°/sec)	$S_{\bar{Y}_{CV}}$ (°/sec)	$S_{\bar{Z}_{CV}}$ (°/sec)
Pump On	0.0083331	0.024716	0.0041827	0.0039689
Pump Off	0.0070684	0.025776	0.0042413	0.0041927

In addition to the mechanical pump test, a simple test was run to determine the noise contribution from the TVC main power; this produced the same minuscule difference between *on* and *off* outputs as the pump test. While there are other remaining noise sources in the system, such as the turbo pump and refrigeration, isolating each noise contributor was not possible due to a limited test time. Thus, we have proceeded with the next tests based on available data from the tests performed in this section; mechanical noise was considered negligible.

2. Testing at Different Vacuum Degrees

Prior to the thermal ramp testing in vacuum, it was not known how much the TVAC vacuum levels would vary during the temperature ramping. Initial calculations at a 560 km spacecraft altitude showed a vacuum level < $1x10^{-5}$ Torr, which was difficult to maintain at a constant in the TVAC. However, literature searches show that small changes in vacuum levels are not likely to cause drastic changes on the sensor output, even though that the QRS11 is pressure-sensitive.

As discussed in [25], the impedance of quartz oscillators has a pressure dependence described by

$$Z = \left(\frac{2\eta_o V^2 cos\theta}{A^2}\right) * f \tag{15}$$

where Z is the impedance of the oscillator due to an ambient gas, V is the driving voltage of the oscillator, η_o is the conversion efficiency of the electric energy to the mechanical energy, θ is the phase difference between voltage and the current, A is the amplitude of the forced vibration, and f is the coefficient of friction drag force. Equation (15) is based on the string of beads model of a tuning fork shown by Figure 29:

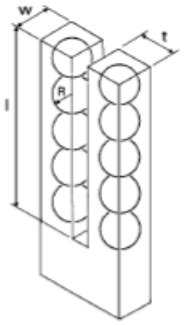

Figure 29. String of Beads Model of a Tuning Fork (From [25])

At the molecular flow region, the coefficient *f* is described by:

$$f = R^2\sqrt{8\pi M/R_0 T} * P \tag{16}$$

where *R* is the radius of the sphere, which is nearly equal to the thickness of *t* of the fork, *M* is the molecular weight of an ambient gas, R_o is the gas constant, *T* is the temperature, and *P* is the pressure.

Due to their sensitivity to pressure, quartz tuning fork oscillators have been studied and developed as friction vacuum gauges [25], [26]. However, in [26], low pressure tests have been conducted down to 7.5E-5 Torr and the results showed that the sensor impedance changes decreases with pressure; impedance is around 345 kΩ to 346 kΩ from 7.5 Torr to 7.5E-5 Torr. Much of the output changes are expected to be seen at higher pressures [27]. This is supported by the results in [11], where the effects of vacuum were found to be relatively fixed bias offsets. Thus, having this supporting information provided confidence in the test methodology in producing the spacecraft polynomials.

As preparation for the thermal ramp tests, short tests were performed to verify the test setup and estimate the output deviations due to pressure variation. The temperature compensation algorithm generated in the ambient pressure tests[7,8] were applied to the

[7] This test used a preliminary temperature algorithm derived from TVAC1-1a; the compensation values are similar to the flight values. For the purpose of this test, the TVAC1-1a polynomial is a reasonable estimate and substitute.

[8] The chamber pump down reached to 10^{-7} Torr. However, this data was for MEMS ELAPSED TIME < 5 minutes, and thus dropped to be consistent with previous tests.

sensor output to correct for temperature-related rate bias. Prior to testing, the chamber was baked out at 100°C for ~2 days. All parts needed for the test were also vacuum-baked at 70°C for ~4 hours to rid of any moisture and out gassing, which could degrade the vacuum during testing. To vary the degree of vacuum, the TVAC was operated with different combinations of mechanical pump, turbo pump, subzero cooling, and/or feeding liquid N_2 into the cold trap[9]. Figure 30 shows the bias vs. pressure plot.

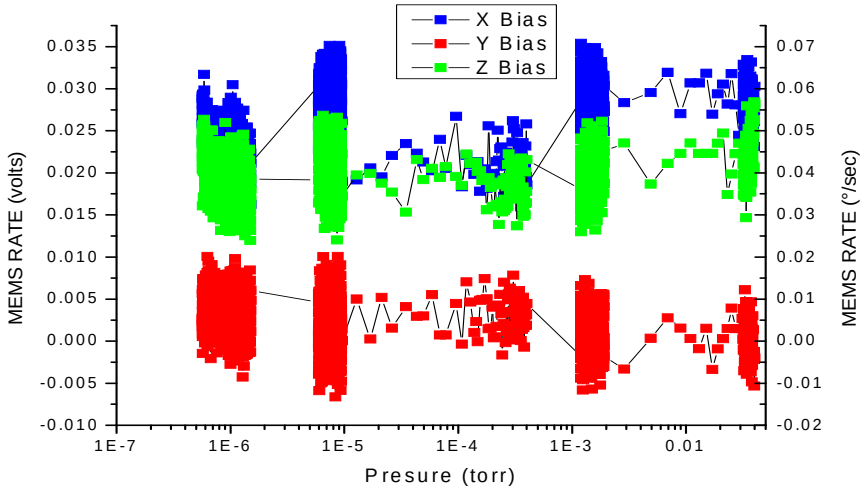

Figure 30. Rate (in-run bias) vs. Interpolated Pressure

The bias plots were divided in six regions, as shown in Table 6 with the corresponding means and standard deviation of the means for the three sensors. These results represent the estimated bias offset due to the degree of vacuum.

[9] Turbo pump cannot be operated without mechanical pump; LN2 cannot be used without turbo and mechanical pump.

Table 6. Pressure Bias Test Results

Pressure Range (Torr)	N Total	X Sensor		Y Sensor		Z Sensor	
		$\bar{X}_{CV}$ (V)	$S_{\bar{X}_{CV}}$ (V)	$\bar{Y}_{CV}$ (V)	$S_{\bar{Y}_{CV}}$ (V)	$\bar{Z}_{CV}$ (V)	$S_{\bar{Z}_{CV}}$ (V)
5.7E-7 to 1.5E-6	1680	0.02221	5.63582E-05	0.00327	5.07468E-05	0.01893	5.47E-05
5.9E-6 to 1E-5	2798	0.02808	4.29143E-05	0.00209	4.44267E-05	0.02039	4.1E-05
1E-5 to 1E-4	10	0.02211	0.000727324	0.00297	0.000743135	0.01949	0.000632
1E-4 to 4E-4	66	0.02091	0.000263416	0.00291	0.000252338	0.01834	0.000266
1E-3 to 2E-3	977	0.02899	6.59052E-05	9.07E-04	6.46255E-05	0.01942	6.94E-05
2E-3 to 1E-2	4	0.02921	0.00105	3.27E-04	0.00132	0.02141	0.00104
1E-2 to 4E-2	176	0.02821	0.000168846	5.63E-04	0.000162062	0.0218	0.000176

The sensor offsets under vacuum generally remained constant from 1E-4 Torr and lower. If there were any variation in the vacuum levels during the actual thermal ramp test, it would be in these levels. With the results of the Noise tests and this section, we proceeded with the thermal ramp testing and polynomial generation assured that the effects of setup-related factors are at a minimum.

3. Thermal Ramp Tests in Vacuum

The thermal ramp test setup and procedure is the same as the ambient pressure test with the additional step of turning on the mechanical and turbo pumps. The chamber was pumped down to 10^{-5} Torr and pre-heated to +66°C. Once the desired temperature was reached, the temperature was lowered to -29°C. ACS and MEMS data were recorded in between cooling cycles.

a. Hysteresis Testing, Conversion to Volts, and Effect of Different Startup Temperatures in Vacuum

For completeness, the characterization tests performed prior to the thermal ramp testing in ambient pressure were repeated under vacuum. The results are consistent with the ambient hysteresis test results. As shown by the two overlapped segments in Figure 31, no hysteresis was observed in vacuum. The small misalignments of the fitted lines are due partially to random errors and partially to curve fit errors.

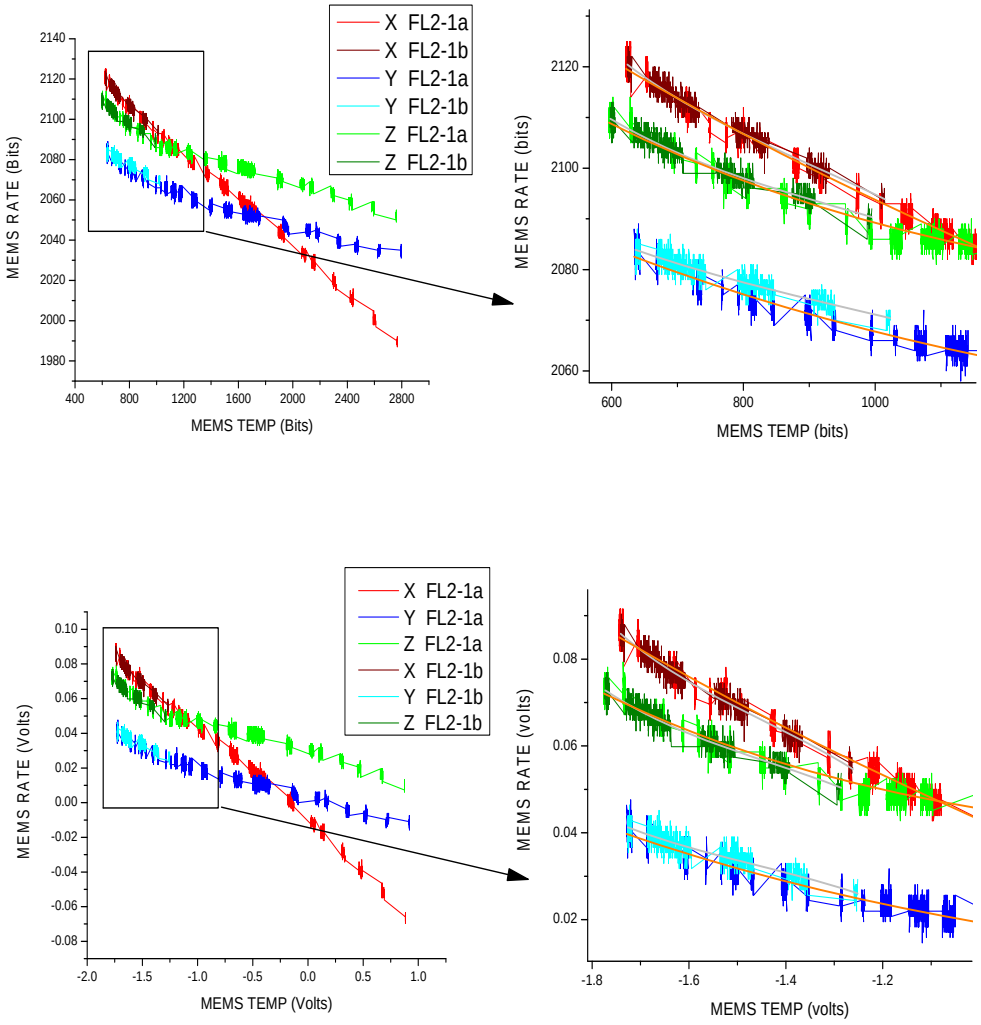

Figure 31. Hysteresis (thermal and pressure in-run bias) test results in vacuum (row 1 in bits and row 2 in volts)

Figure 32 show plots of sensor data started at different temperatures. The X, Y, and Z data are separated in different plots to ease the comparison; the first column displays the rate output in bits while the second column is shown in volts. Similar to that seen in ambient tests, the offsets observed in the raw A/D rate output are reduced after voltage conversion.

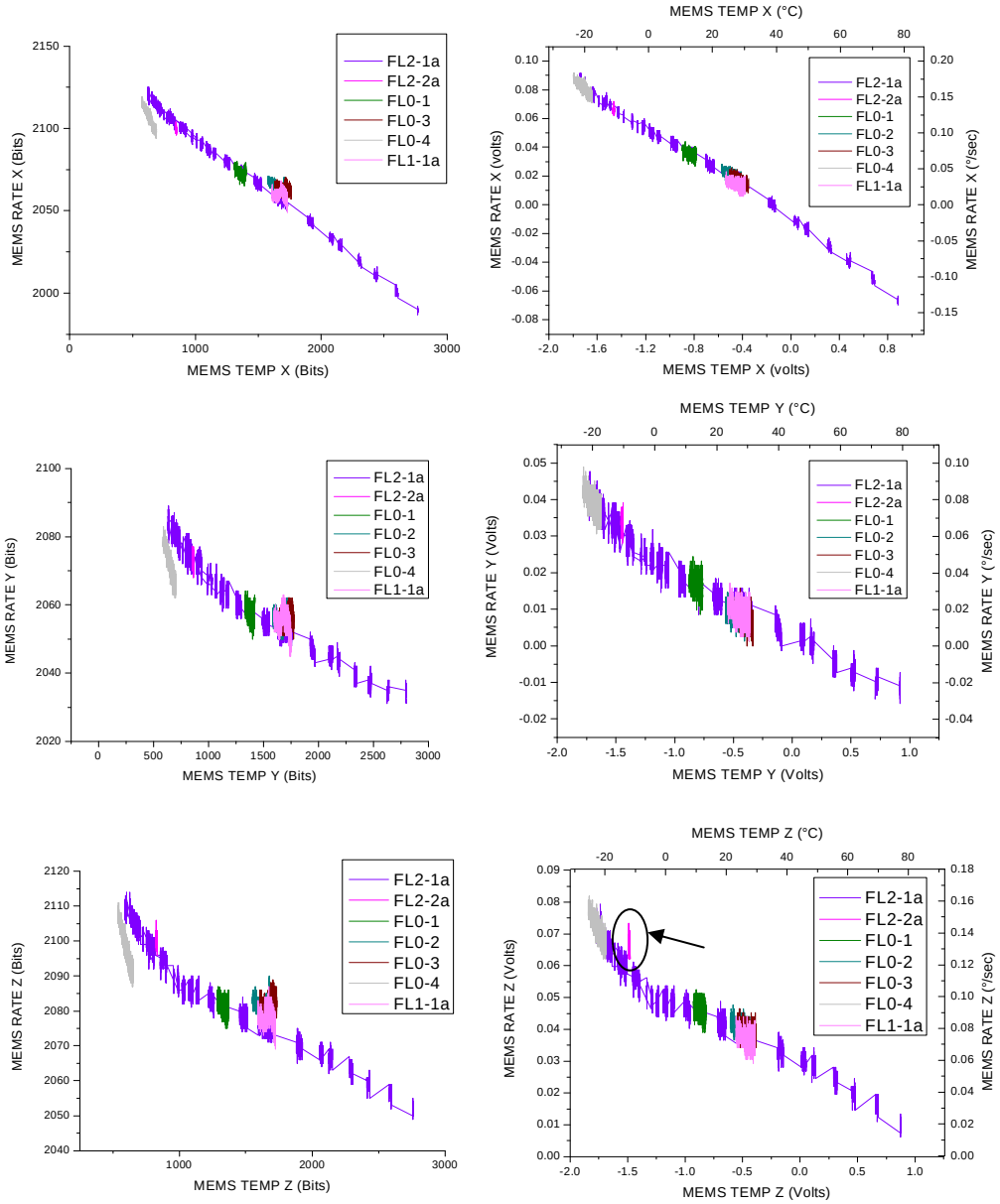

Figure 32. Startup temperature effects/run-to-run bias (column 1) and correction after conversion (column 2)

Figure 33 shows a comparison of the ambient (TVAC2–1a) and vacuum thermal ramp data (FL2–1a). The raw outputs (a) start at a relatively constant offset from each other; the offset is due to difference in pressure and starting temperature. As the temperature is lowered, we see the vacuum data drift from the initial fixed offset. After voltage conversion (b), the drift in offset is reduced and the two data sets are once again

relatively parallel. Also plotted is FL2–3a data, which is part in ambient and part in vacuum to show the repeatability of the tests. Although the correction during voltage conversion reduces the variation, errors of up to ~0.016°/sec may still occur in both ambient and vacuum environments. This is shown in (b), where one can see that the ambient end of the data is not completely in line with the TVAC2–1a data set. Similarly, in the vacuum data of Figure 32, notice that FL2–2a (Z) was also not affected or corrected by the conversion process.

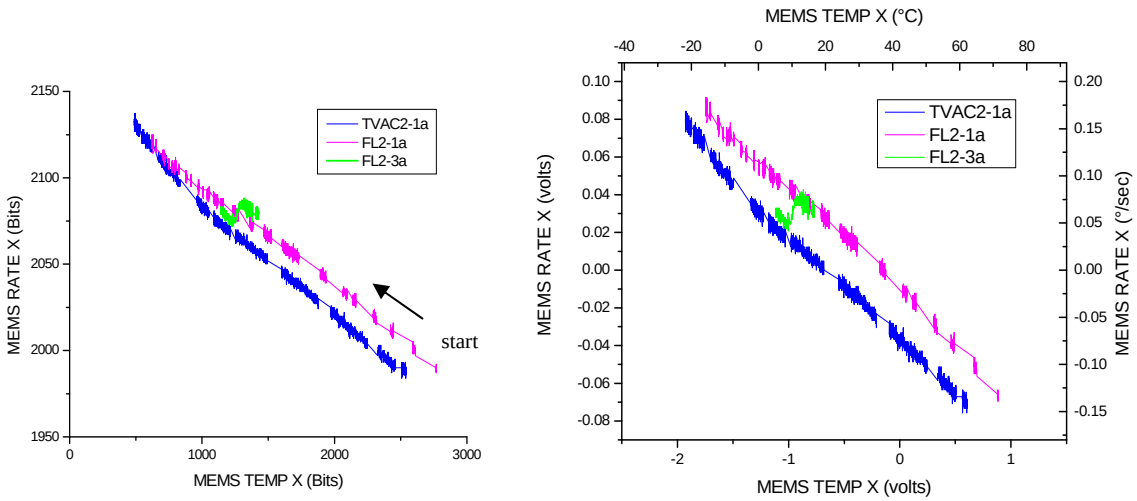

(a) (b)

Figure 33. Comparison of ambient/TVAC2–1a and vacuum/FL2–1a Thermal Ramp data (in-run bias): a) before and b) after conversion. FL2–3a data set shows half in ambient and half in vacuum.

b. Polynomial Generation

The spacecraft polynomials were generated using the FL2–1a data, as shown in Figure 34. The polynomial fits are in the form of $y = B + m_1 * T_m{}^1 + m_2 * T_m{}^2 + m_3 * T_m{}^3$ with the constants shown in Table 7 in volts and Table 8 in C vs. °/sec. As established in the Vacuum degree testing section, the effects of changes in pressure can be approximated by a constant. Hence, these polynomials will compensate for the changes in temperature, again represented by the variable T_m and the pressure dependent bias, which is now included in the constant B. By comparing the B constants of Table 8 to the ambient results in Table 4, one can see that the ambient polynomials acquired

additional biases of ~0.05°/sec, ~0.01°/sec, ~0.03°/sec for X, Y, and Z, The additional bias shifts due to pressure change are shown in Figure 35.

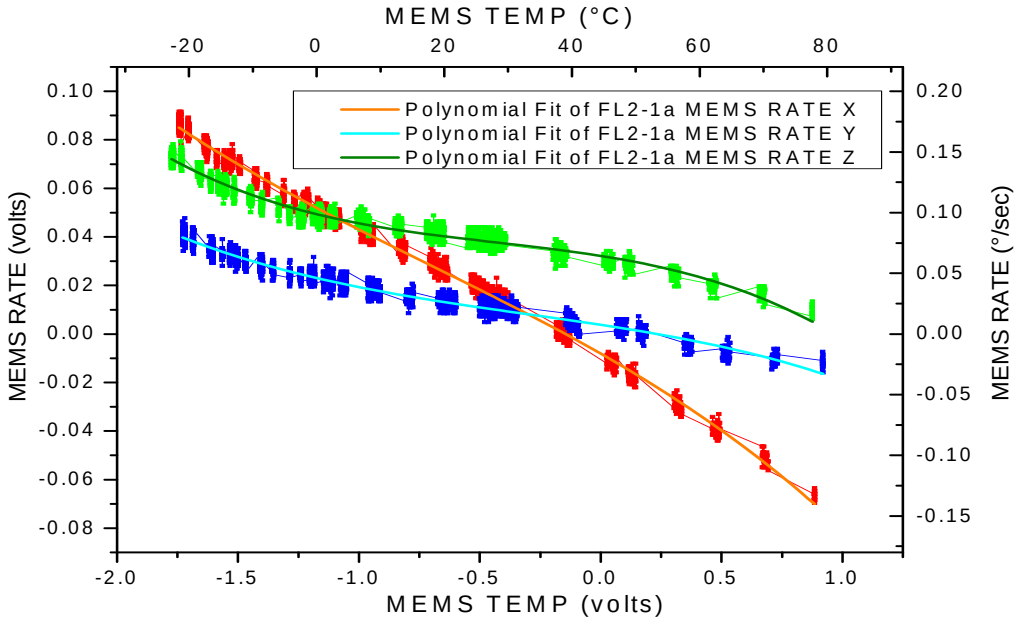

Figure 34. Vacuum thermal ramp data for spacecraft compensation polynomial generation

Table 7. Spacecraft Cubic Bias Compensation Values in Volts

Sensor Bias	Variable	Value (V)	Standard Error (V)	Residual Sum of Squares	Adj. R-Square
X	B	-0.00809	9.42371E-5	0.01733	0.99549
	m_1	-0.05675	1.39881E-4		
	m_2	-0.0107	2.48778E-4		
	m_3	-0.00503	1.2944E-4		
Y	B	0.0038	9.04443E-5	0.01661	0.9697
	m_1	-0.01519	1.30299E-4		
	m_2	-0.0037	2.28306E-4		
	m_3	-0.00402	1.23636E-4		
Z	B	0.03219	1.01867E-4	0.02021	0.96914
	m_1	-0.01581	1.53371E-4		
	m_2	-0.01039	2.70324E-4		
	m_3	-0.00796	1.36271E-4		

Table 8. Spacecraft Cubic Bias Compensation Values in °C vs. °/sec

Sensor Bias	Variable	Value (V)	Standard Error (V)	Residual Sum of Squares	Adj. R-Square
X	B	0.10358	1.15748E-4	0.08397	0.99542
	m_1	-0.00276	4.75537E-6		
	m_2	1.01728E-5	3.06867E-7		
	m_3	-1.91933E-7	4.50312E-9		
Y	B	0.04631	1.16592E-4	0.08545	0.97027
	m_1	-0.00125	4.82254E-6		
	m_2	1.5161E-5	3.11857E-7		
	m_3	-1.51168E-7	4.42731E-9		
Z	B	0.09842	1.22537E-4	0.09314	0.9719
	m_1	-0.00128	4.89401E-6		
	m_2	2.50795E-5	3.05081E-7		
	m_3	-2.99741E-7	4.62209E-9		

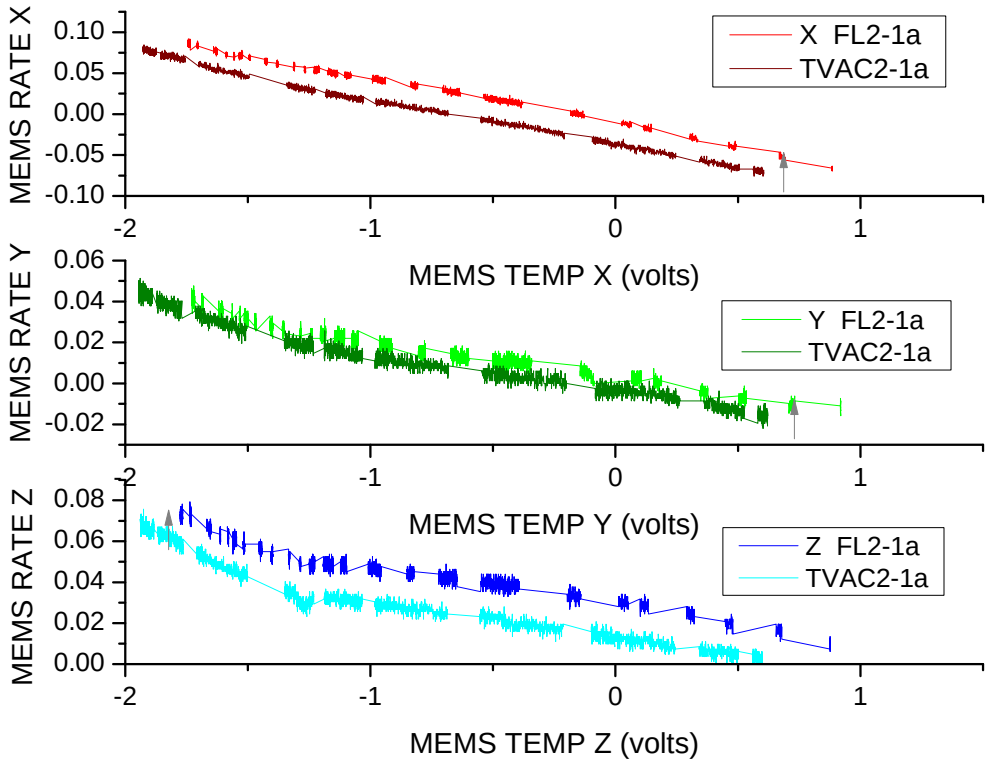

Figure 35. Comparison of Ground and Spacecraft Polynomials

c. Polynomial Testing and Bias drift

To test the compensation polynomials, the MEMS unit was again placed in the TVAC for a period of ~5 hours under vacuum at room temperature. This was a simple test to collect data and compare the results once the polynomials were applied. It was also an interest to observe how the rates drift in vacuum over a longer period. For comparison, a short 20-minute sample under ambient pressure was taken before (7.5E+2 Torr) and after (7.6E+2 Torr) the test. In accordance with the Vacuum degree test section results, the vacuum level during this test was kept under 1E-4 Torr to minimize bias offsets related to pressure changes; the chamber pressure was roughly at 4.6E-5 Torr at the start of the test to 1.2E-5 after the test and right before the pumps were turned off. Figure 36 is a combined plot of data before, during, and after the vacuum test, showing discontinuities in the plot where the vacuum pumps were on. In (a) the uncompensated rates are shown and the sensor outputs are seen to drift with internal temperature and small changes to the ambient temperature. In (b), the ground test polynomials were applied to the data. As expected, the curves outside of the vacuum region show reduced biases to nearly zero. Moreover, the temperature drift in the vacuum data is corrected but is still shifted due to the pressure difference. In (c), the spacecraft polynomials were applied to the data set and the data within the vacuum lines are brought down to nearly zero.

Initial transients, as seen in (b), last about 5 minutes in ambient and bias errors of up to 0.02°/sec, 0.014°/sec, and 0.03°/sec were observed for the X, Y, and Z sensors. Similarly, transients in vacuum were observed and lasted at least an hour, which is significantly longer than the ambient behavior. During this vacuum transition period, the X, Y, and Z sensor bias errors of ~0.02°/sec, ~0.015°/sec, and ~0.016°/sec were observed, which are comparable to the ambient values. From these initial results and the 5% requirement, one can estimate that the resolution limits in vacuum would be about 0.4°/sec, 0.3°/sec, and 0.3°/sec. The rate tests in the following section would be able to provide a slightly more accurate estimate since the earth rate components can be removed by positioning the HAAS table at the appropriate angles.

Once the initial transients were stable in vacuum, the averaged temperature and pressure compensated bias errors are: X = 0.004 °/sec, Y = -0.004 °/sec, and Z = -0.002 °/sec. These errors drift with time and will be discussed in the Allan variance section, G.3.

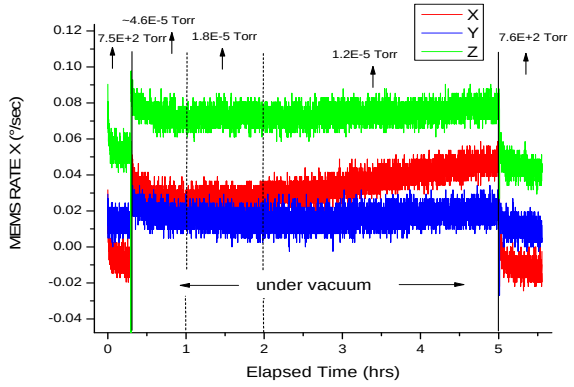

(a)

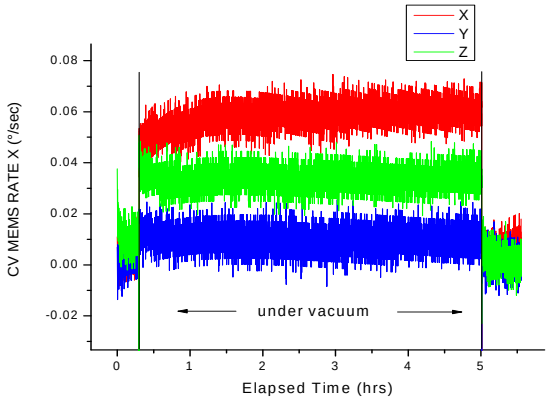

(b)

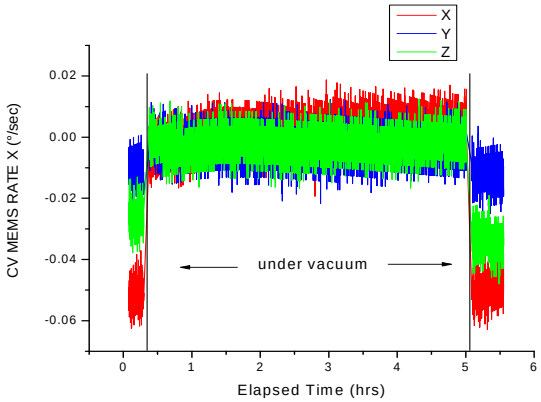

(c)

Figure 36. (a) Uncompensated Rates, (b) Temperature Compensated Rates, and (c) Temperature and Pressure Compensated Rates

E. RATE TRANSFER TESTING

Rate output verification testing was conducted to compare the angular rates measured by the gyroscope with that given by a rate table.[10] The goals of this test series are (1) to determine the gyroscope output error with rotation rate and compare the results to the static test estimates, and (2) to determine b_{cons}, and to extract the components of matrix M. These angular rate tests were performed while the test axis is orthogonal to the earth's rotational axis. In addition, the data were thermally compensated using the ground polynomials derived in Section C. Hence, the results are without (or reduced due to setup misalignment) the component of the Earth's rotation and temperature variation.

1. Setup

The HAAS rate table was positioned so that the main axis of the body is perpendicular to the earth's rotational axis. Then, the turntable was leveled and the MEMS and ACS were mounted on the plate using the bracket shown in the Figure 37. The MEMS subsystem was oriented so that the sense axis of the sensor under test was parallel with the HAAS rotational axis. To cancel the earth's rotational effects, the turntable was tilted at -36.4° (accounts for the geocentric latitude of Monterey, CA). The test setup is shown in Figures 37 and 38.

The HAAS controller was programmed to apply a constant angular rate for a set period of time and then stepped according to the designed test sequence. Two types of test schedules were used:

(a) For rates > 0.01°/s, the cycle step dwell time was set to 60 seconds and the table was rotated four times, alternating in the + and − rotational direction to prevent over twisting the wiring harness. A recording of the zero rate or bias before and after the test cycle was included to serve as a reference. This test sequence is shown in Figure 39.

[10] Typically, (as described in [15]) multi-position tests are conducted to evaluate the drift, as well as the run-to-run, and in-run drift of a gyroscope. A Graseby table is commonly used to accurately position the gyroscope in a series of fixed orientation with respect to geographic axes and the local gravity vector of the Earth. On the other hand, rate transfer tests are used to investigate the characteristics of the scale factor. Rate tables may be enclosed in a controlled environmental chamber for thermal evaluations. The methods are slightly different in this thesis due to the type of equipment available.

(b) For rates < 0.01°/s, the + and - rotation outputs became hard to distinguish from the zero rate bias. To ease the data analysis process, the + and − halves as well as the stationary output for rate tests < 0.01°/s were recorded separately. Moreover, the step duration was lengthened to 260 seconds.

To simulate the orbit scenario where the temperature compensation errors would be highest, the tests were conducted while the MEMS sensors were in its stabilization period. The rate tests (most) were started under 300 seconds after the ACS electronics was turned on.

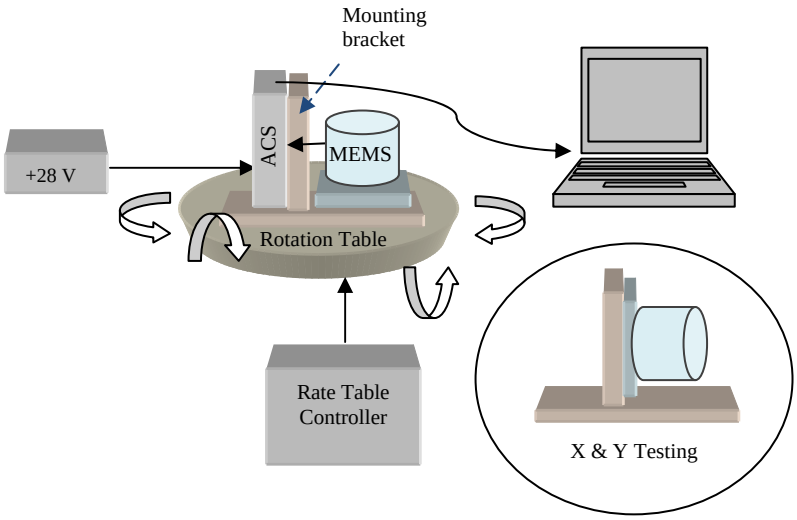

Figure 37. Rotary Table Test Setup

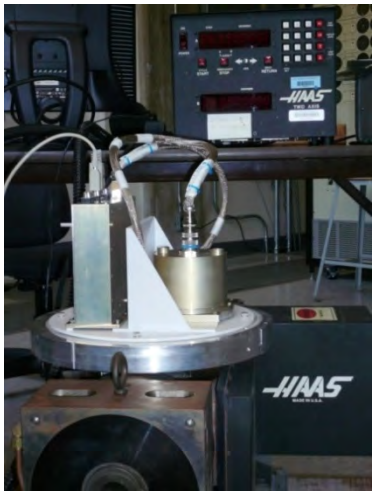

Figure 38. HAAS Test Setup

2. Results

A typical test output is shown by Figure 39.

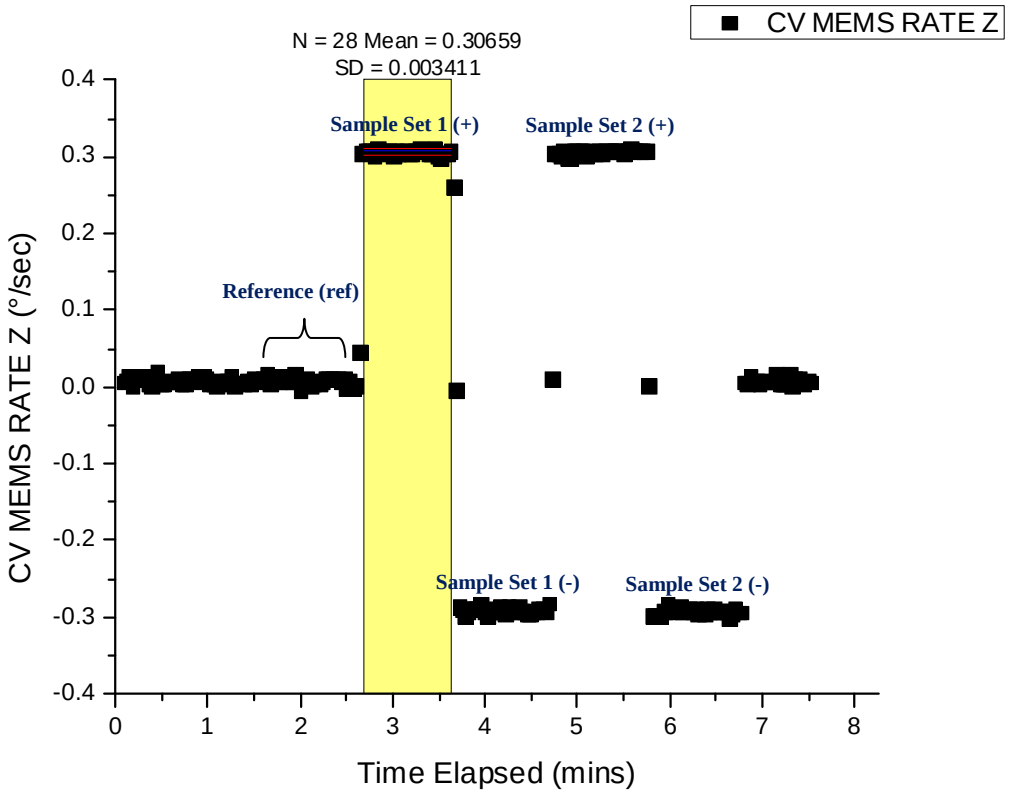

Figure 39. Example Output of Rate Testing (Z Sensor)

Due to potential rate table timing issues[11], the first and last data points of each step were not included in the analysis. Data from the rate transfer tests were analyzed by comparing the gyroscope output with the corresponding rate of the HAAS table. The deviations from the programmed table drive speed are listed in Tables 9, 10, and 11[12] in terms of the percent error of the average output. The error results are provided in two ways—using direct rate measurements (no ref) and using a reference (minus ref). The cells in orange are about the 5% error requirement and the cells in red are those that do

[11] HAAS Manual [36] pg 37 describes HAAS delay between steps. Timing issues also include delays from the manual start of HAAS controller, and manual start of python software.

[12] Tests were also conducted at earth rate but not presented in these tables, since the resolution degrades below the requirement much greater than the earth rate.

not meet this requirement. Note that the use of a reference was not in the original test plan and was a mere product of data analysis. Consequently, the averages for these references were taken from available data that were not uniform in sample size, unlike the actual dynamic measurements. Nevertheless, the reference data used in this analysis served as an initial estimate to gauge the potential of the sensors for use at lower rates.

The estimates show that if the rate sensor measurements are used directly, the performance requirements are met for most of the B-dot rates, which are >0.1 °/sec. If, however, a reference can be established or the bias estimated, then the resolution could improve to <0.1 °/sec, with the best or most reliable case showing at about 0.04 °/sec. By using this "reference," the output errors are provided with reduced[13] initial bias, including the effects of alignment errors from the setup (not internal misalignment) and the residual run-to-run bias variation. If rate integration is later pursued for this experiment, the reference that was used in this test would represent a known initial attitude and the sensors would be used to measure the rate of change in attitude from this initial attitude. The use of gyroscope for attitude control is usually calibrated against an external reference or a known initial attitude; periodic calibration must be performed due to bias drift [28], [29].

In these tests, we also wanted to address the initial transients, which is approximately 5 minutes in ambient and up to 1.5 hours in vacuum. Recall that in the ambient startup profile on a tabletop position, the observed bias errors after thermal compensation were as much as 0.024°/sec (X), 0.017°/sec (Y), and 0.019°/sec (Z) during the 300-second stabilization period. The initial resolution limit due to these biases using the 5% requirement would then be 0.48°/sec, 0.34°/sec, and 0.38°/sec for the X, Y, and Z sensors. Due to the more refined setup in the rate table test, slightly better resolution (>0.01°/sec) for all three sensors were obtained, as discussed above. In support of the static test results, the results in Tables 9, 10, and 11 are marked by an asterisk (*) where the rate tests started after the MEMS have been on for at least 300 seconds. As can be seen, these asterisk-marked tests do not appear to have a significant impact on the rate

[13]It is emphasized that the values in this analysis are *averages*, thus even with the use of reference, the bias cannot be completely removed.

resolution or the error trend. From these ambient test results, one can derive that the bias compensated sensors would perform as well in vacuum given that the startup profile tests showed similar resolution estimates of 0.4°/sec, 0.3°/sec, and 0.3°/sec during the observed 1.5 hr stabilization. Although the initial transients are longer in vacuum, it is reasonable to expect that we need not wait 1.5 hrs before the sensors can be used, and that *most* of the larger detumbling rates can be measured accurately while the rates are still in transient. Further testing would be required to validate this. In addition to the tables, the absolute errors are plotted in Figure 40 and the relative error results using references are plotted in Figure 41. Again, the absolute errors are estimates of what can be currently achieved by the ACS setup using "raw" sensor data and using the in-run bias as a minimum compensation method. On the other hand, the relative error results using the references (also compensated using the in-run bias) represent possible improvement with further work. It should be noted that the true resolution of the system would ultimately be defined by the sensor fusion algorithm.

Table 9. Z Sensor Output Error in Percent

Test Rate Z	Sample Set 1			Sample Set 2		
	% Error (minus ref)	% Error (no ref)	STDV in °/sec (no ref)	% Error (minus ref)	% Error (no ref)	STDV in °/sec (no ref)
5	1.3	1.1	0.001	1.3	1.0	0.001
-5	0.5	0.7	0.004	0.6	0.8	0.004
4	0.3	0.1	0.004	0.3	0.1	0.003
-4	0.3	0.5	0.005	0.3	0.5	0.005
4.5	0.2	0.2	0.005	0.2	0.2	0.004
-4.5	0.5	0.5	0.003	0.5	0.6	0.004
3	0.4	0.1	0.004	0.5	0.1	0.004
-3	0.4	0.7	0.005	0.4	0.7	0.004
3.5	0.4	0.1	0.003	0.4	0.2	0.004
-3.5	0.4	0.6	0.004	0.4	0.6	0.004
2	0.4	-0.1	0.004	0.4	0.0	0.004
-2	0.3	0.7	0.004	0.3	0.7	0.003
2.5	0.4	0.1	0.004	0.3	0.0	0.004
-2.5	0.5	0.8	0.004	0.4	0.7	0.004
1.5	0.5	-0.1	0.005	0.6	0.1	0.004
-1.5	0.4	1.0	0.004	0.4	0.9	0.004
1	0.5	-0.2	0.004	0.6	-0.1	0.004
-1	0.6	1.3	0.005	0.6	1.3	0.004
0.5	0.6	-1.0	0.005	0.5	-1.0	0.004
-0.5	0.6	2.1	0.004	0.5	2.1	0.004
0.4	0.6	-1.1	0.004	-0.2	-2.0	0.004
-0.4	0.4	2.1	0.004	0.7	2.4	0.004
0.45	0.3	-1.0	0.003	0.4	-0.9	0.004
-0.45	0.4	1.7	0.004	0.6	1.8	0.005
0.3	0.5	-2.2	0.003	0.6	-2.1	0.003
-0.3	0.2	2.9	0.004	-0.2	2.6	0.004
0.35	0.6	-1.6	0.004	1.0	-1.3	0.005
-0.35	0.6	2.8	0.005	0.4	2.7	0.004
0.2	1.3	-3.2	0.004	1.2	-3.3	0.004
-0.2	0.0	4.5	0.004	0.3	4.8	0.005
0.25	0.4	-2.8	0.005	1.5	-1.7	0.005
-0.25	-0.2	2.9	0.004	-0.2	2.9	0.004
0.1	3.2	-5.2	0.003	2.4	-6.0	0.004
-0.1	-0.1	8.3	0.005	-0.1	8.3	0.005
0.15	0.3	-3.9	0.004	1.2	-3.1	0.005
-0.15	1.5	5.7	0.004	1.6	5.8	0.003
0.09	0.6	-7.6	0.004	0.9	-7.3	0.004
-0.09	-3.1	5.0	0.004	0.7	8.9	0.004
0.08	-2.0	-8.7	0.004	-0.9	-7.7	0.003
-0.08	2.2	8.9	0.004	1.8	8.5	0.004
0.07	4.0	-14.4	0.004	4.7	-13.8	0.004
-0.07	-3.8	14.7	0.005	-5.9	12.5	0.004
0.06	0.2	-14.0	0.004	1.3	-12.9	0.004
-0.06	0.4	14.6	0.004	0.0	14.2	0.004
0.05	-3.2	-20.6	0.004	-0.4	-17.9	0.004
-0.05	0.9	18.4	0.004	-1.4	16.0	0.004
0.04	5.6	-19.6	0.004	6.5	-18.8	0.005

Test Rate Z	Sample Set 1			Sample Set 2		
	% Error (minus ref)	% Error (no ref)	STDV in °/sec (no ref)	% Error (minus ref)	% Error (no ref)	STDV in °/sec (no ref)
-0.04	-2.6	22.7	0.004	-6.3	19.0	0.005
0.03	-1.1	-19.6	0.003	-4.1	-22.6	0.004
-0.03	4.3	22.8	0.004	5.6	24.1	0.004
0.02	-5.4	-39.9	0.004	3.1	-31.4	0.004
-0.02	13.2	47.7	0.003	5.5	40.1	0.003
0.01	19.4	-48.7	0.004	2.8	-65.3	0.004
-0.01	-2.5	65.6	0.005	-1.5	66.6	0.005
0.009	16.4	-57.8	0.005	--	--	--
-0.009	-6.1	54.1	0.004	--	--	--
0.008*	-10.5	-78.9	0.004	--	--	--
-0.008*	6.1	69.7	0.004	--	--	--
0.007*	5.4	-81.5	0.004	--	--	--
-0.007*	5.7	93.8	0.004	--	--	--
0.006*	-5.7	-92.7	0.004	--	--	--
-0.006*	3.6	105.2	0.004	--	--	--

Table 10. X Sensor Output Error in Percent

Test Rate X	Sample Set 1			Sample Set 2		
	% Error (minus ref)	% Error (no ref)	STDV in °/sec (no ref)	% Error (minus ref)	% Error (no ref)	STDV in °/sec (no ref)
5*	0.4	0.2	0.005	0.3	0.1	0.005
-5*	0.3	0.5	0.002	0.3	0.5	0.001
4	-0.1	-0.3	0.006	0.0	-0.3	0.004
-4	-0.1	0.2	0.004	0.0	0.2	0.005
4.5	-0.2	-0.4	0.005	-0.2	-0.4	0.005
-4.5	-0.2	0.0	0.005	-0.2	0.0	0.005
3	0.1	-0.3	0.003	0.0	-0.3	0.005
-3	-0.2	0.2	0.004	-0.2	0.2	0.006
3.5	-0.1	-0.3	0.005	0.0	-0.3	0.005
-3.5	-0.1	0.2	0.005	-0.1	0.2	0.005
2	0.2	-0.4	0.006	3.6	3.0	0.348
-2	-0.3	0.3	0.004	-0.4	0.2	0.005
2.5	0.0	-0.4	0.004	-0.1	-0.5	0.004
-2.5	-0.1	0.2	0.004	-0.1	0.3	0.005
1.5	0.0	-0.5	0.003	0.0	-0.5	0.004
-1.5	-0.2	0.4	0.006	-0.1	0.5	0.004
1	0.1	-0.9	0.005	0.2	-0.7	0.004
-1	-0.3	0.7	0.004	-0.1	0.8	0.005
0.5	-0.3	-1.9	0.005	0.0	-1.6	0.003
-0.5	-0.1	1.5	0.004	0.1	1.7	0.005
0.4*	-0.7	-2.1	0.003	-0.7	-2.1	0.004
-0.4*	0.5	1.9	0.005	0.5	1.9	0.004
0.3	-0.4	-3.3	0.004	-0.2	-3.1	0.005
-0.3	0.1	3.0	0.004	-1.1	1.8	0.005

Test Rate X	Sample Set 1			Sample Set 2		
	% Error (minus ref)	% Error (no ref)	STDV in °/sec (no ref)	% Error (minus ref)	% Error (no ref)	STDV in °/sec (no ref)
0.2	-0.3	-4.8	0.004	0.0	-4.4	0.004
-0.2	-1.1	3.4	0.004	-0.1	4.4	0.005
0.1*	0.6	-7.8	0.004	0.2	-8.3	0.004
-0.1*	-0.2	8.3	0.004	-1.6	6.8	0.004
0.09	-0.8	-9.8	0.004	-1.5	-10.5	0.004
-0.09	0.0	9.1	0.004	-0.7	8.3	0.004
0.08	0.0	-9.0	0.004	1.4	-7.6	0.004
-0.08	-4.2	4.7	0.003	-1.6	7.3	0.003
0.07	0.6	-11.9	0.004	0.8	-11.7	0.004
-0.07	-2.2	10.3	0.005	-4.3	8.2	0.004
0.06*	-1.3	-13.9	0.003	0.0	-12.6	0.004
-0.06*	-0.9	11.7	0.005	-1.6	11.0	0.004
0.05*	2.1	-20.0	0.003	4.3	-17.8	0.004
-0.05*	-5.9	16.2	0.003	-8.0	14.1	0.003
0.04	0.1	-21.8	0.005	-0.7	-22.7	0.004
-0.04	-5.5	16.4	0.004	0.2	22.1	0.004
0.03*	6.0	-26.5	0.004	4.8	-27.8	0.005
-0.03*	-8.0	24.6	0.004	-12.0	20.6	0.003
0.02	9.2	-34.8	0.004	5.9	-38.0	0.003
-0.02	-10.2	33.7	0.004	-8.1	35.8	0.003
0.01	18.2	-66.7	0.004	13.6	-71.3	0.004
-0.01	-30.7	54.2	0.004	-25.2	59.7	0.003
0.009	30.9	-77.2	0.004	19.7	-88.5	0.004
-0.009	-34.5	73.6	0.004	-29.2	78.9	0.004
0.008	22.0	-106.8	0.003	--	--	0.005
-0.008	-21.1	88.3	0.004	--	--	0.001
0.007	--	-92.7	0.004	--	--	0.004
-0.007	--	98.2	0.004	--	--	0.005
0.006	33.2	-120.0	0.004	--	--	0.005
-0.006	-3.0	130.1	0.004	--	--	0.005

Table 11. Y Sensor Output Error in Percent

Test Rate Y	Sample Set 1			Sample Set 2		
	% Error (minus ref)	% Error (no ref)	STDV in °/sec (no ref)	% Error (minus ref)	% Error (no ref)	STDV in °/sec (no ref)
5	0.1	0.2	0.001	0.1	0.2	0.001
-5	-0.1	-0.2	0.001	-0.1	-0.2	0.001
4	-0.5	-0.4	0.004	-0.5	-0.4	0.004
-4	-0.6	-0.7	0.003	-0.6	-0.8	0.005
4.5	-0.5	-0.4	0.005	-0.5	-0.4	0.005
-4.5	-0.6	-0.7	0.005	-0.6	-0.7	0.005
3	-0.6	-0.3	0.004	-0.5	-0.3	0.004
-3	-0.5	-0.7	0.004	-0.6	-0.8	0.004
3.5	-0.5	-0.3	0.004	-0.6	-0.4	0.004

Test Rate Y	Sample Set 1			Sample Set 2		
	% Error (minus ref)	% Error (no ref)	STDV in °/sec (no ref)	% Error (minus ref)	% Error (no ref)	STDV in °/sec (no ref)
-3.5	-0.6	-0.8	0.006	-0.5	-0.7	0.005
2	-0.4	-0.1	0.005	-0.4	-0.1	0.005
-2	-0.6	-0.9	0.006	-0.7	-1.0	0.003
2.5	-0.4	-0.2	0.005	-0.5	-0.3	0.004
-2.5	-0.6	-0.8	0.004	-0.6	-0.8	0.005
1.5	-0.3	0.1	0.004	-0.3	0.1	0.003
-1.5	-0.6	-1.0	0.004	-0.7	-1.1	0.004
1	-0.2	0.4	0.004	-0.2	0.4	0.005
-1	-0.7	-1.3	0.004	-0.6	-1.2	0.005
0.5	-0.4	0.9	0.004	-0.1	1.2	0.005
-0.5	-0.9	-2.2	0.004	-0.8	-2.1	0.004
0.4	0.5	1.7	0.004	0.2	1.3	0.003
-0.4	-0.9	-2.0	0.004	-1.3	-2.5	0.004
0.3	0.5	2.5	0.004	-0.1	1.9	0.004
-0.3	-0.6	-2.6	0.004	-1.2	-3.2	0.005
0.2	1.3	4.3	0.004	0.9	3.9	0.004
-0.2	-1.0	-4.0	0.006	-1.2	-4.3	0.004
0.1	1.4	8.0	0.005	1.0	7.6	0.004
-0.1	-2.8	-9.4	0.005	-2.8	-9.4	0.005
0.09	1.9	8.7	0.005	3.9	10.7	0.004
-0.09	-1.3	-8.2	0.004	-3.7	-10.6	0.003
0.08	2.1	9.6	0.004	2.1	9.6	0.003
-0.08	-1.6	-9.1	0.004	-5.1	-12.6	0.005
0.07	8.6	13.6	0.004	6.1	11.1	0.004
-0.07	-5.4	-10.4	0.004	-6.4	-11.4	0.004
0.06	0.6	11.2	0.005	2.2	12.8	0.005
-0.06	-3.8	-14.4	0.004	-2.0	-12.6	0.004

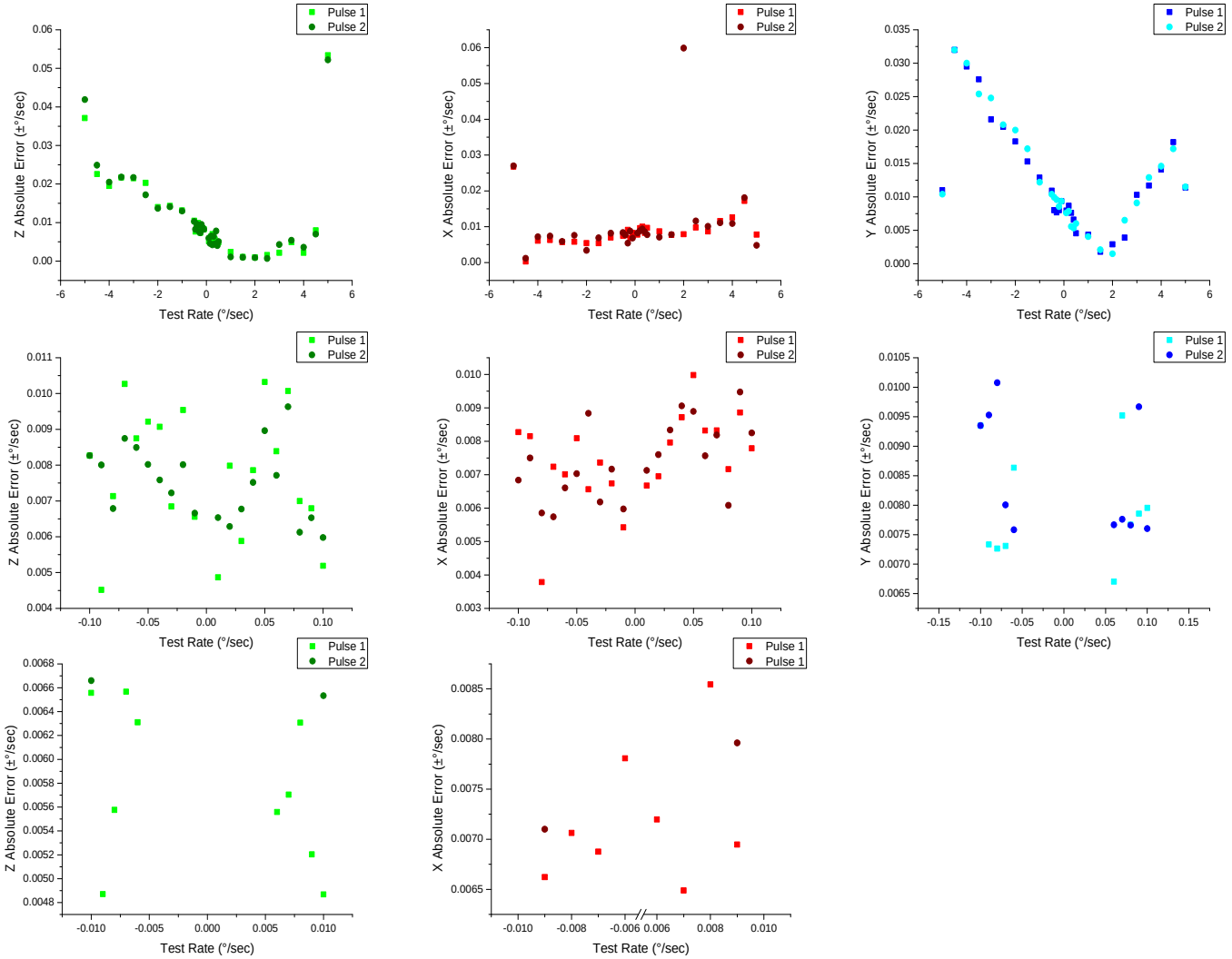

Figure 40. Absolute Errors (no reference)

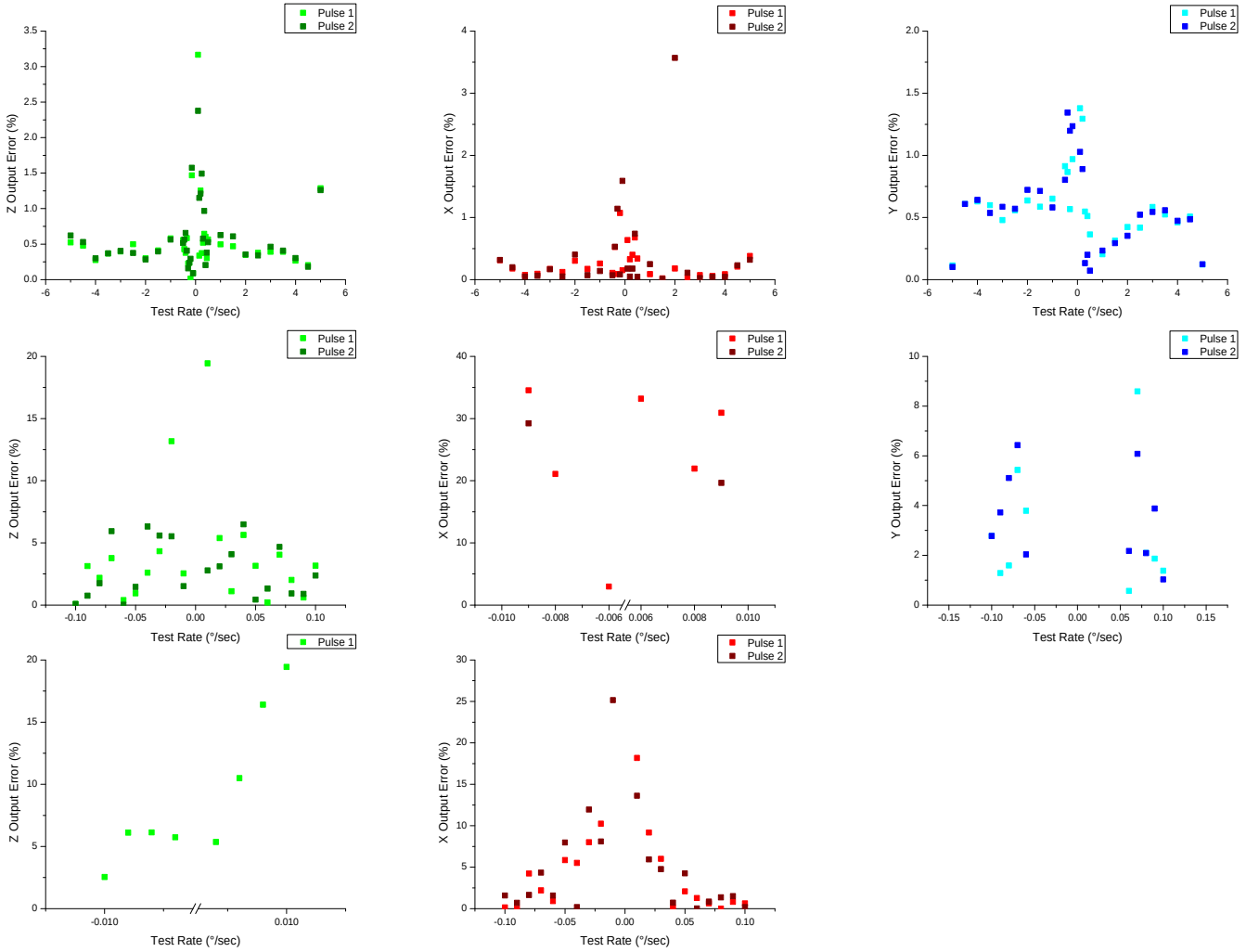

Figure 41. Sensor Relative Output Error in Percent (with reference)

a. B_{cons}, Scale Factor and Nonorthogonality

The input-output data was plotted and the sample sets were fitted using a line. The input-output relationship is given by [15]:

$$output = bias + \widetilde{S_f} * input \tag{17}$$

where the actual scale factor $\widetilde{S_f}$ is the slope of fitted line while the y-intercept is the estimate of the fixed portion of the bias or b_{cons}. This is also shown in Figure 42.

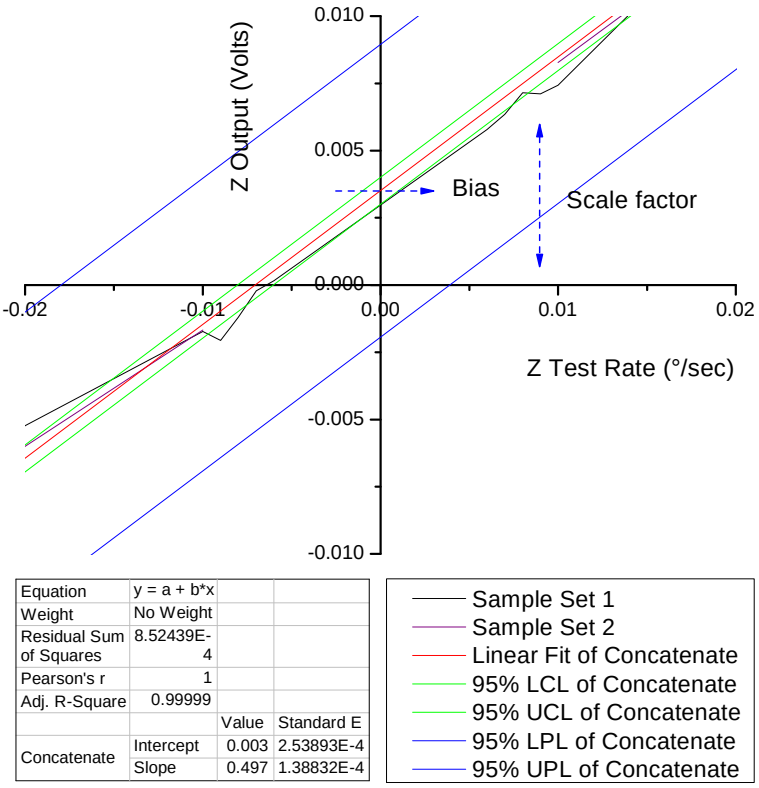

Figure 42. Bias and Scale Factor from the Input-Output Plot (Z)

The misalignment/nonorthogonality is shown by Figure 43. As seen in this example, small signals are detected along the orthogonal X and Y sensors during a Z axis test. Due to the position of the X and Y sensors in this particular test, these

misalignment errors include a component of the earth's rotation; although the misalignment errors are clearly more significant than the earth rate component. The output errors are summarized next in Figure 44.

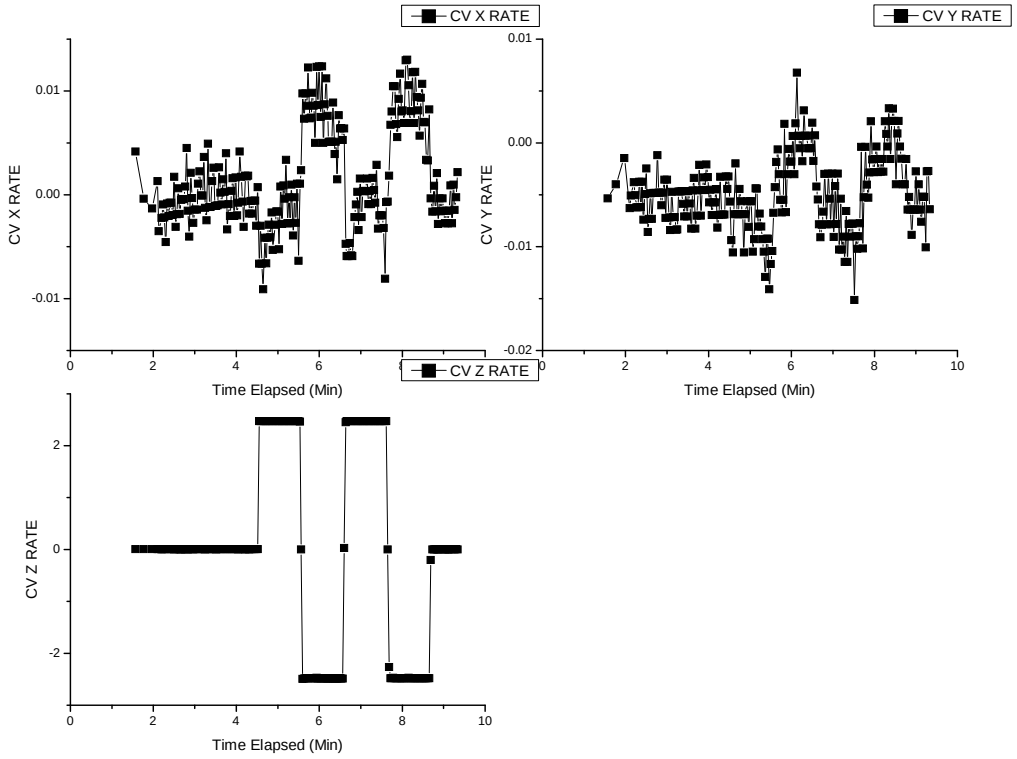

Figure 43. Example of misalignment errors for the X & Y sensors during a Z axis test.

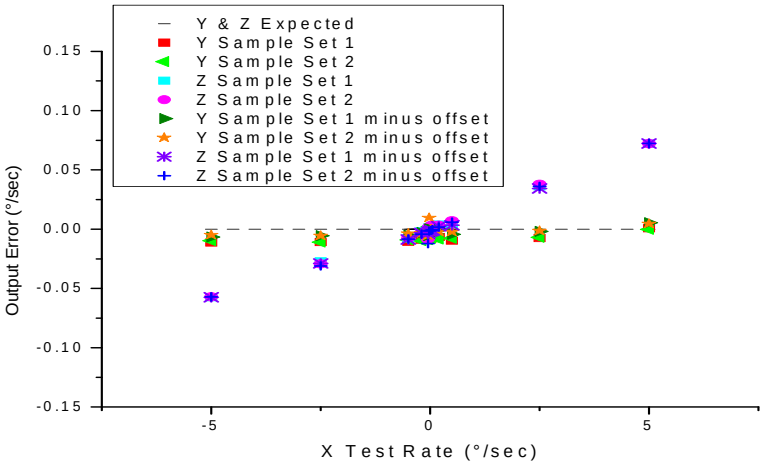

(a)

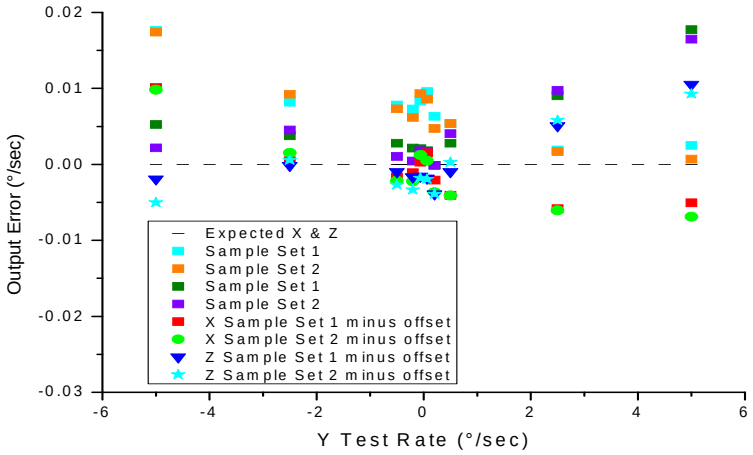

(b)

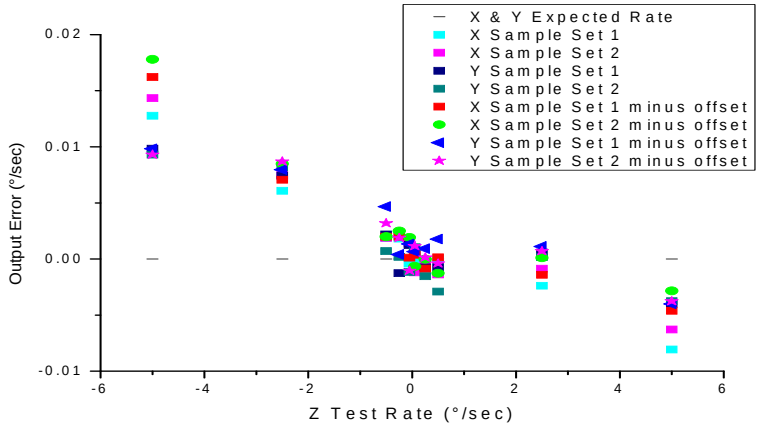

(c)

Figure 44. X, Y and Z Misalignment Errors

The results for:

$\boldsymbol{b_{cons}} = (b_{cons,x} \quad b_{cons,y} \quad b_{cons,z})$ and $\boldsymbol{M} = \begin{pmatrix} S_x & m_{xy} & m_{xz} \\ m_{yx} & S_y & m_{yz} \\ m_{zx} & m_{zy} & S_z \end{pmatrix}$ are given below for direct measurements (no ref) and for data with reference (minus ref). The Origin reports can be found in Appendices E–J. The results below have been converted to °/sec for b_{cons} and % for M.

- $\boldsymbol{b_{no\ ref}} = (7.18E-03 \quad -8.12E-03 \quad 7.00E-03)$
- $\boldsymbol{M_{no\ ref}} = \begin{pmatrix} 0.042 & 0.102 & 1.298 \\ -0.156 & -0.4 & 0.128 \\ -0.2 & -0.139 & 0.506 \end{pmatrix}$
- $\boldsymbol{b_{minus\ ref}} = (-1.74E-03 \quad -2.34E-03 \quad -6.52E-04)$
- $\boldsymbol{M_{minus\ ref}} = \begin{pmatrix} 0.042 & 0.102 & 1.298 \\ -0.23 & -0.4 & 0.128 \\ 0.244 & -0.139 & 0.506 \end{pmatrix}$

The "no ref" set of elements are suitable for the B-dot mode. On the other hand, the "minus ref" elements are provided here for the potential rate integration mode. The $\boldsymbol{b_{minus\ refs}}$ are the residual biases after using the references.

F. RANDOM VIBRATION TESTING

Vibration tests were performed in each of the three orthogonal axes to screen for design and workmanship defects. Figure 45 shows the test flow.

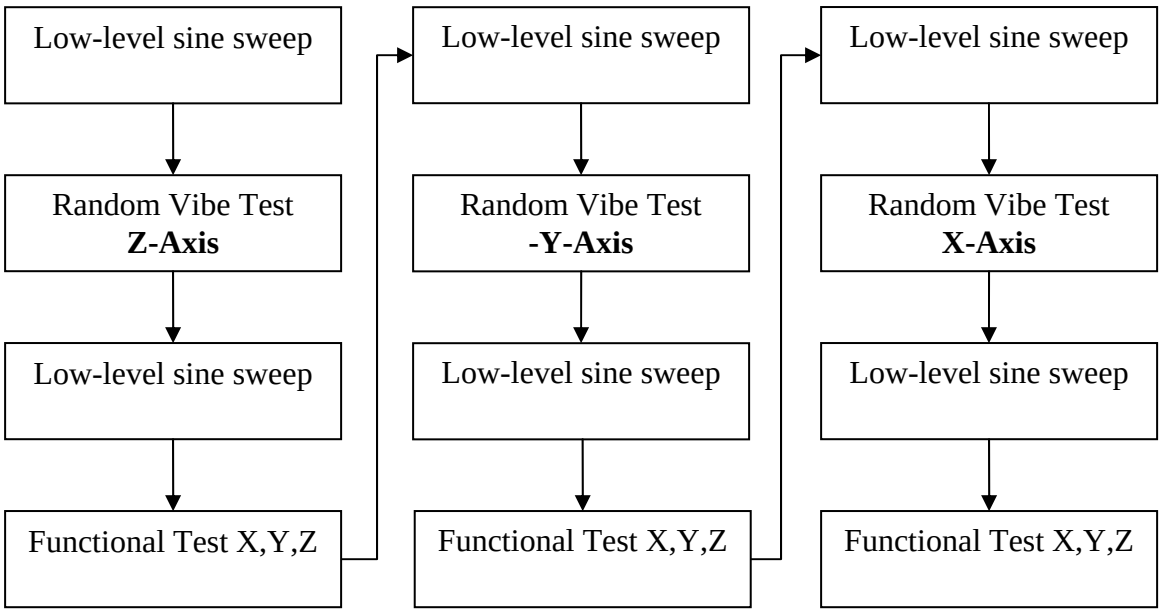

Figure 45. MEMS Random Vibration Test Flow

A low-level sine sweep test is performed prior to and after each test to measure the natural frequencies of the component in its test configuration and to verify the fixture dynamics. The test input is limited to the band from 20 to 1000 Hz, at 0.25 g and a sweep rate of 4 oct/min [9]. The sine sweep measurement is recorded and plotted in acceleration (g) vs. frequency (Hz).

The random vibration test is performed according to the test levels for component minimum workmanship as shown in Table 1. A plot showing these test levels are also shown in Figure 46. These levels are applicable for components 45.4 kg or less. The MEMS sensor suite weighs 874 g.

Functional tests on all three orthogonal axes of the MEMS are performed before acceptance testing and following each vibration test sequence to verify that the hardware is still fully operational. Functional tests are done using the same procedure as Section E,

Rate Transfer Test. An analysis is done to determine if there are any changes to the performance of the subsystem after random vibration testing.

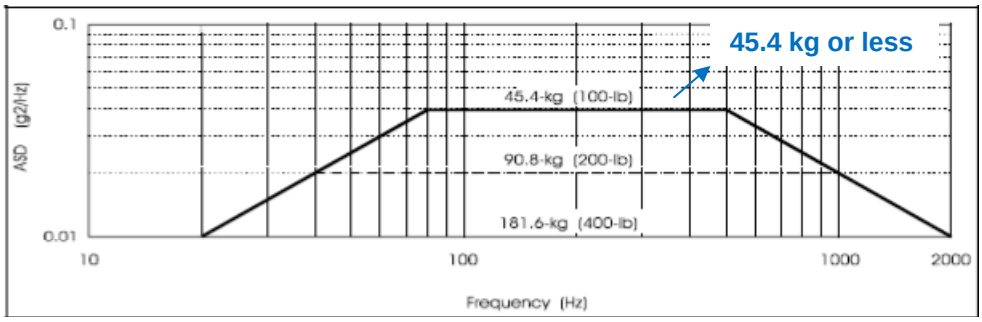

Figure 46. Component Minimum Workmanship Random Vibration Test Levels

1. Setup

In preparation for the vibration test, all screws in MEMS assembly were torqued according to estimated installation torque calculations. A pre-vibe functional test was conducted using the HAAS rate table using the same setup and procedures in Section E. Data was collected at 5°/sec, 0.5 °/sec, and 0.05°/sec on all three axes. The MEMS unit was then moved to the shaker table area.

The vibration test setup consists of a Ling 612VH electrodynamic shaker and amplifier, a computer workstation, which controls the shaker using the M+P Vibrunner software suite, a data acquisition system, a slip table, a power conditioner, a mounting fixture specifically designed for the MEMS, and four accelerometers. A closed-loop vibration control was implemented to ensure the acceleration input to the test article met the acceleration spectral density test specification. Before mounting the MEMS on the shaker table, an initial test using just the mounting fixture and two accelerometers was performed to verify the controller settings and to check the signals from the accelerometers. After the pretest, the MEMS unit was bolted on to the mounting fixture. One accelerometer was attached to the base plate and another on top of the enclosure cap. A video camera was also positioned to record the test. The setup and accelerometer placement are shown in Figure 47.

Vertical tests were first conducted for the Z sensor. Then, the shaker was rotated and attached to a horizontal slip table for the horizontal tests of the Y and X directions.

After each vibe test, the setup was inspected to verify that the accelerometers were still adhered well in place and that all screws were still tight. In addition, post-vibe functional tests were conducted on all three axes, as mentioned before.

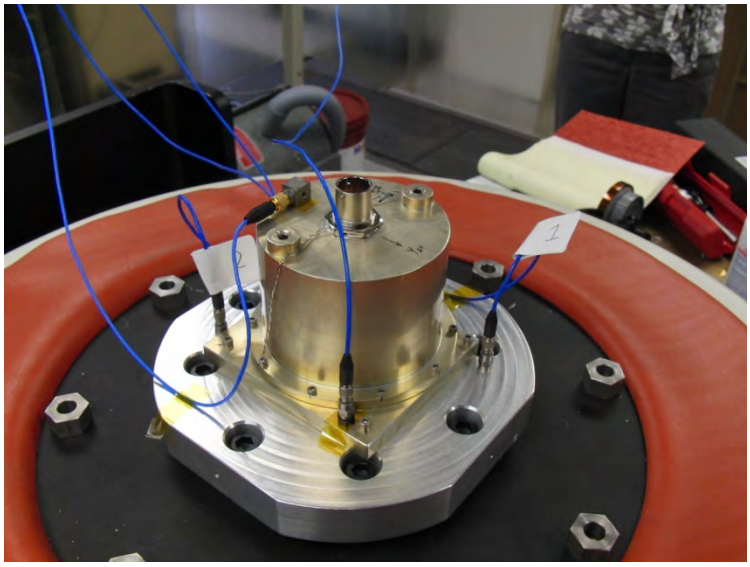

Figure 47. Random Vibe Test Setup

2. Results

a. Accelerometer Measurements

For the Z-axis test, the sine sweep shows the first mode at ~6.75 kHz likely due to the housing given the location of the accelerometer. The resonance at this frequency is apparent in the random vibration, as well. The Z results are shown in Figures 48 and 49.

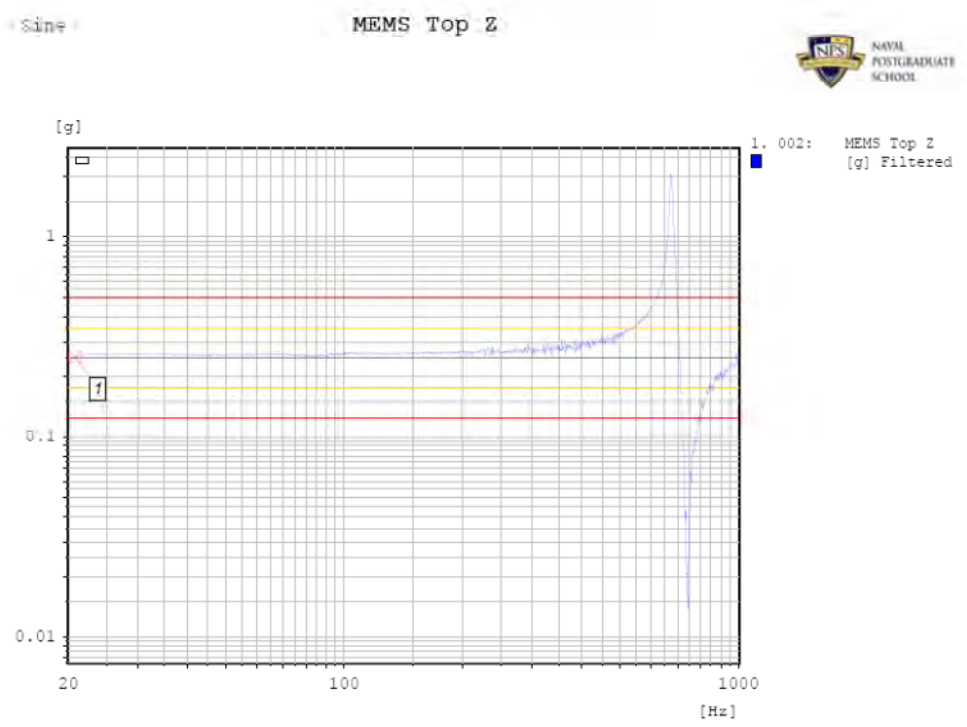

Figure 48. Sine Sweep (Pre Random Vibe) along the Z-Axis

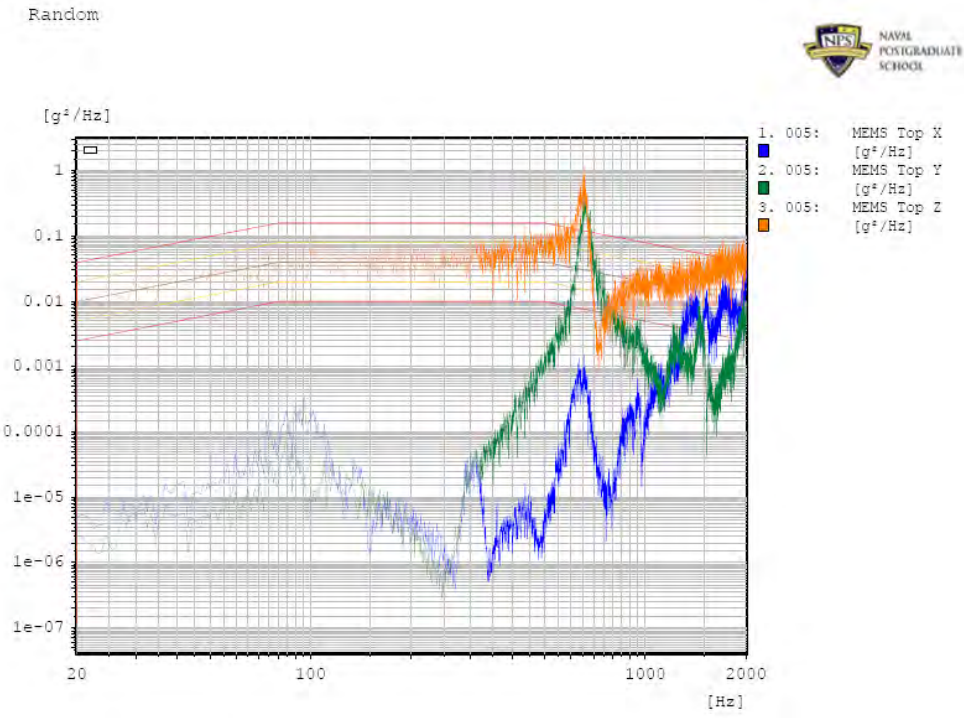

Figure 49. Random Vibration along the Z-Axis

The Y-axis test showed several peaks in the sine sweep test, with the highest seen at just under 700 Hz. However, there was no large spike observed at this frequency during the random vibration test. Instead, the Y acceleration shifted up at 1.2 kHz until 2 kHz. The post sweep displayed the same behavior as the pre-random vibe sine sweep. The Y results are shown in Figures 50, 51, and 52.

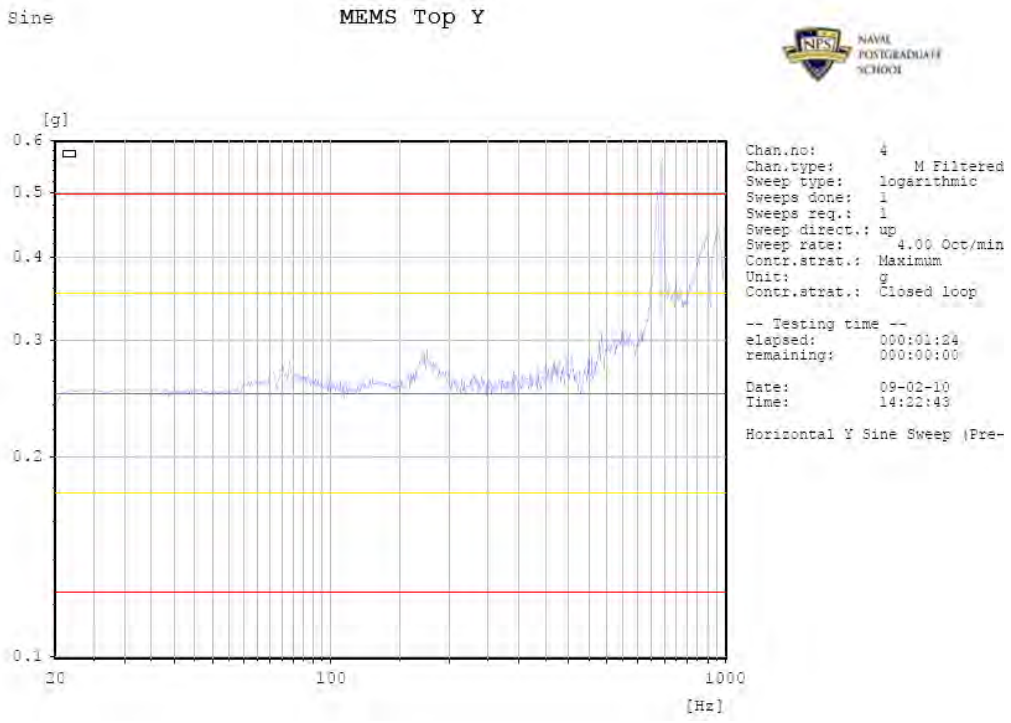

Figure 50. Low-level Sine Sweep (Pre-Random vibe) along the Y-Axis

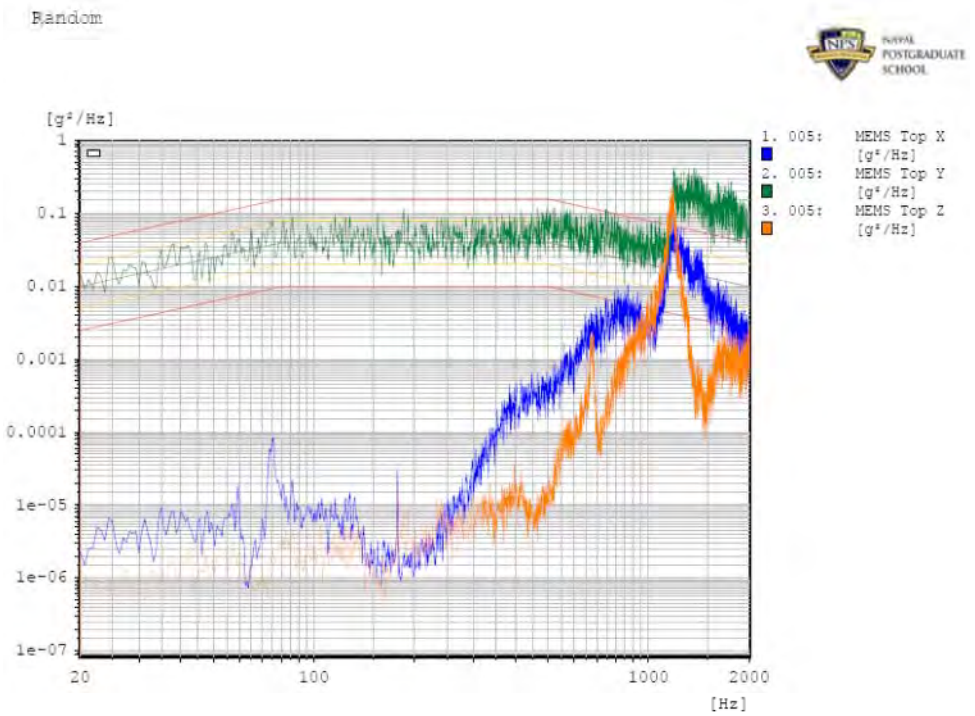

Figure 51. Random Vibration along the Y-Axis

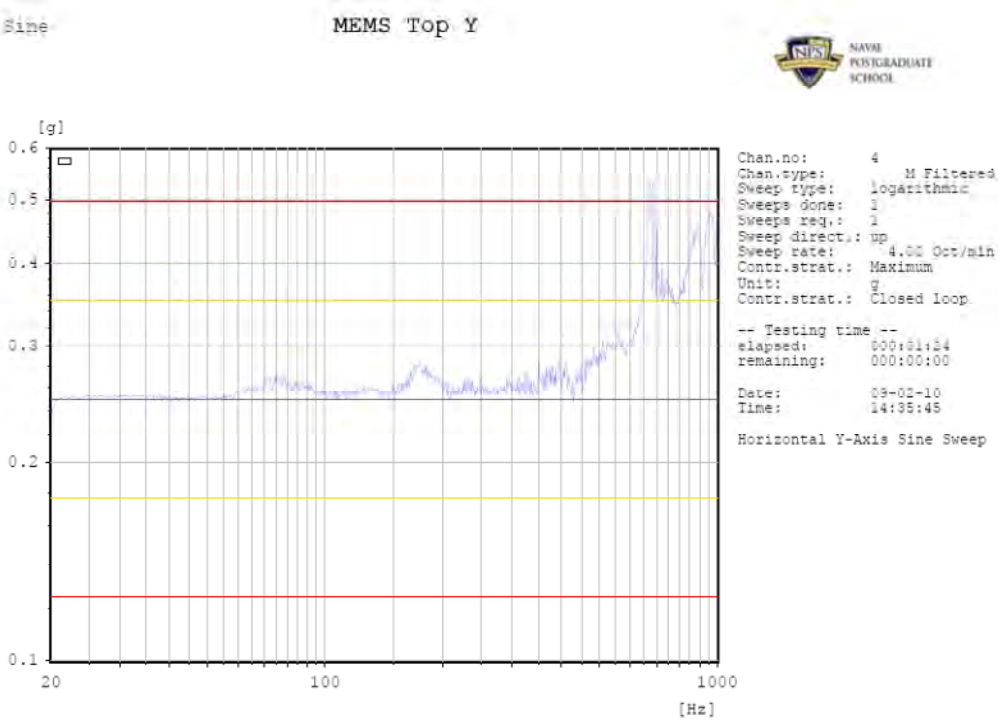

Figure 52. Low-level Sine Sweep (Post Random Vibe) along the Y-Axis

Finally, the results of the X-axis test are shown on Figures 53, 54, and 55. The sine sweep of X behaved similarly to the Y sine sweep, with the first peak showing at around 80 Hz. During the random vibration test, the highest acceleration was seen at ~1.3 kHz. A few more peaks showed after the largest spike and then the acceleration went back down to the input levels by 2 kHz. The post-random vibe sine sweep exhibited the same modes as the pre-random vibe sweep, indicating that there were no changes to the unit after the random vibe test.

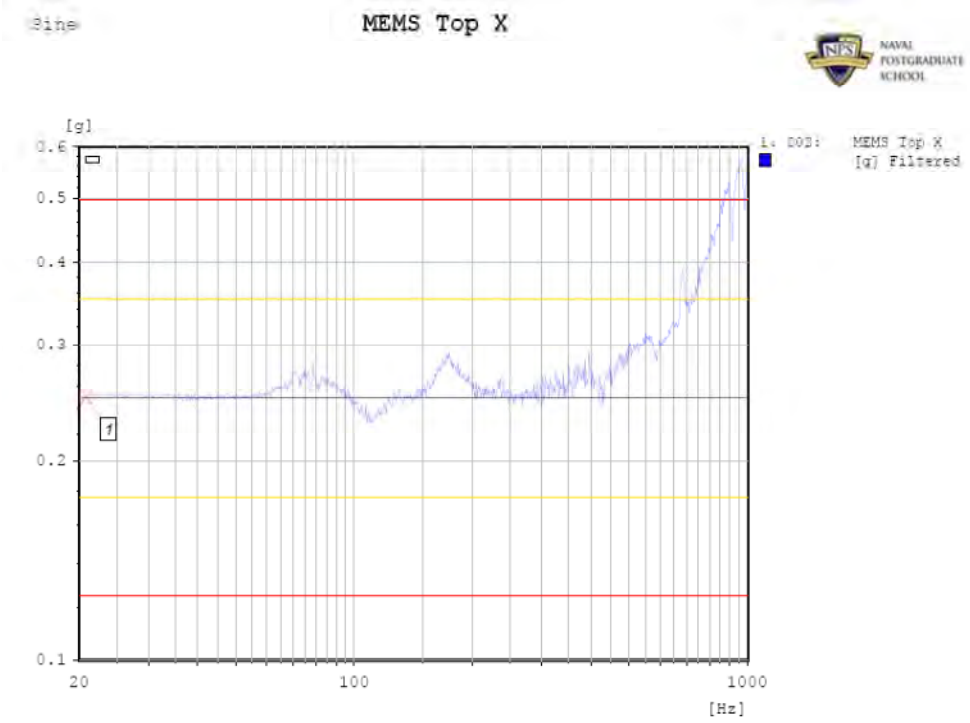

Figure 53. Low-Level Sine Sweep (Pre Random Vibe) along the X-Axis

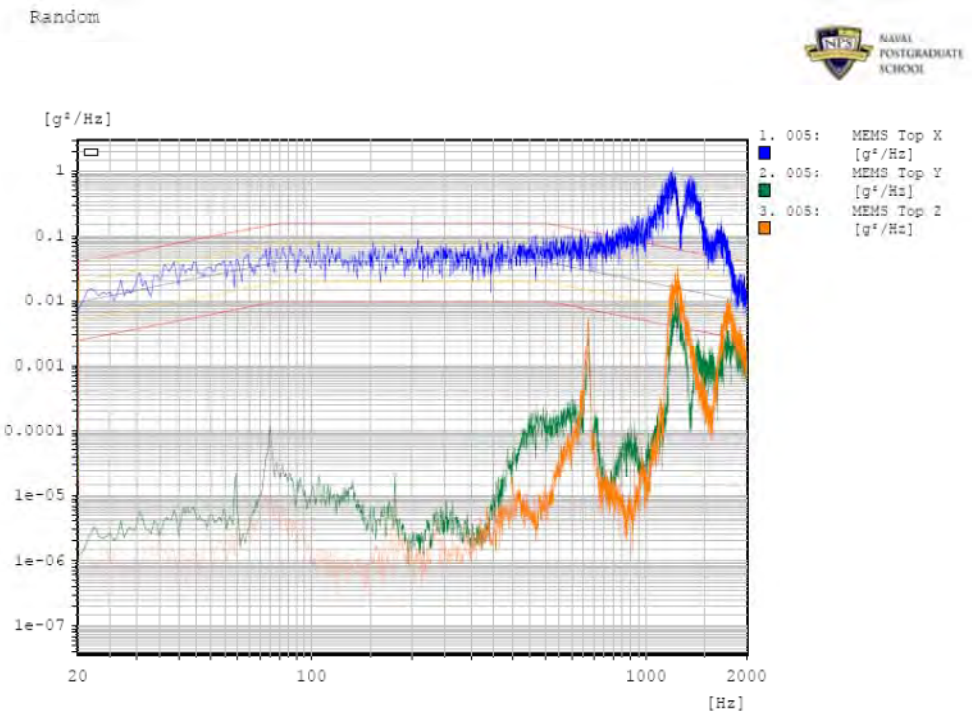

Figure 54. Random Vibration along the X-Axis

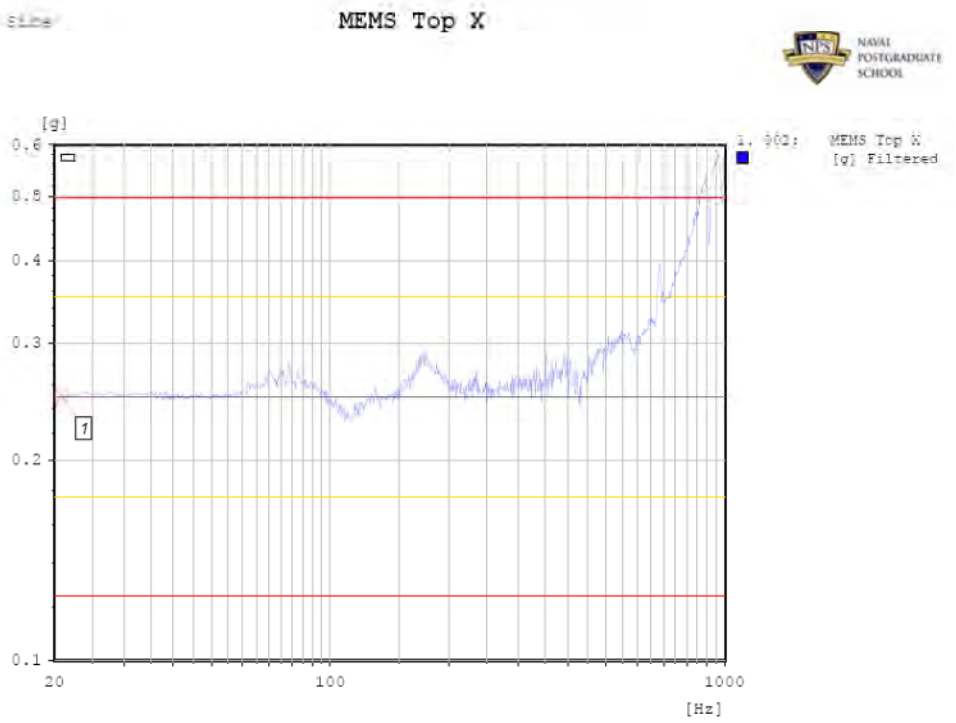

Figure 55. Low-Level Sine Sweep (Post Random Vibe) along the X-Axis

Overall, the higher frequency accelerations can be attributed to the dynamics of the MEMS unit. High frequency dynamics may also be contributions from the test fixture [30].

b. Visual Inspection

During the Z-axis test, two screws came loose on the MEMS housing. It was determined that the initially prescribed torque values were low and that a possible error in applying the torque values resulted from confusion of different screw sizes. The installation torque is calculated based on the target pre-load, which is generally set to at least 80% of the yield for the screw material. All torque values are being re-evaluated for higher preloads and will likely be increased to levels close to the 80% of yield point for the screw material [31]. At the time of the tests, there was no secondary backout prevention used for mounting the MEMS assembly to the shaker adapter plate. Safety wires were used for the connectors. There were no other failed parts found by visual inspection

c. Functional Test Results

The results of all functional tests performed on the MEMS subsystem are plotted in Figures 56, 57, and 58. The rate tests performed ~3 months earlier are also included in the graphs for comparison. Note that these results use the initial bias as reference to distinguish from the no motion signal; also, these are post-thermal compensation data. The “minus ref” values were used for this particular analysis to determine the variability using this referencing scheme, in addition to determining the vibration sensitivity of the sensors. The plots show that there are no significant changes to the rate output of all three sensors that could be attributed to the vibrations that they were subjected to during the shake test. At 5°/sec and 0.5°/sec, all three sensors met the performance requirements and are all within ±5% output error. At 0.05°/sec, the X and Y both exceeded the requirement 3 times out of the 5 tests. However, this inconsistency is not unexpected at this low rate. On the other hand, the Z sensor met the performance requirements in all of the tests.

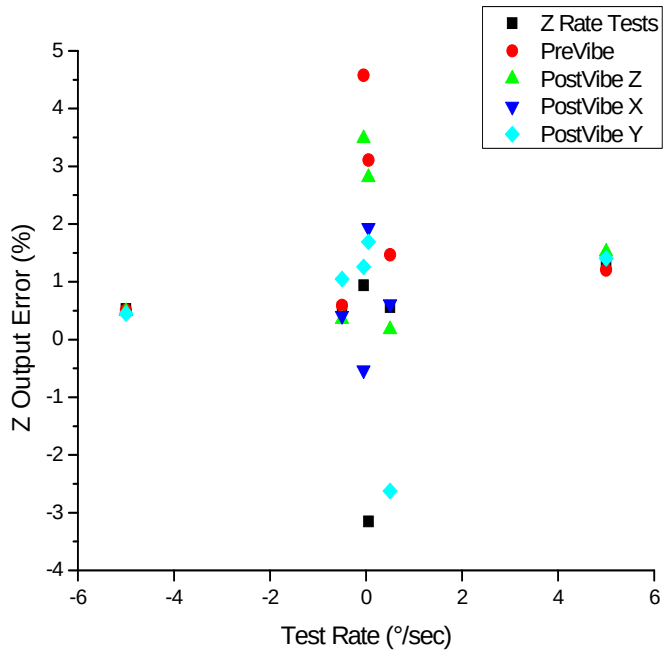

Figure 56. Functional Tests of Z Sensor

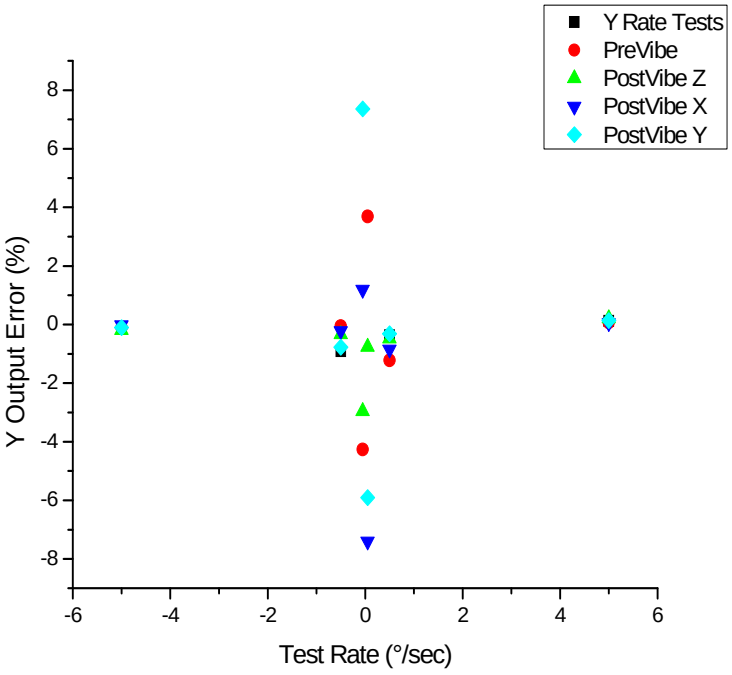

Figure 57. Functional Tests of Y Sensor

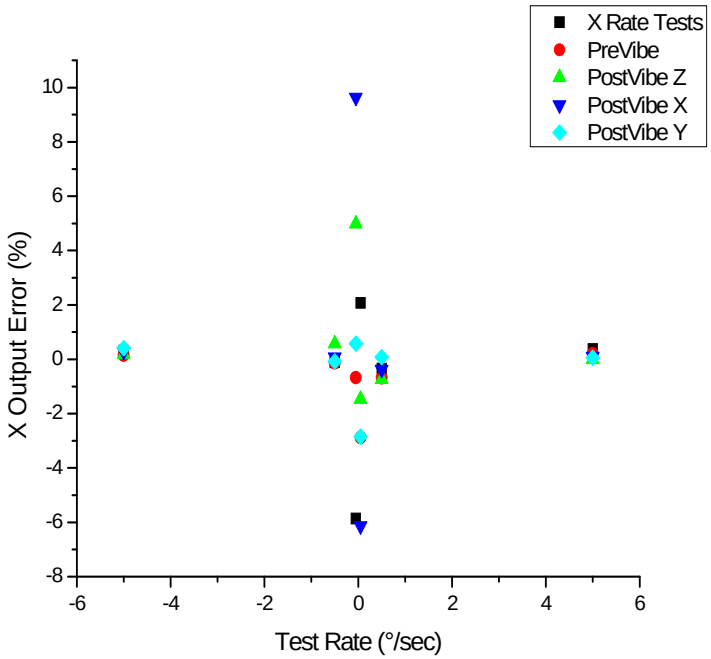

Figure 58. Functional Tests of X Sensor

The actual scale factor $\widetilde{S}_f$ and the fixed bias b_{cons} (no reference) are shown in Table 12 for all of the tests. Since the functional tests for the vibration tests were cycled only once, the sample sets for the rate tests were separated[14] for the purpose of comparison. The elements were extracted from the direct measurement data to obtain the worst-case values.

[14] Sample sets 1 and 2 of rate test results were concatenated.

Table 12. Comparison of $\widetilde{S_f}$ and b_{cons}

Test		X				Y				Z			
Category	**Sample**	**S_f mV/(°/sec)**	**S_f STDV mV/(°/sec)**	**Bias °/sec**	**Bias STDV °/sec**	**S_f mV/(°/sec)**	**S_f STDV mV/(°/sec)**	**Bias °/sec**	**Bias STDV °/sec**	**S_f mV/(°/sec)**	**S_f STDV mV/(°/sec)**	**Bias °/sec**	**Bias STDV °/sec**
Rate Test	Set 1	499.95	1.48E-01	0.008	2.80E-4	501.99	2.10E-01	-0.008	4.87E-4	497.52	1.95E-01	0.007	3.49E-4
	Set 2	499.62	3.83E-01	0.007	7.68E-4	502.01	2.14E-01	-0.008	4.96E-4	497.43	2.01E-01	0.007	3.82E-4
	Set 1 (6 points only)[15]	498.29	1.56E-01	0.009	4.54E-4	500.01	2.83E-01	-0.009	1.00E-3	495.49	6.96E-01	0.003	2.02E-3
Vibe Test	Pre Vibe	499.14	1.55E-01	0.012	4.49E-4	500.11	3.54E-01	-0.009	1.03E-3	495.9	6.40E-01	-0.002	1.86E-3
	Post Vibe Z	499.57	1.50E-01	0.012	4.36E-4	499.97	4.77E-01	-0.002	1.38E-3	494.97	9.96E-01	0.013	2.89E-3
	Post Vibe X	499.07	1.20E-01	0.012	3.47E-4	499.96	2.52E-01	0.000	7.32E-4	497.33	3.85E-01	0.019	1.37E-4
	Post Vibe Y	498.57	3.72E-01	0.013	1.08E-3	499.94	3.28E-01	-0.001	9.51E-4	495.33	9.18E-01	0.011	2.66E-3
Manuf. Test Data	n/a	500.152		0.048		502.14		0.068		497.92		0.131	
Manuf. Spec		500±5		±0.40		500±5		±0.40		500±5		±0.40	

[15] Included here to show effects of data reduction.

G. ADDITIONAL TESTS AND CHARACTERIZATION

1. ACS Data Save Interval

During data analysis, an error in the data save interval n (described in Section III-D-2) was observed. For most of the tests, a save interval of 2 was used. However, it was noticed that the interval could from time to time skip. For example, using the ACSID 238 data collected during recirculator and cold plate tests where a save interval of 2 was used, an interval in the elapsed time of 3 occurred 17 instances, 5 occurred 7 instances, and 6 in 2 instances. In another data set, ACSID 247, a save interval of 3 occurred 3 times. In ACSID 206, an interval of 3 occurred 150 times. This may not be too much of an issue for test analysis, since the data points are averaged. However, this affects actual space operations, since the current ACS setup requires MEMS data every two seconds. This observation is noted here for NPS SSAG use.

2. Variability within Tests

Recall that the sampling period of the current ACS setup is 200 points/sec. In the tests conducted above, one data point represents the mean of this 200 points/sec. Later into the tests, the software was updated so that the variance of the 200 points was also saved into the database. Short tests, as shown in Figure 59, were conducted to compare the variance within a test and between tests. The results show that the variance is greater within a test, shown in Figures 60 and 61, than between the ten short duration tests, shown in Figure 62.

In [2], sampling re-testing was recommended to possibly lower the sampling rate of 200 Hz and free up bandwidth and resources for other ACS tasks. As in [32] and [33], the sampling rate needs to be at least twice the bandwidth of the QRS11, which is ~100 Hz [12] to satisfy the Nyquist criterion. In [32], a sampling rate of three to five times the bandwidth was considered the reliable frequency. Thus, the 200 Hz is the minimum sampling frequency. It is not suggested to lower the sampling rate due to the Nyquist criterion and to the large variance within a test. The ACS computing has been alleviated by transferring some of the processes to the CD&H.

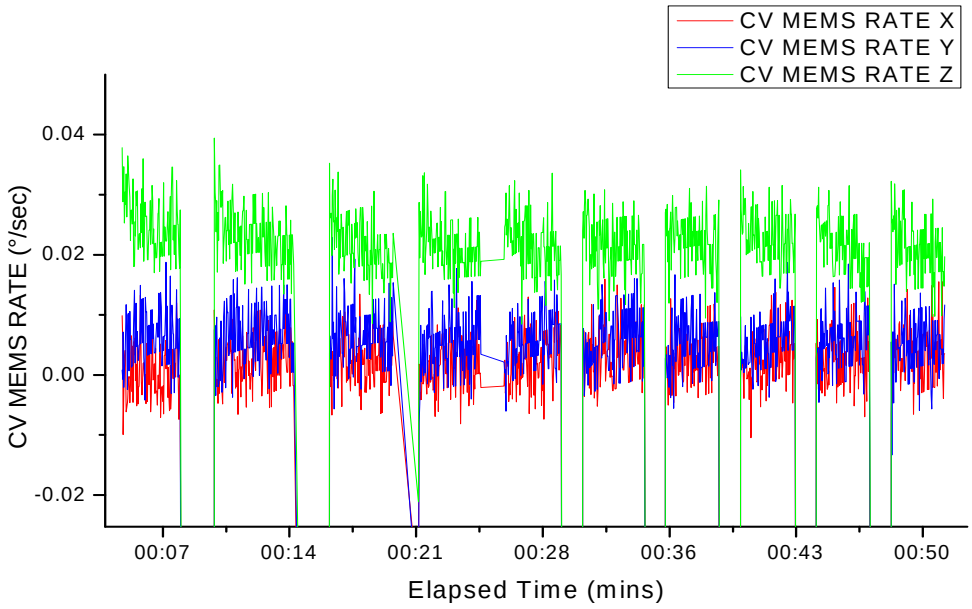

Figure 59. Short Duration Tests (1-10)

Figure 60. Variance of the 200 point averages in Test 1

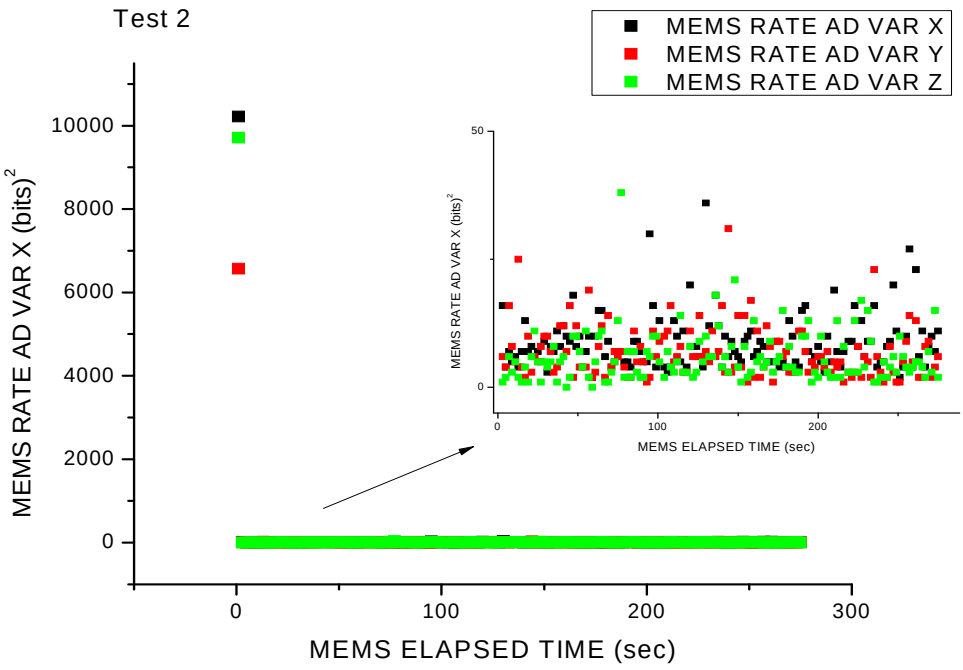

Figure 61. Variance of the 200 point averages in Test 2. The first few points right after turn on are typically very large variances and will not be used by the ACS.

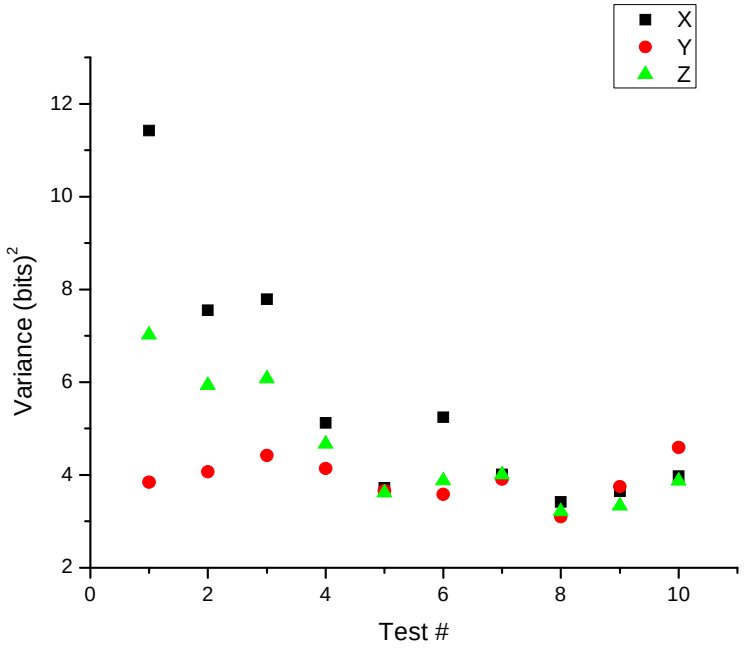

Figure 62. Variance between tests

3. Drift Characterization Using Allan Variance

The purpose of this section is to present the initial characterization results of random drift rate using the Allan variance technique.

Allan variance is a time domain analysis technique used to determine the character of the underlying random processes that give rise to the data noise. It is defined as:

$$\sigma^2(T) = \frac{1}{2}\langle[\overline{\Omega}_{\text{next}}(T) - \overline{\Omega}_{\text{k}}(T)]^2\rangle \tag{18}$$

where T is the cluster time, which is equal to nt_o and $n = 1,2,3,\ldots N$, t_o is the sample time; $\overline{\Omega}_{\text{k}}(T)$ is the cluster average of the instantaneous rate output $\Omega(t)$ and, and $\overline{\Omega}_{\text{next}}(T)$ is the subsequent cluster average. The cluster average is defined as:

$$\overline{\Omega}_{\text{k}}(T) = \frac{1}{T}\int_{\text{t}_\text{k}}^{\text{t}_\text{k}+T} \Omega(t)dt \tag{19}$$

where $\overline{\Omega}_{\text{k}}(T)$ starts from k$^{\text{th}}$ data point and contains n data points. Moreover, the subsequent cluster average is given by:

$$\overline{\Omega}_{\text{next}}(T) = \frac{1}{\text{T}}\int_{\text{t}_{\text{k}+1}}^{\text{t}_{\text{k}+1}+T} \Omega(\text{t})dt \tag{20}$$

where $\text{t}_{\text{k}+1} = \text{t}_\text{k} + T$.

The Allan variance method provides a way of estimating the different noise components that exist in the data. The noise components in typical gyroscope models include: quantization noise, angle random walk (ARW), correlated noise (Markov), sinusoidal error, bias instability, rate random walk and rate ramp. Static data is fed into the above equations and the result is typically plotted as the *square root* of the Allan variance (Allan deviation) versus T on a log-log plot. Any number of noise components can be present in the data. A typical plot showing different variance components are shown in Figure 63. For this initial modeling, the main interest is to estimate ARW, bias instability, and rate random walk, which were defined in Section II-B and named in [20] as three usual noise terms of random drift.

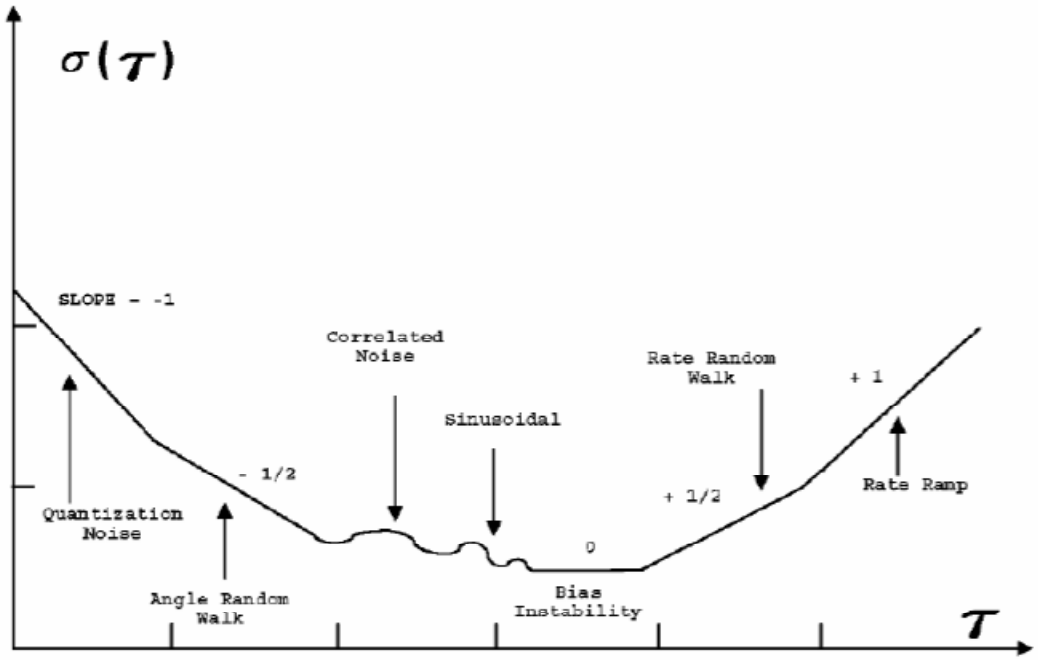

Figure 63. Sample Plot of Allan Variance Analysis Results Showing Different Noise Components (From [33]).

As seen in the figure above, the components are identified by the slope of $\sigma(T)$ segment[16]. The details of these components and their derivation are described in [32] and [33]. Briefly, by relating Equation (18) to the power spectral density (PSD)[17], $\sigma(T)$ can be reduced to the following equations:

1. For ARW, Equation (18) simplifies to,

$$\sigma(T) = \frac{N}{\sqrt{T}} \tag{21}$$

where N is the angle random walk coefficient. By reading the -1/2 slope line, the value of $\sigma(T)$ can be obtained at T = 1 hour.

2. For bias instability, the Allan deviation reaches a plateau for T much longer than the inverse of the cut off frequency. Bias instability can be obtained from:

[16] From [27], gradual transitions would exist between the slopes with real data.

[17] PSD is the most commonly used representation of spectral decomposition of a time series. It is a positive real function of a frequency variable associated with a stationary stochastic process, or a deterministic function of time, which has dimensions of power per Hz, or energy per Hz [37].

$$\sigma(T) \cong 0.664\text{B} \tag{22}$$

where *B* is the bias instability coefficient. From this relationship, the slope is zero and *B* can be solved from where the horizontal line crosses $\sigma(T)$.

3. For rate ramp, the Allan deviation is given by,

$$\sigma(T) = R\frac{T}{\sqrt{2}} \tag{23}$$

where *R* is the rate ramp coefficient. The value of *R* can be read from where the +1 slope line intersects $T = \sqrt{2}$ hour.

a. Results

Using data collected in the vacuum tests, the Allan standard deviation was plotted using the MATLAB source code from [34]. The data sets selected for this characterization are two-hours long. Additionally, these sample sets are temperature and pressure compensated rates taken after the initial transients have settled. The results are shown in Figure 64.

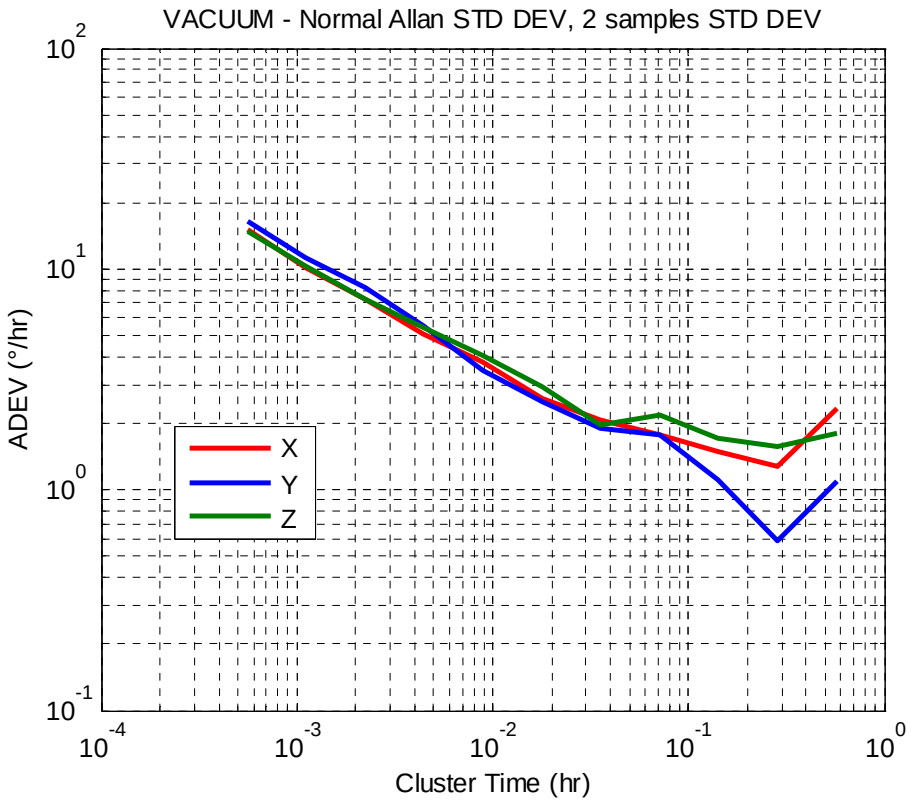

Figure 64. Allan Deviation of 2 hour data

The plots show that the dominant noise term for shorter cluster time is ARW, while the higher cluster time indicates (for X and Y) that rate ramp is dominant. The plots do not contain regions with zero slopes. As a *preliminary* estimate, the bias instability for each sensor was taken at the minimum points of the graphs. The noise values were obtained as shown in Figure 65 and the results are summarized in Table 13.

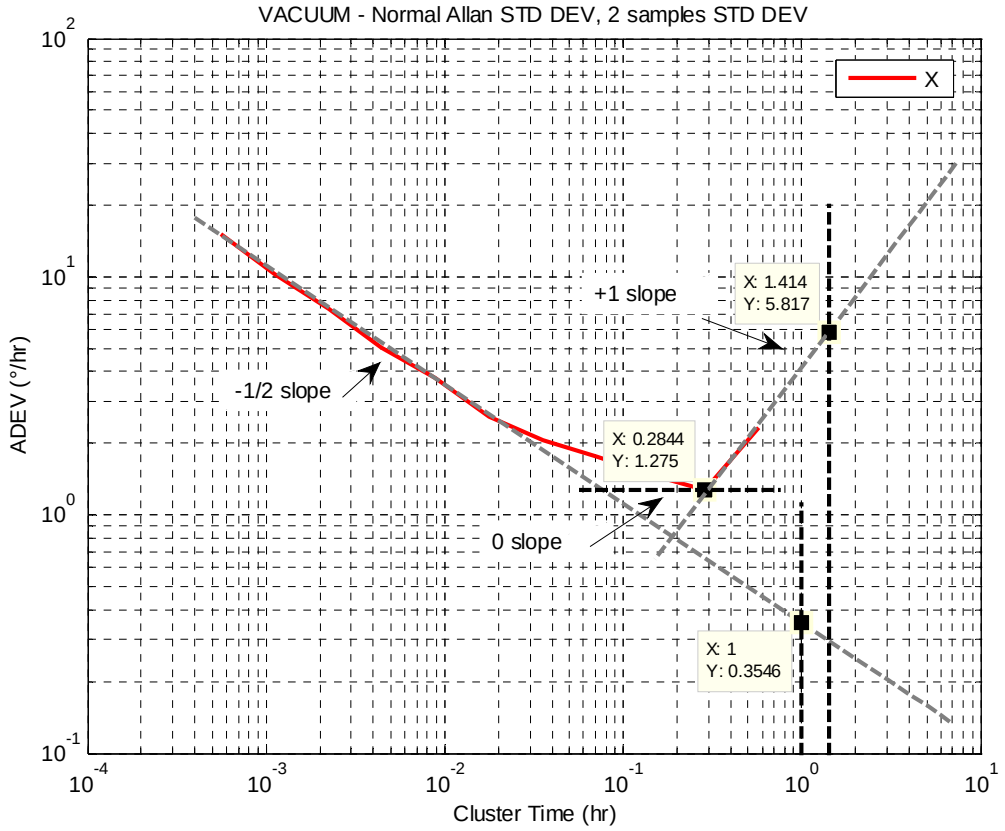

Figure 65. Sample Plot Showing Noise Components from Slope of Fitted Line

The results in Table 13 show that the bias instability for the X and Y sensors are less than the Z sensors. From previous tests, however, the Z sensor has demonstrated to be the most stable, while the X sensor has shown to be the one that has the largest drift. This inconsistency may be an indication that long-term data is required to obtain better estimates of the bias instability, as well as identification of other noise components.

The quality of Allan variance estimation depends on the number of independent clusters, and the confidence improves as the number of clusters is increased. It is recommended to design a test to observe a particular noise term within a given accuracy using the equations provided in reference [33], page 78 (Annex C.2 Estimation accuracy and test design, Equation C.22).

Table 13. Summary of Initial Noise Analysis

Sensor	ARW, -1/2 slope, T = 1, ($°/h^{1/2}$)	Bias instability, 0 slope, (°/h) {estimate only}	Rate ramp, +1 slope, T = √2, (°/h/√h) {estimate only}
Gyro X	0.3546	1.920	5.817
Gyro Y	0.386	0.886	2.71
Gyro Z	0.352	2.381	--

H. SUMMARY

The results of the tests are summarized in Table 14:

Table 14. Summary of Results, Comparison to Previous Research and Manufacturer Data

<table>
<tr><th>Test</th><th>Results</th><th>Previous Research</th><th>Manufacturer Data</th></tr>
<tr><td>Startup Profile/ initial transients</td><td>Startup time cannot be determined due to software setup.

Bottom line: Initial transients are of more concern. After thermal & pressure compensation, the transients take 1–1.5 hrs to settle. This transition time is consistent with that observed in [11].

See pg. 63</td><td>Characteristic transition ~ 1 sec ([2], pg. 66)

Warm-up 5 minutes. ([2] pg. 120, 128)</td><td>Typical < 1 sec, (data sheet)</td></tr>
<tr><td>Nominal Temperature Voltage</td><td>New gain used in filter to increase temperature output range. The new nominal temperature voltages are:

<table><tr><th>Sensor</th><th>V_n (V)</th><th>T_{ave} (°C)</th></tr><tr><td>-X</td><td>-0.5042</td><td>25.7</td></tr><tr><td>Y</td><td>-0.4909</td><td>25.4</td></tr><tr><td>-Z</td><td>-0.5071</td><td>25.3</td></tr></table>
See pg. 37

Due to uncertainties with temperature conversion equation, polynomial fitting did not use °C converted temperature.</td><td>From old gain value:
<table><tr><th>Sensor</th><th>Vn</th></tr><tr><td>-X</td><td>-0.3724</td></tr><tr><td>Y</td><td>-0.1995</td></tr><tr><td>-Z</td><td>-0.3932</td></tr></table>
([2], pg. 28)

Note: sensor sign is the orientation relative to spacecraft (sensor mounted up-side down)</td><td>-0.100 to +0.050 Vdc @ +25°C</td></tr>
<tr><td>Ambient Pressure Chamber Tests

Hysteresis</td><td>Ramp up and down curve misalignment not directly attributed to hysteresis; partially due to random and/ or curve fit errors. See pgs. 42- 43.

Our method is slightly different in</td><td>Hysteresis effects observed in [11]

Test conducted at 10°C up to +40°C and back down to -10°C at 5°C steps. All points</td><td>N/A</td></tr>
</table>

Test	Results	Previous Research	Manufacturer Data
	that no incremental steps taken.	collected used for polynomial fitting.	
Repeatability	When rate output is in raw A/D bits form, run-to run biases were observed between tests starting at different temperatures. *Most* errors are reduced to negligible amounts after converting raw output from bits to volts. However, errors of up to ~0.016°/sec have been observed to occur at random in both ambient and vacuum environments. Run-to-run errors cannot be calibrated. See pgs. 44-46.	[18] pg. 41;[22] pg. 112, describes Run-to-run (repeatability) bias.	N/A
Thermal Ramp	Polynomial equations extracted for ground tests only. See pg. 47.	Equations from [2] needed to be updated for new Y sensor and to account for interface errors.	Model equation: cubic (unique for each sensor)
Vacuum Chamber Tests			
Mechanical Noise	Noise tests show that mechanical noise has minimal effect on sensor output. This allowed to keep vacuum running while data gathering. Data collected in between heating and cooling cycles. See pgs. 51- 53.	Mechanical noise concerns in [2]; recommended to shut off TVC power once desired temp during data gathering. This is an issue for vacuum tests since the chamber isolation valve cannot not hold desired vacuum level for long.	N/A (test equipment dependent)
Vacuum Degree Test	Verified that vacuum level changes effect on MEMS are at minimum during thermal ramp test. See pgs. 53-55.	[11][27] showed pressure dependency of bias. Initial result showed that gyros acquired relatively fixed but unique offset in vacuum [27].	
Hysteresis	Same results as ambient pressure tests. See pgs. 56-57	N/A	
Repeatability	Same results as ambient pressure tests. See pgs. 56-58.	N/A	

Test	Results	Previous Research	Manufacturer Data
Thermal Ramp	Compensation polynomials extracted for pressure & thermal $B_{in\text{-}run.}$ See pg. 59	N/A	
Rate Testing	MEMS + ACS Resolution: 0.1–0.2 °/sec (direct measurement) Alternative method using reference: ~0.04 °/sec Rate equation modified to account for scale factor error & nonorthogonality. See pgs. 66-77	[2] pg. 136, Resolution: >0.05 °/sec (@ 5% requirement)	±5 mV/(°/sec)
Random Vibration	Workmanship screening—visual inspection and functional test results showed no significant changes to scale factor and bias after vibration test. See pgs. 81-87	N/A	
Other:			
ACS Interval Test	Data save interval skips occasionally. Software update required to ensure that ACS receives MEMS data every 2 secs. See pg. 91	N/A	N/A
Variance	Variance within test large compared to variance between tests. Sampling rate not recommended to be lowered. See pg. 91	N/A	N/A
Allan Variance	ARW dominant at lower cluster times; bias instability and rate ramp require more data to get better estimates. See pgs. 96-99	N/A	Short term bias stability $\leq$ 0.01°/sec, typical (100 sec) Output noise $\leq$ 0.01°/√Hz (for ±100 °/sec range)

From the preceding tests, the static error compensation values of Equation (2) were determined, as well as the nominal voltages for converting the raw temperature output to °C. The three outputs of the MEMS subsystem are summarized in Table 15.

Table 15. MEMS Output

Output	Terms	X	Y	Z
Rate	form	$\tilde{\boldsymbol{\omega}} = \boldsymbol{I}_{\tilde{\omega}} - (\boldsymbol{b}_{\boldsymbol{in-run}} + \boldsymbol{M}\tilde{\boldsymbol{\omega}} + \boldsymbol{b}_{\boldsymbol{cons}}) - \boldsymbol{b}_{\boldsymbol{run-to-run}} - \boldsymbol{\varepsilon}(\tilde{\boldsymbol{\omega}})$		
	$I_{\tilde{\omega}}$	$= R_{ave} * \frac{1}{S_f}$ *where,* $R_{ave}\,(\mathrm{V}) = \left(\frac{R_{ave}(\mathrm{bits})}{4095} \times 5\right) - R_{shift}$		
	$b_{in\text{-}run}$ *(orbit-thermal & pressure)*	$= B + m_1 * T_m^1 + m_2 * T_m^2 + m_3 * T_m^3$ where, $T_m(\mathrm{V}) = \left(\frac{T_m\,(\mathrm{bits})}{4095} \times 5\right) - T_{shift}$		
	B	-0.00809	0.0038	0.03219
	m_1	-0.05675	-0.01519	-0.01581
	m_2	-0.0107	-0.0037	-0.01039
	m_3	-0.00503	-0.00402	-0.00796
	$M_{B\text{-}dot}$	$= \begin{pmatrix} S_x & m_{xy} & m_{xz} \\ m_{yx} & S_y & m_{yz} \\ m_{zx} & m_{zy} & S_z \end{pmatrix} = \begin{pmatrix} 0.042 & 0.102 & 1.298 \\ -0.156 & -0.4 & 0.128 \\ -0.2 & -0.139 & 0.506 \end{pmatrix}$		
	$b_{cons(B\text{-}dot)}$	$7.18E-03$	$-8.12E-03$	$7.00E-03$
Temperature	$T(°C)$	$T_x = 25.7°C + \frac{0.5042 + T_{mx}}{0.0264}$	$T_y = 25.4°C + \frac{0.4909 + T_{my}}{0.0264}$	$T_z = 25.3°C + \frac{0.5071 + T_{mz}}{0.0264}$
BIT	BIT (V)	$= \left(\frac{BIT\ (\mathrm{bits})}{4095} \times 5\right)$		

THIS PAGE INTENTIONALLY LEFT BLANK

V. CONCLUSIONS AND FOLLOW-ON WORK

A. CONCLUSIONS

The NPSAT1 MEMS 3-axis rate sensor protoflight unit was characterized and tested in 2007; the author of [2] reported finding literature that described vacuum effects on the rate output of the QRS11 sensor [11]. Thereafter, a SSAG recommendation and decision was made to fly the MEMS subsystem unpressurized. This new requirement, along with the replacement of a damaged sensor (Y), necessitated the recalibration of the MEMS subsystem.

In this thesis, the issues presented in [2] and [11] were addressed. The pressure dependence of the rate bias was determined in conjunction with the thermal drift errors. In addition, the opportunity was taken to investigate other inertial sensor error sources such as hysteresis, repeatability (in relation to startup temperature), scale factor error, nonorthogonality, noise, and vibration sensitivity. These errors were methodologically categorized according to the models in [15], [19] and [22].

The main contributions of this thesis to the NPSAT1 program are:

1. Identification of deterministic error terms through laboratory testing: b_{cons}, which is the constant portion of the bias; b_{in-run} or the stability bias with temperature and pressure in the form of a third-order polynomial; and *M*, which is a matrix coefficient containing the scale factor and nonorthogonality errors of the sensors.

- The in-run bias results for the ambient thermal ramp polynomials acquired additional biases of ~0.05°/sec, ~0.01°/sec, ~0.03°/sec for X, Y, and Z, correspondingly, when placed in vacuum.
- The static tests in vacuum showed that the stabilization period could last up to 1.5 hours even with thermal and pressure compensation. During this stabilization, absolute bias errors of up to ~0.02°/sec, ~0.015°/sec, and ~0.016°/sec were recorded for the X, Y, and Z sensors, correspondingly. Although the initial transients are long and an important consideration for

spacecraft operation or pointing, these uncertainties are small enough for the B-dot or detumbling mode.

2. Gained an understanding of the repeatability errors and addressed the hysteresis effects mentioned in [11]. The results indicate that these effects are at a minimum.

3. Re-evaluated the sensors' accuracy through dynamic tests and verified that the MEMS subsystem in its current setup with the ACS meets the requirement for the initial part of detumbling, down to about 0.1–0.2 °/sec. The accuracy results were based on error results using b_{in-run} compensated rates. This is the minimum compensation factor and the estimates are thus conservative.

4. Tested the robustness of the MEMS subsystem and verified that it meets the vibration requirements and acceptance levels. The functional tests indicate no significant changes to the scale factor and bias (constant portion).

This thesis concludes with some recommendations and follow-on research work.

B. FOLLOW-ON TOPICS

1. Warm-Up Drift

It may be possible to improve the in-run compensation by using separate drift compensation during the warm-up period. An idea to test this possibility requires several ~2 hour static vacuum tests. The tests should be started at different temperatures (e.g. at temperatures within the operating range). If a relationship between the temperature and time or rate and time can be established, then a time dependent drift can be used during the warm-up period.

2. Allan Variance Characterization

In Section IV-G, initial modeling of the noise components was performed on available static data from the tests performed in vacuum. Two-hour data was used for this initial analysis. The results show that ARW is dominant for shorter cluster times. A longer data set may be required to reliably identify the bias instability and rate ramp, as well as other noise components that could be present in the system. The quality of Allan

variance estimation depends on the number of independent clusters, and the confidence improves as the number of clusters is increased. As suggested earlier, it is recommended to design a test to observe a particular noise term within a given accuracy using the equations provided in reference [33], page 78 (Annex C.2 Estimation accuracy and test design, Equation C.22). It is also suggested to apply the alternative methods described in [11] and compare the results to the traditional Allan variance results. Prior to data collection, the software should be updated to include the results summarized in Table 15.

The results of the follow-on work described here, are parameters that are required for designing the process noise matrix of the extended Kalman filter algorithm.

3. Noise Filtering

As listed in [2], Kalman filtering is still an open topic for this program. The extended Kalman filter is commonly used; however, a study should be done to determine the most optimal type of filter to implement.

4. Verification and Validation of Final Error Compensation Algorithm

The accuracy results were derived from rates that were compensated using the $b_{in\text{-}run}$ term. This in-run bias compensation is the minimum for the B-dot mode. The compensation terms b_{cons} and M were derived from the rate table tests and offer additional improvement in the compensation; while the terms $b_{run\text{-}run}$ and $\varepsilon(\tilde{\omega})$ have yet to be decided on and determined. Once the error compensation algorithm is finalized, a test should be conducted to verify and validate the algorithm. This step would determine the accuracy of the system.

5. Initial Alignment

Alignment is the procedure of determining the initial values of the attitude angles [19]. A study is needed to determine the method to use for this initialization.

a. Gyro Bias Calibration from Three-Axis Magnetometer Measurements

Reference [35] presents a real-time approach for gyro bias calibration using three-axis magnetometer measurements without any attitude knowledge. This paper is listed here for the benefit of the reader. Additional papers that could be of potential interest to the reader are listed in the Bibliography section.

APPENDICES

Appendix A	QRS11 Performance Specification
Appendix B	Main Test List
Appendix C	Schematics
Appendix D	Hysteresis Test Results
Appendix E	Scale Factor and Nonorthogonality Report X
Appendix F	Scale Factor and Nonorthogonality Report Y
Appendix G	Scale Factor and Nonorthogonality Report Z
Appendix H	Scale Factor and Nonorthogonality Report X, without reference
Appendix I	Scale Factor and Nonorthogonality Report Y, without reference
Appendix J	Scale Factor and Nonorthogonality Report Z, without reference
Appendix K	Error of Curve Fit for MEMS Elapsed Time < 5 minutes
Appendix L	Earth Rate Component

A. QRS11 PERFORMANCE SPECIFICATION

PARAMETER	SUMMARY SPECIFICATIONS		
Part Number	QRS11-00100-100	QRS11-00100-101	QRS11-00005-565
Performance Level	Standard	High	High
Power Requirements			
Input Voltage	+ and – 5 Vdc ±3% regulation		
Input Current	≤80 mA (each supply)		
Input Power Noise Limits	<10 mV_{rms} wideband, except at 8.7 ±0.5 kHz, <1 mV_{rms}		
Performance			
Standard Range Full Scale	± 100°/sec.		±5°/sec
Full Scale Output (Nominal)	±2.5 Vdc		
Scale Factor Calibration (at 22°C Typical)	≤1% of value		
Scale Factor over Temperature (Dev. from 22°C Typical)	≤0.03%/°C		
Bias Calibration (at 22°C Typical)	≤2.0°/sec.*	≤0.5°/sec.*	0.131°/sec
Bias Variation over Temperature (Dev. from 22°C)	≤1.80°/sec.*	≤0.35°/sec.*	0.117°/sec
Short Term Bias Stability (100 sec at const. temp)	<0.01°/sec, typical*		
Long Term Bias Stability (1 year)	≤0.2°/sec.*		
G Sensitivity (Typical)	≤0.02°/sec/g		
Start-Up Time (Typical)	< 1 sec.		
Bandwidth (-90°)	>60 Hz		
Non-Linearity (Typical) % Full Range	≤0.05%		
Threshold/Resolution	≤0.004°/sec.*		
Output Noise (DC to 100 Hz)	≤0.01°/sec./√Hz*		0.004°/sec/√Hz
Environments			
Operating Temperature	-40°C to +80°C		
Storage Temperature	-55°C to +100°C		
Vibration Operating	8 g_{rms} 20 Hz to 2 kHz Random (Consult factory for other vibration level requirements)		
Vibration Survival	20 g_{rms} 20 Hz to 2 kHz random 5 minutes/axis		
Shock	200g, any axis		
Weight	≤60 grams		
AVAILABLE OPTIONS			
• Special Non-Standard Ranges <±100°/sec. and >±100°/sec., Consult Factory • Extended Bandwidth • Low Noise • Extended Temperature Range • Flying Leads			
*Values indicated are for ±100°/sec. range			

Appendix Figure 1. QRS11 Performance specification

B. MAIN TEST LIST

All tests are provided for NPS use. "ACS ID" is an NPS SSAG internal reference number. TS = UNIX time stamp.

Appendix Table 1 lists the thermal ramp tests in ambient. The naming convention is as follows:

TVAC = Chamber Tests Ambient Pressure/Vacuum pumps off
Recirc = Recirculator Tests

Appendix Table 1. Test List for Thermal Chamber and Recirculator Tests

Purpose	Test ID	Temperature Range	Notes	ACS ID	TS Start *first 300 secs removed	TS End
TVC Practice				1		
Temperature Test				15		
HAAS Practice Test				16		
TVC MEMS Nominal Test			Temp did not stabilize; Moved to Cold Plate	lost		
Cold Plate Nominal Test			1st try	20		

Purpose	Test ID	Temperature Range	Notes	ACS ID	TS Start *first 300 secs removed	TS End
Cold Plate Nominal Test			Rotated MEMS -90 deg, MEMS temp better, this is the data set used for nominal voltage calculations	21		
AMBIENT PRESSURE TESTS 1. Thermal Ramp up/down Test 2. Hysteresis Effects Test 3. Effect of initial temperature at startup	TVAC1–1a	+64°C to -27°C	Cooldown	27	1272475321	1272504689
	TVAC1–1b	-27°C to +27°C	Warmup	27	1272474371	1272531461
	TVAC1–2a	-27°C to +27°C	Warmup	28	1272571957	1272643199
	TVAC2–1a	+66°C to -29°C	Cooldown, meet qualification range	203	1282605684	1282617850
	TVAC2–2a (used to 2–1b)	-29°C to +66°C	Test Hysteresis effect, warmup	204	1282667147	1282676304
	Recirc1–1a	+25°C to +6°C	Test Hysteresis effect, cooldown	239	1282948116	1282954713
	Recirc1–1b	+6°C to +12°C	Test Hysteresis effect, warmup	239	1282954717	1282955566
	Recirc1–2a	+16°C to +6°C	Cooldown	239	1282956386	1282959821
	Recirc1–2b	~+4°C to +25°C	warmup	239	1282959823	1282962803
	Recirc2–1a	+4°C to +25°C	warmup	240	1283202960	1283206656
	Recirc2–1b	+26°C to ~6°C	cooldown	240	1283206658	1283212519
	Recirc2–1c	~+6.5°C to +27°C	warmup	240	1283212521	1283215955
	TVAC3–	-17°C to +12.8	warmup	241	1283235369	1283237609

Purpose	Test ID	Temperature Range	Notes	ACS ID	TS Start *first 300 secs removed	TS End
	1a	°C				
	TVAC3–1b	+18°C to -7°C	cooldown	241	1283238321	1283241101
VACUUM TESTS	FL0–1 (formerly called Vac1)	+10°C to +14°C	These tests were intended to test MEMS under different vacuum levels	31	1272773185	1272776857
	FL0–2 (formerly called Vac2)	+22°C to +29°C		32	1272933747	1272935763
	FL0–3 (formerly called Vac3)	+25°C to +31°C		33	1272944942	1272946644
	FL0–4 (formerly called Vac4)	-23.5°C to -19.5°C		34	1272989784	1272993586
	FL0–5 (formerly called Vac5)	-21°C to -13°C		35	1272999276	1273000598
	FL1–1a	+23°C to +29°C	No heat/refrigeration,	206	1282691102	1282695210
	FL1–1b	+30°C to 23°C		206	1282695214	1282707778
	FL2–1a	+77°C to -21°C	Under vacuum, cooldown	242	1283281936	1283311017
	FL2–2a	-11°C to -10.77°C	Under Vacuum, warmup	243	1283357875	1283358137
	FL2–2b		Under vacuum, Cooldown—not intentional, should have been a warmup but heating was too slow and	243		

Purpose	Test ID	Temperature Range	Notes	ACS ID	TS Start *first 300 secs removed	TS End
			unit cooled down			
	FL2–2c	-11°C to +19°C	Under Vacuum, warmup	243	12833581390	12833645430
	FL2–2d	+19°C to +16°C	Under vacuum, cooldown	243	1283364545	1283365803
	FL2–3a	15°C to 2°C	Under vacuum, cooldown	243	1283366113	1283367781
	FL2–4st		Ambient pressure, Startup profile *Data too short <300 secs	243	1283367785	1283368010
Noise Test—Main On				29		
Mech Pump Noise Test (Pump on)				30	1272690062	1272691939
Mech Pump Noise Test (Pump off)				30	1272692033	1272693781
Vacuum Degree Test	Vac1 Test		Test with Mech, Turbo, Cold trap; Pressure at 6E-6 to 9.2E-6	31	1272773185	1272776857
	Vac2 Test		Test with just Mech Pump on, Vents closed	32	1272933567	1272935763
	Vac3 Test		Test with Mech, Turbo, No Cold trap;	33	1272944762	1272946644
	Vac4 Test		Test with Mech, Turbo,	34	1272951897	1272993586

Purpose	Test ID	Temperature Range	Notes	ACS ID	TS Start *first 300 secs removed	TS End
			LN2, Subzero			
	Vac5 Test		From 4, turned off LN2, turned on heat for 17mins, turned off turbo and record while pressure	35	1272999276	1273000598

Appendix Table 2. Rate Table Tests

Purpose	Test Axis	Test Input (°/sec)	ACS ID	Rotation (+/-)	Notes
RATE TRANSFER TESTING	Z	5	81	300	
		4.5	82	270	
		4	83	240	
		3.5	84	210	
		3	85	180	
		2.5	86	150	
		2	87	120	
		1.5	88	90	
		1	89	60	
		0.5	90	30	
		0.45	91	27	
		0.4	92	24	
		0.35	93	21	
		0.3	94	18	
		0.25	95	15	
		0.2	96	12	
		0.15	97	9	
		0.1	98	6	
		0.09	99	5.4	
		0.08	100	4.8	
		0.07	101	4.2	
		0.06	102	3.6	
		0.05	103	3	
		0.04	104	2.4	
		0.03	106	1.8	
		0.02	105	1.2	
		0.01	107	0.6	
		0.009	108	2.34	
		0.009	109	-2.34	
		0.008	110	2.08	
		0.008	111	-2.08	
		0.007	112	1.82	
		0.007	113	-1.82	
		0.006	114	1.56	
		0.006	115	-1.56	
	X	5	117	300	
		4.5	118	270	
		4	119	240	
		3.5	120	210	
		3	121	180	

Purpose	Test Axis	Test Input (°/sec)	ACS ID	Rotation (+/-)	Notes
		2.5	122	150	
		2	123	120	
		1.5	124	90	
		1	125	60	
		0.5	126	30	
		0.4	128	24	
		0.3	129	18	
		0.2	130	12	
		0.1	131	6	
		0.09	133	5.4	
		0.08	134	4.8	
		0.07	135	4.2	
		0.06	136	3.6	
		0.05	137	3	
		0.04	138	2.4	
		0.03	139	1.8	
		0.02	140	1.2	
		0.01	141	0.6	
		0.009	132	2.34	
		0.008	142	2.08	
		0.007	143	1.82	
		0.006	144	1.56	
	Y	5	145	300	
		4.5	146	270	
		4	147	240	
		3.5	148	210	
		3	149	180	
		2.5	150	150	
		2	151	120	
		1.5	152	90	
		1	153	60	
		0.5	154	30	
		0.4	155	24	
		0.3	156	18	
		0.2	157	12	
		0.1	158	6	
		0.09	159	5.4	
		0.08	160	4.8	
		0.07	161	4.2	
		0.06	162	3.6	
		0.004	163	1.04	

Purpose	Test Axis	Test Input (°/sec)	ACS ID	Rotation (+/-)	Notes
	Z	5	41	300	Initial tests conducted with table not tilt (level). This series was not used for thesis analysis. Used for preliminary test purposes only.
		4.5	42	270	
		4	43	240	
		3.5	44	210	
		3	45	180	
		2.5	46	150	
		2	47	120	
		1.5	48	90	
		1	49	60	
		0.5	50	30	
		0.45	51	27	
		0.4	52	24	
		0.35	53	21	
		0.3	54	18	
		0.25	55	15	
		0.2	58	12	
		0.15	59	9	
		0.1	60	6	
		0.09	61	5.4	
		0.08	62	4.8	
		0.07	63	4.2	
		0.06	64	3.6	
		0.05	65	3	
		0.04	66	2.4	
		0.03	67	1.8	
		0.02	69	1.2	
		0.01	70	0.6	
		0.009	71	0.54	
		0.008	72	0.48	
		0.007	73	0.42	
		0.006	74	0.36	
		0.005	75	0.3	
		0.004	76	0.48	
		0.003	77	0.36	
		0.002	78	0.24	
		0.001	79	0.12	
EARTH RATE	Z	--	38		36.6
		--	39		-53.4
		--	40		0
		--	80		53.4
	-Y	--	164		53.6
		--	237		Tilt @ 52.6, problem with HAAS
	X	--	227		53.6

Purpose	Test Axis	Test Input (°/sec)	ACS ID	Rotation (+/-)	Notes
PRE VIBE	Z	5	209		
		0.5	210		
		0.05	211		
		0.006	212		
		-0.006	214		
		0.004	215		
		-0.004	216		
	X	5	219		
		0.5	220		
		0.05	222		
		0.006	223		
		0.006	224		
		0.004	225		
		0.004	226		
	Y	5	228		
		0.5	229		
		0.06	230		
		0.05	231		
		0.006	232		
		- 0.006	234		
		0.006	233		HAAS error—not used
		0.004	235		
		-0.004	235		
POST VIBE Z	Z	5	247		
		0.5	248		
		0.05	249		
	X	5	253		
		0.5	254		
		0.05	255		
	Y	5	250		
		0.5	251		
		0.05	252		
POST VIBE X	Z	5	256		
		0.5	257		
		0.05	258		
	X	5	259		
		0.5	260		delete first few minutes—bad data
		0.05	261		delete last minutes, forgot to disable program
	Y	5	264		

Purpose	Test Axis	Test Input (°/sec)	ACS ID	Rotation (+/-)	Notes
		0.5	263		
		0.05	262		
POST VIBE Y	Z	5	271		
		0.5	272		
		0.05	273		
	X	5	270		
		0.5	269		
		0.05	268		
	Y	5	265		delete first part—bad data
		0.5	266		
		0.05	267		
RUN TO RUN			245		
MAGNET TEST			246		NOT USED

C. SCHEMATICS

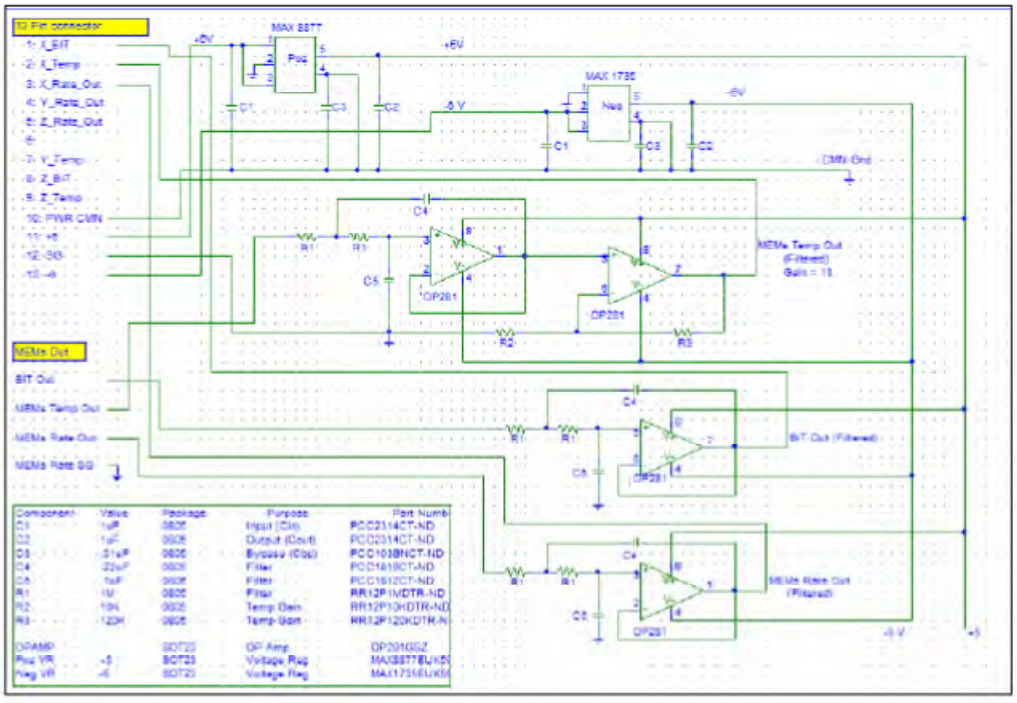

Appendix Figure 2. MEMS PCFB Schematic (From [2])

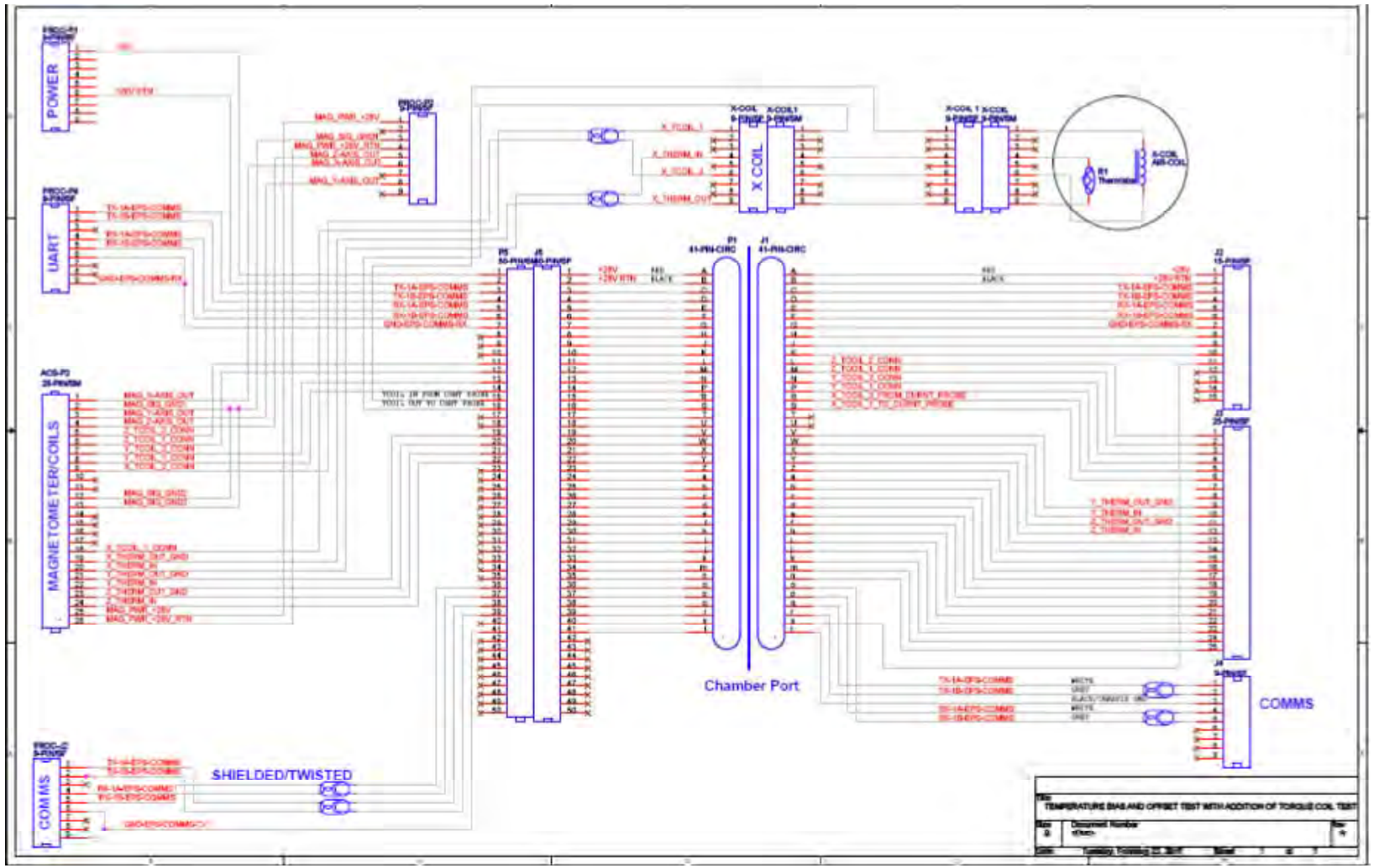

Appendix Figure 3. Thermal Chamber Setup Schematic (From R. Phelps)

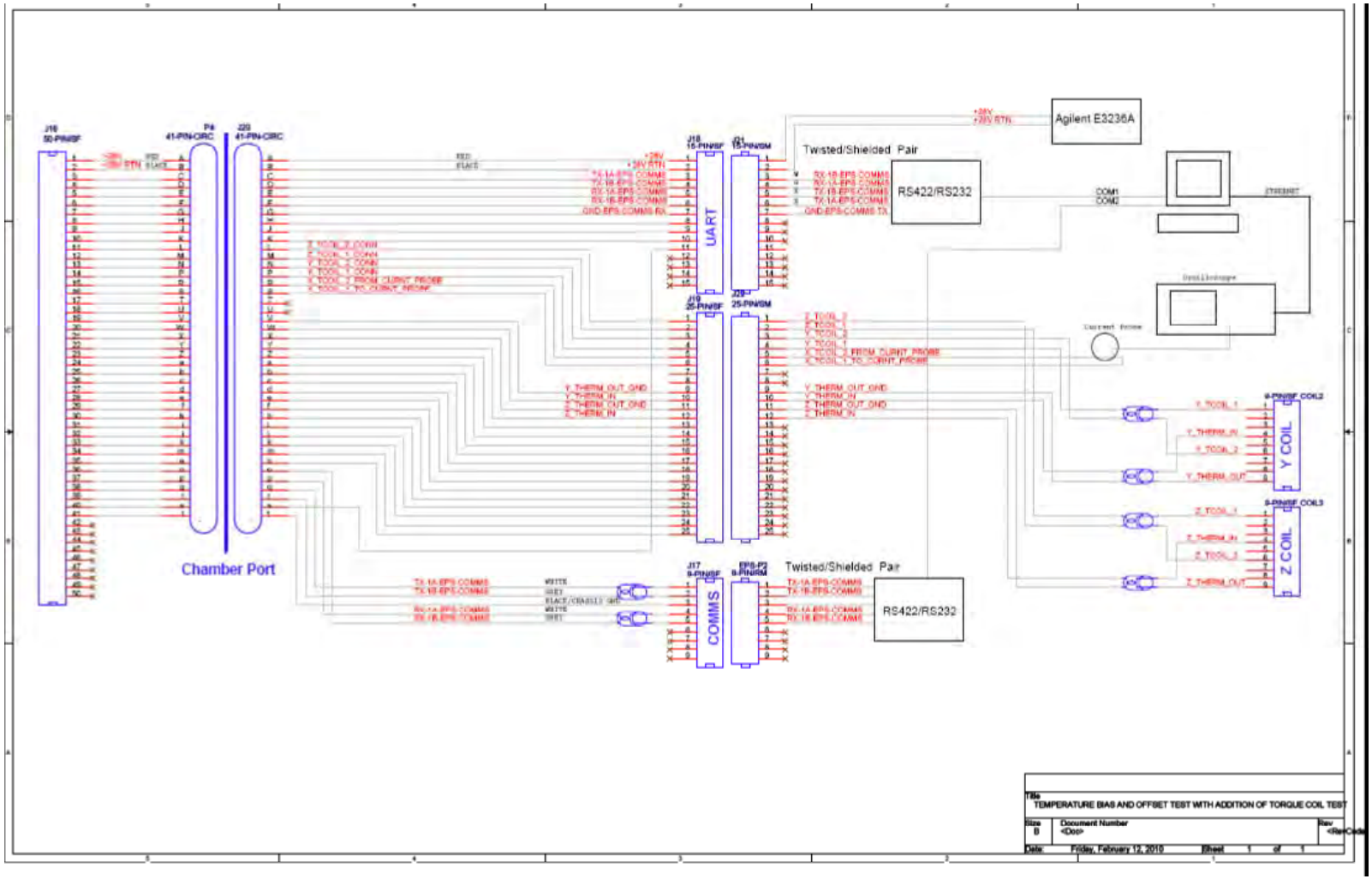

Appendix Figure 4. Thermal Chamber Setup Schematic, Outside Connections, (From R. Phelps)

D. HYSTERESIS TEST RESULTS

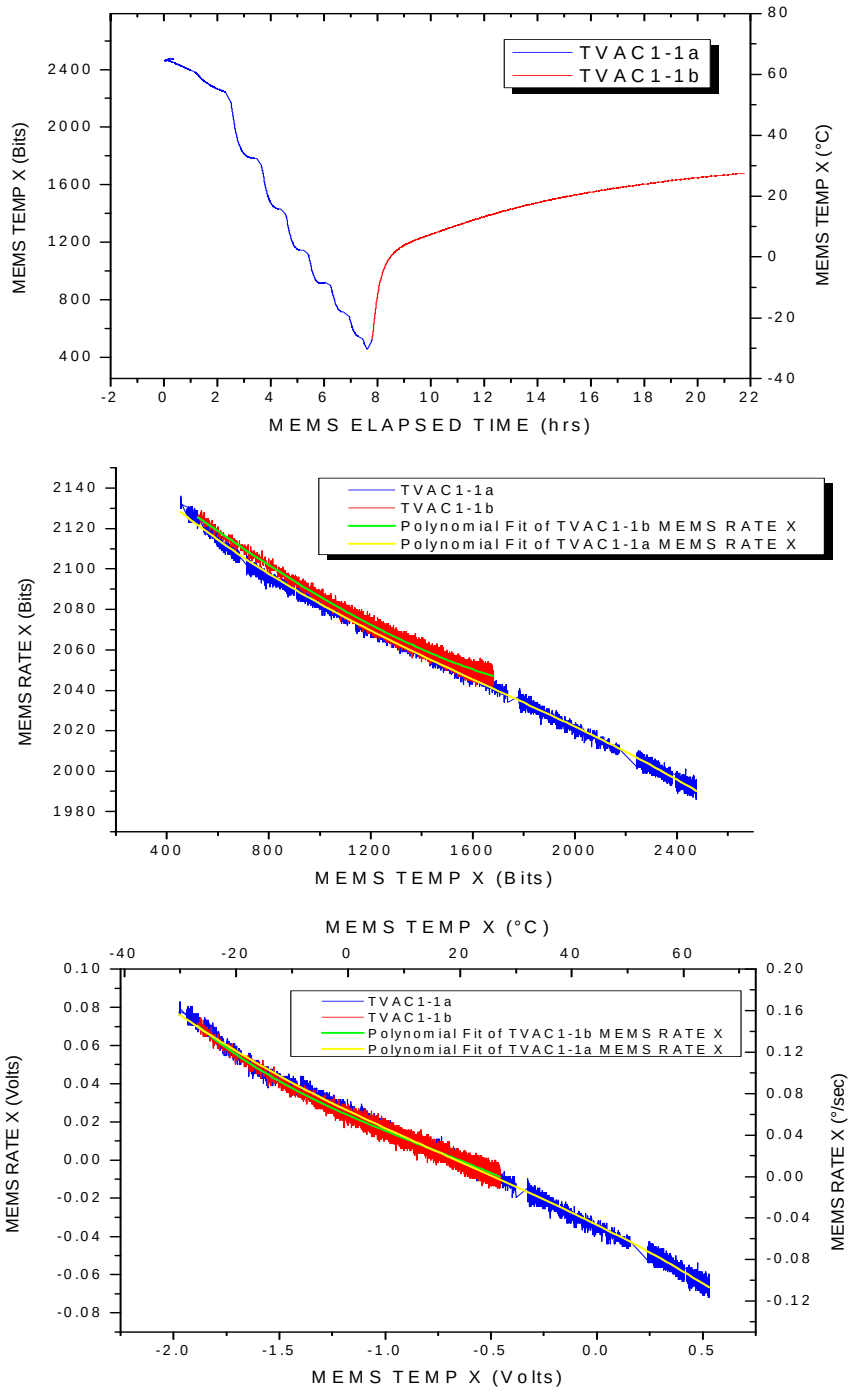

Appendix Figure 5. Hysteresis Test, TVAC1–1 (X)

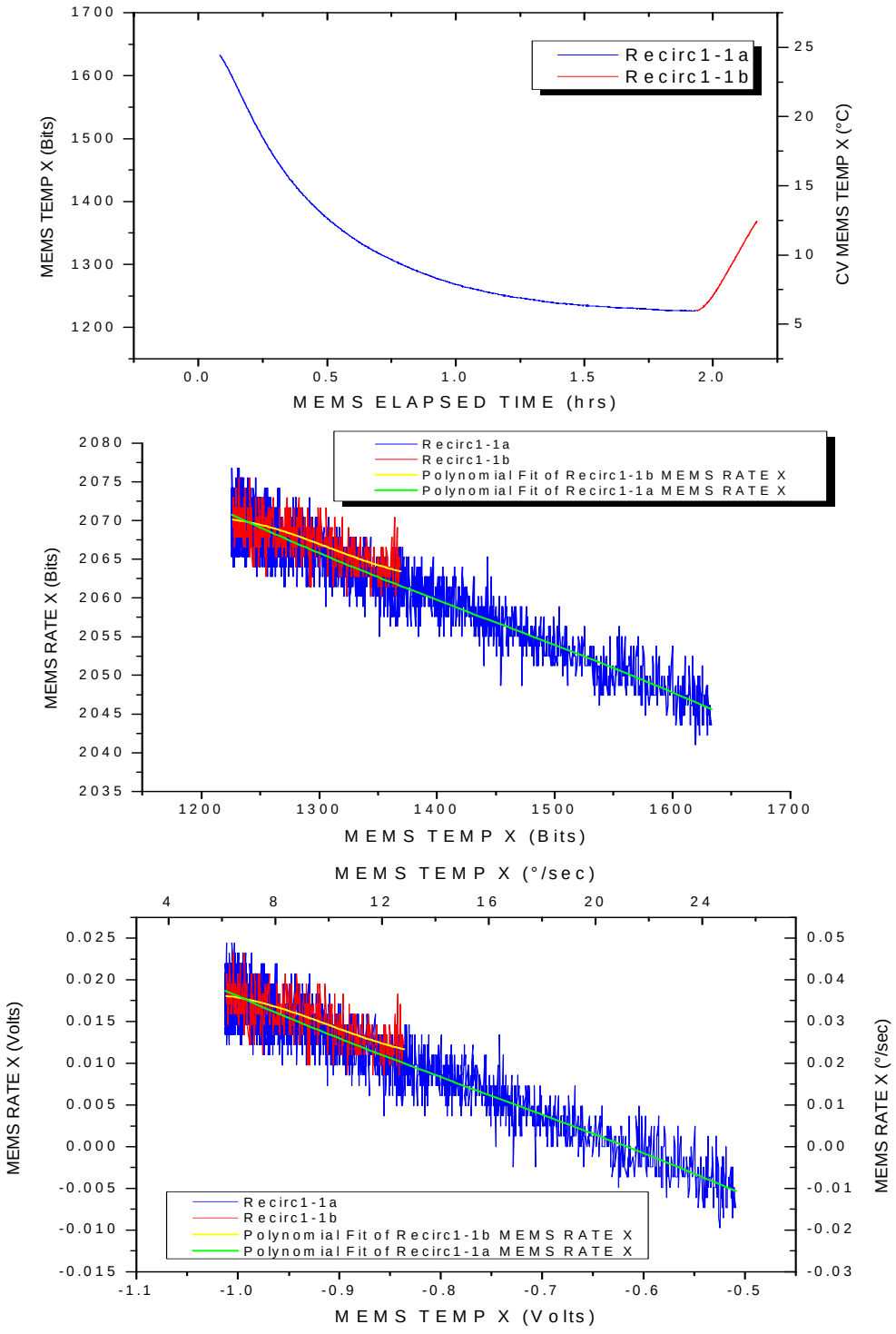

Appendix Figure 6. Hysteresis Test, Recirc1–1 (X)

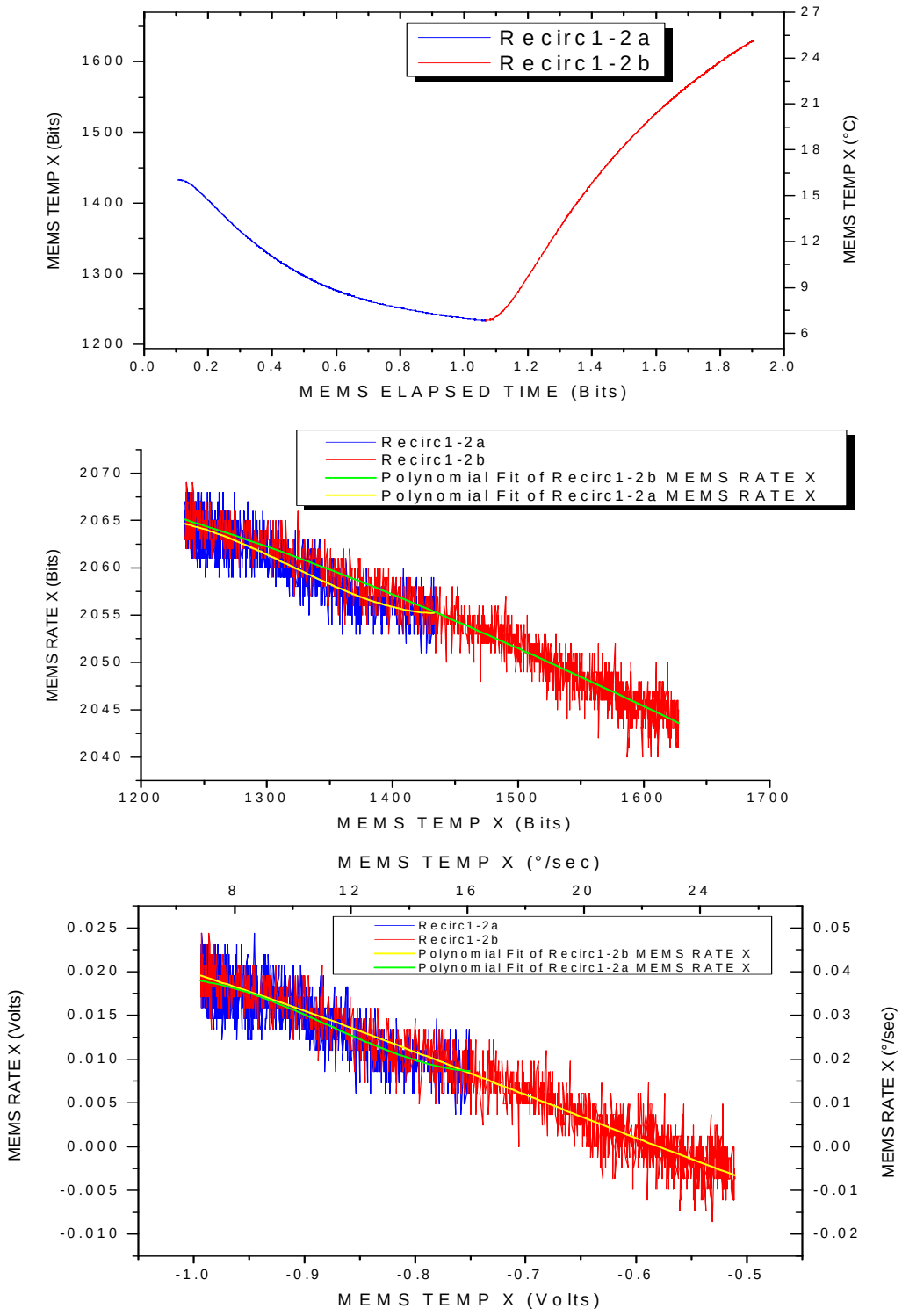

Appendix Figure 7. Hysteresis Test, Recirc1–2 (X)

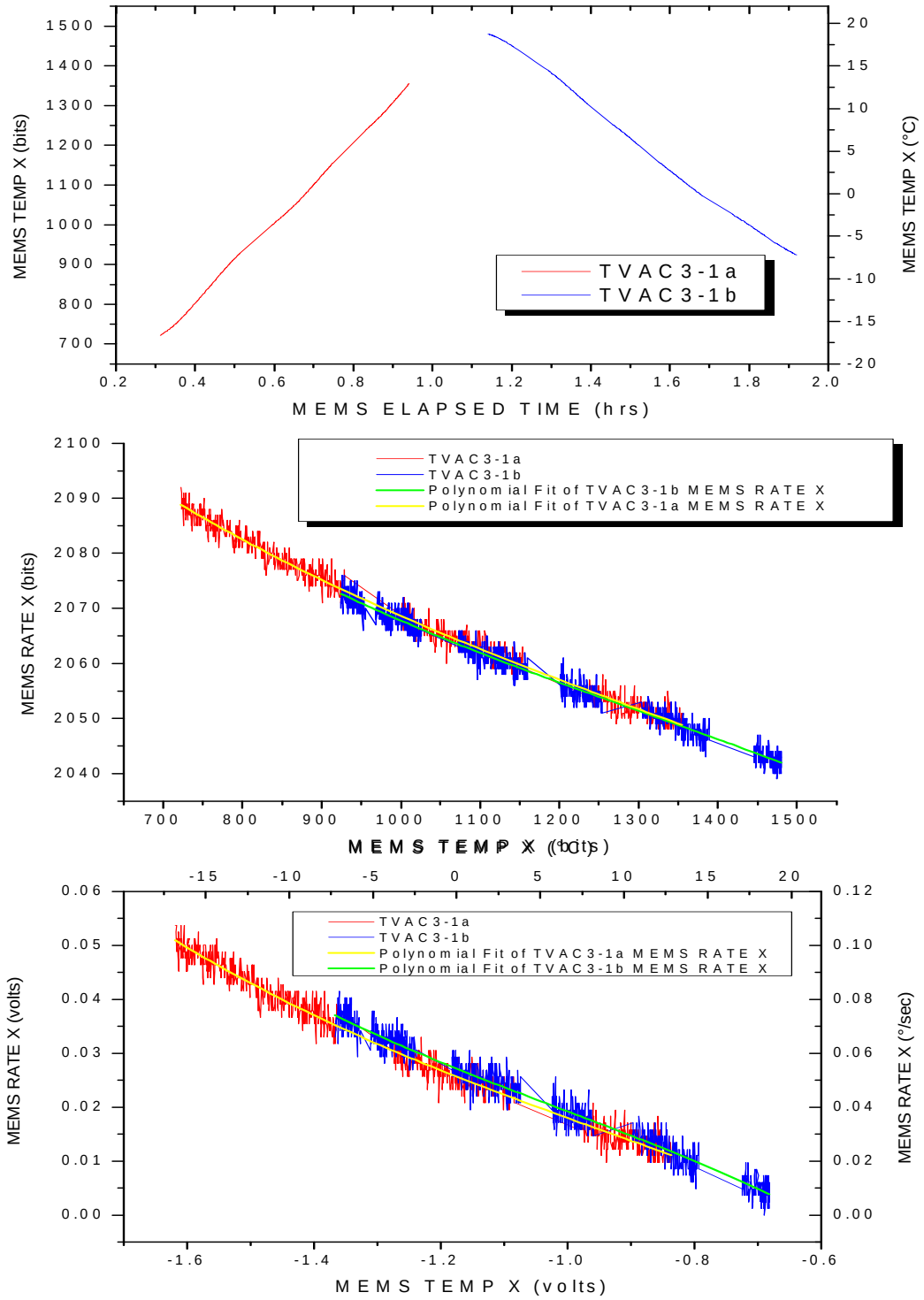

Appendix Figure 8. Hysteresis Test, TVAC2–1 (X)

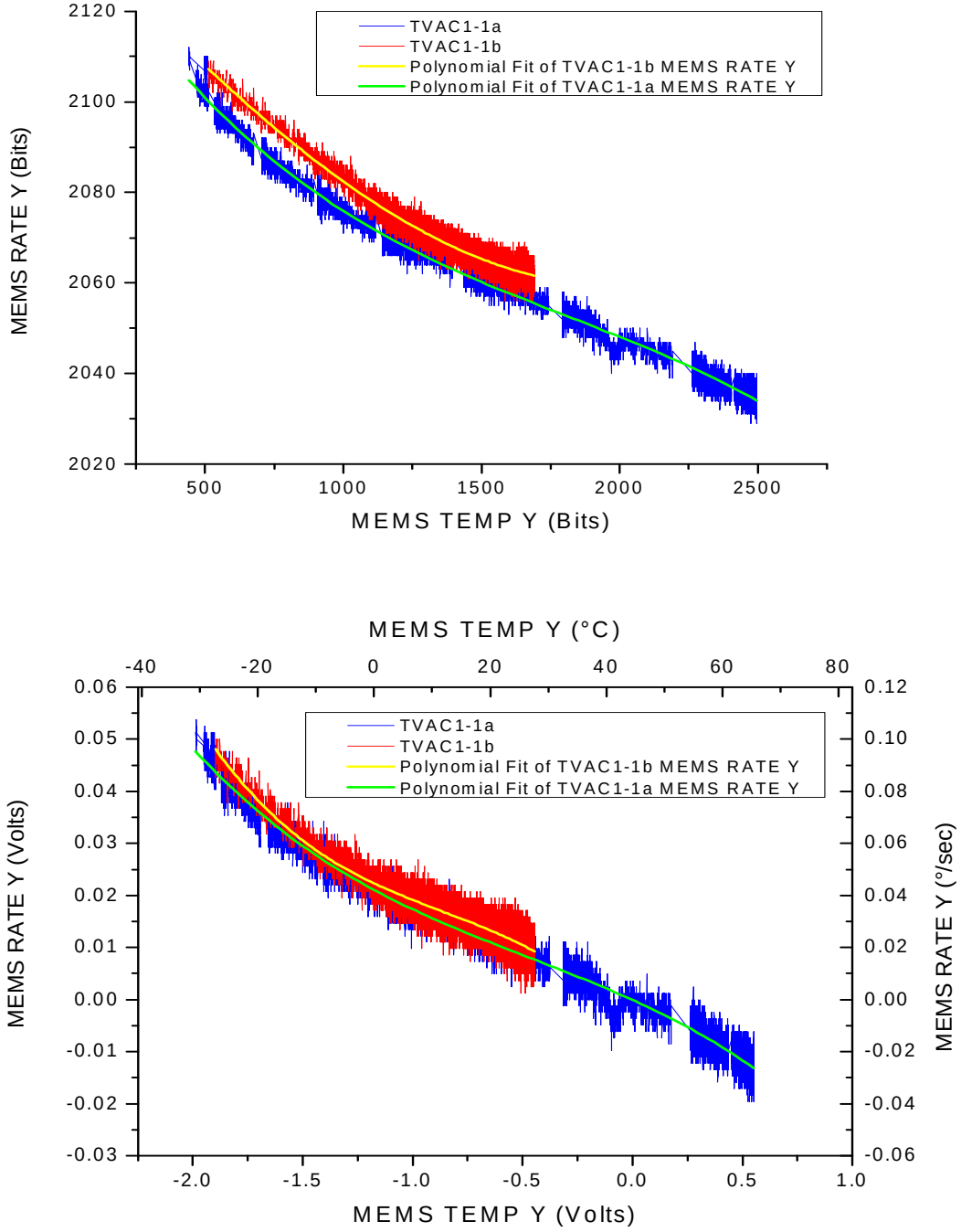

Appendix Figure 9. Hysteresis Test, TVAC1–1 (X)

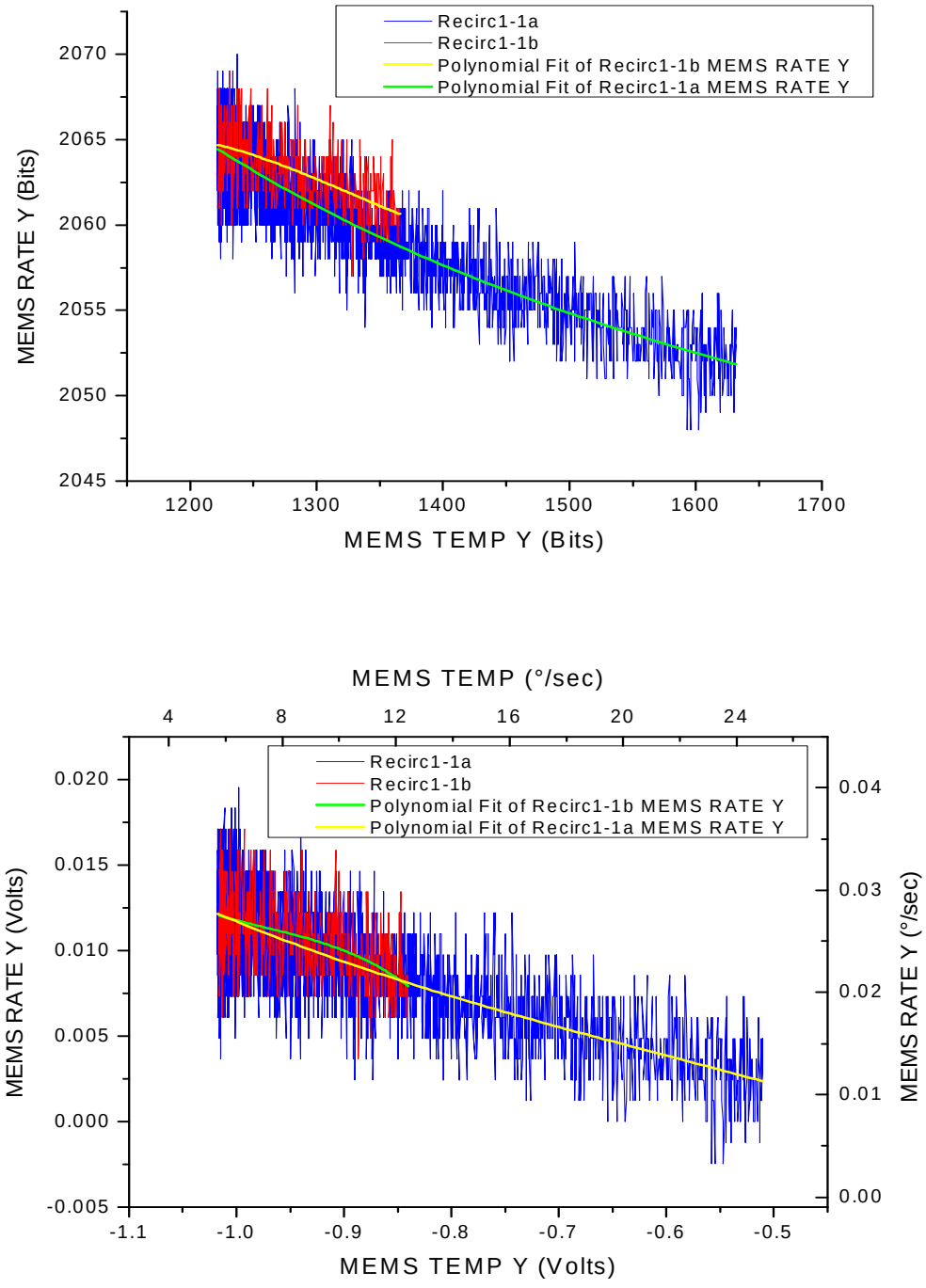

Appendix Figure 10. Hysteresis Test, Recirc1–1 (Y)

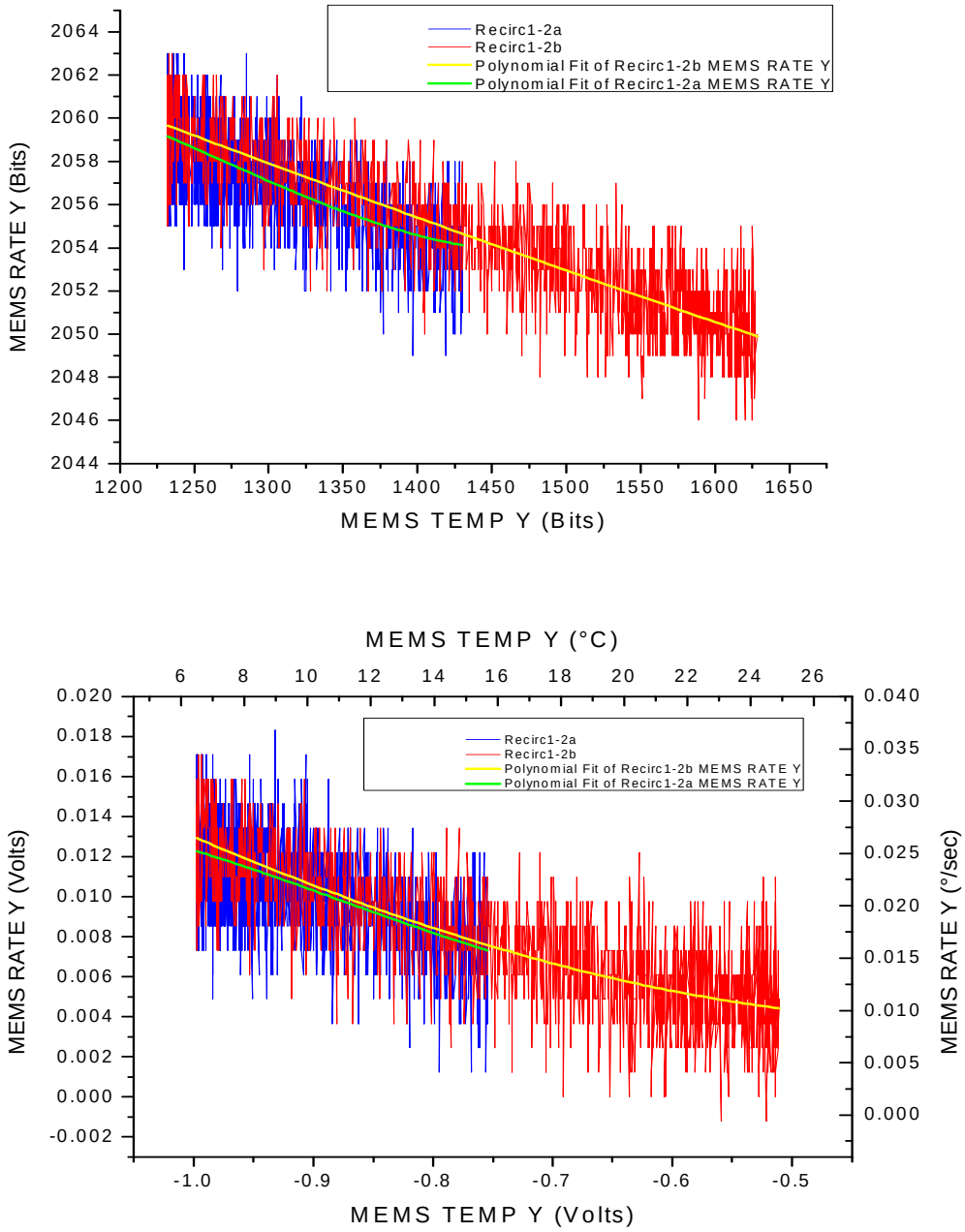

Appendix Figure 11. Hysteresis Test, Recirc1–2 (Y)

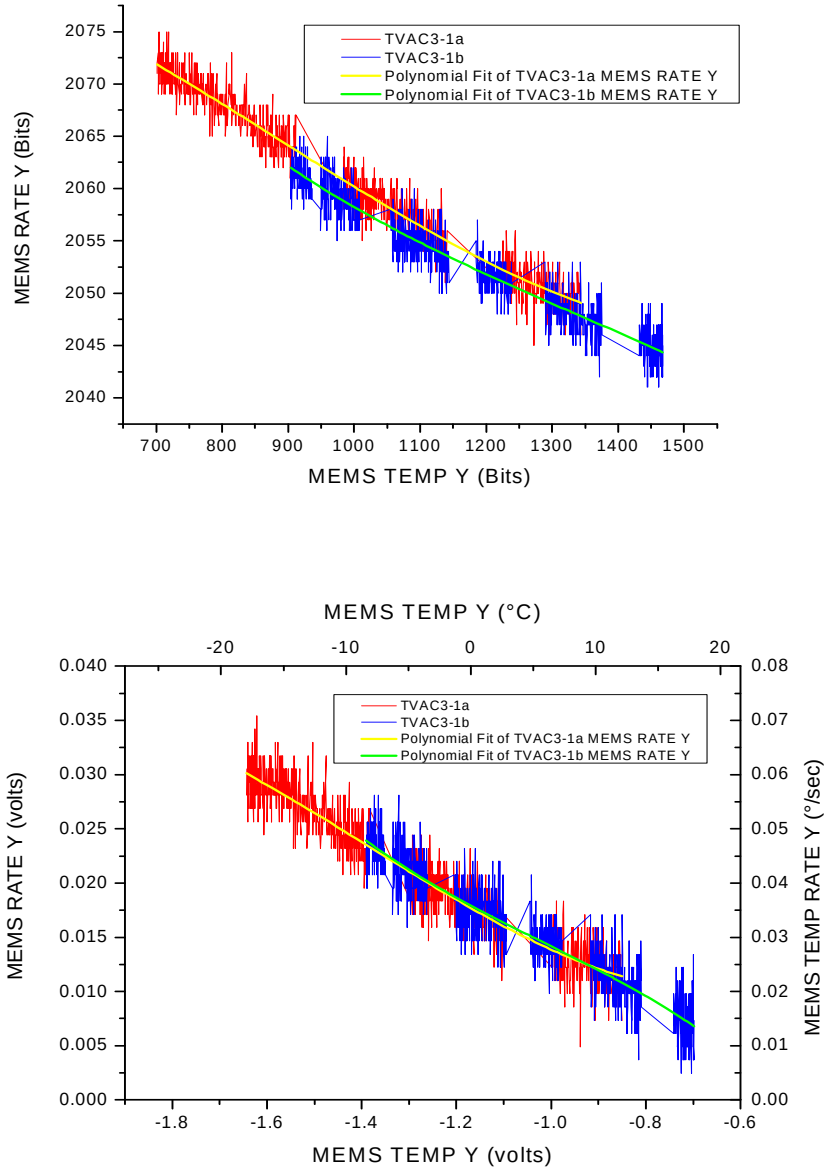

Appendix Figure 12. Hysteresis Test, TVAC2–1 (Y)

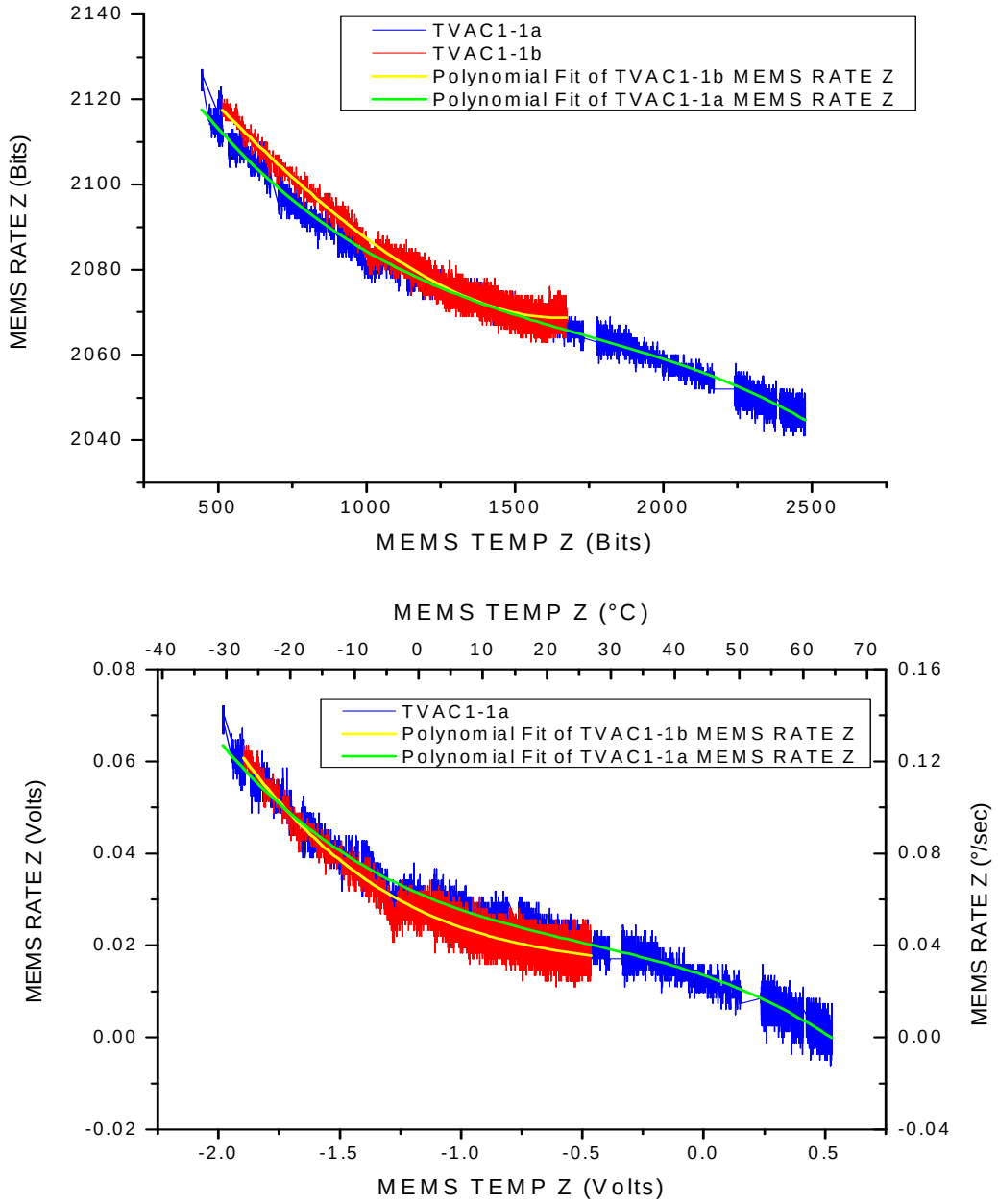

Appendix Figure 13. Hysteresis Test, TVAC1–1 (Z)

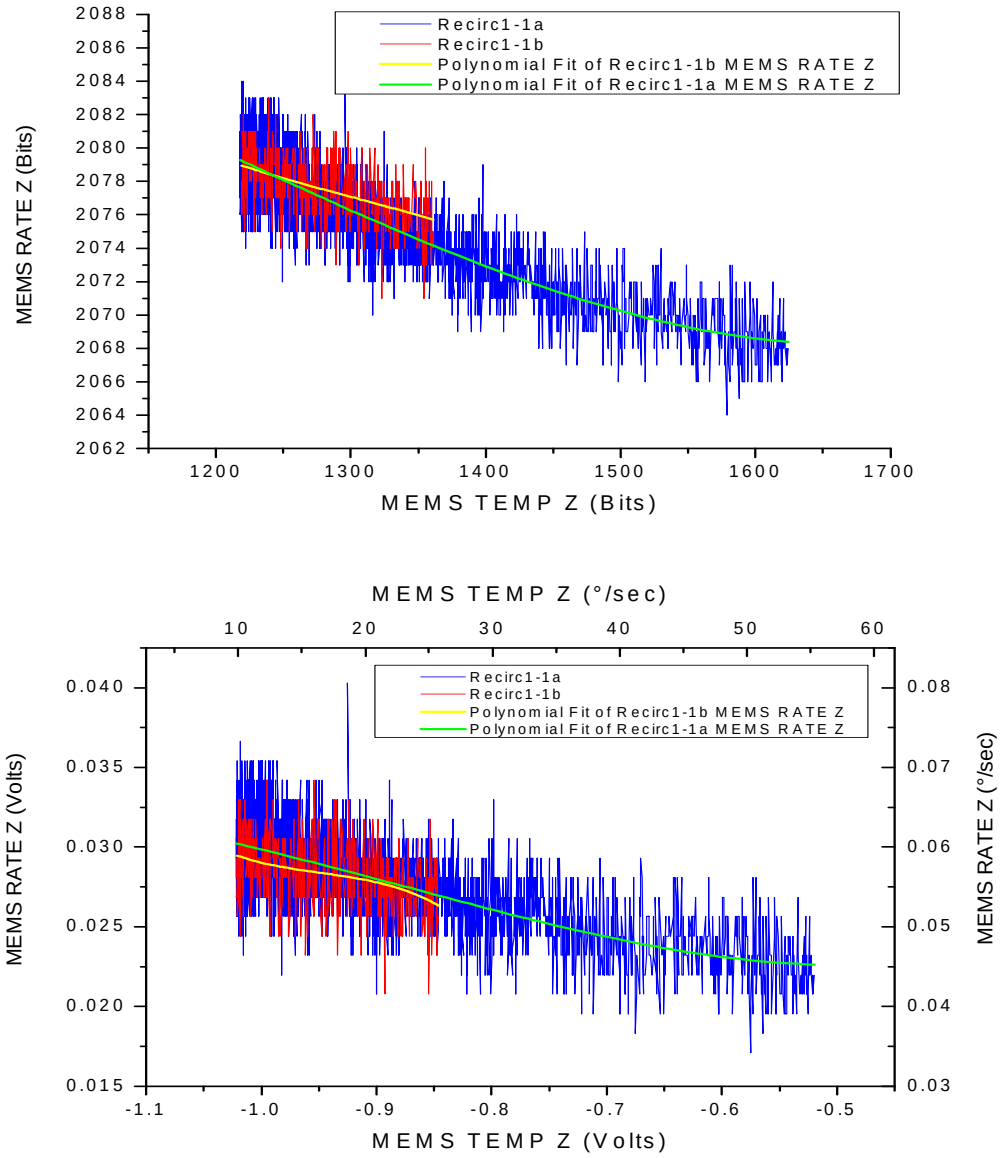

Appendix Figure 14. Hysteresis Test, Recirc1–1 (Z)

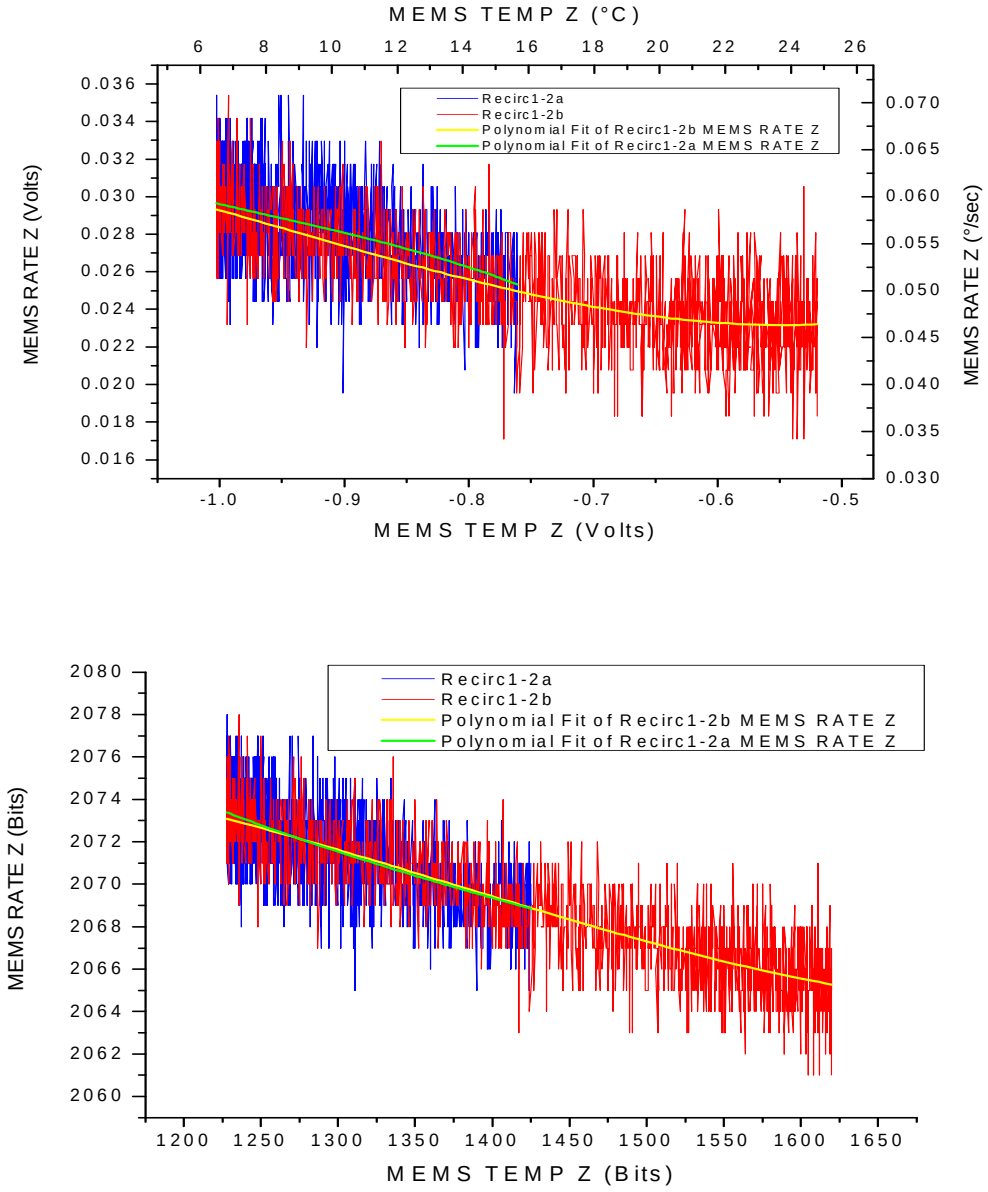

Appendix Figure 15. Hysteresis Test, Recirc1–2 (Z)

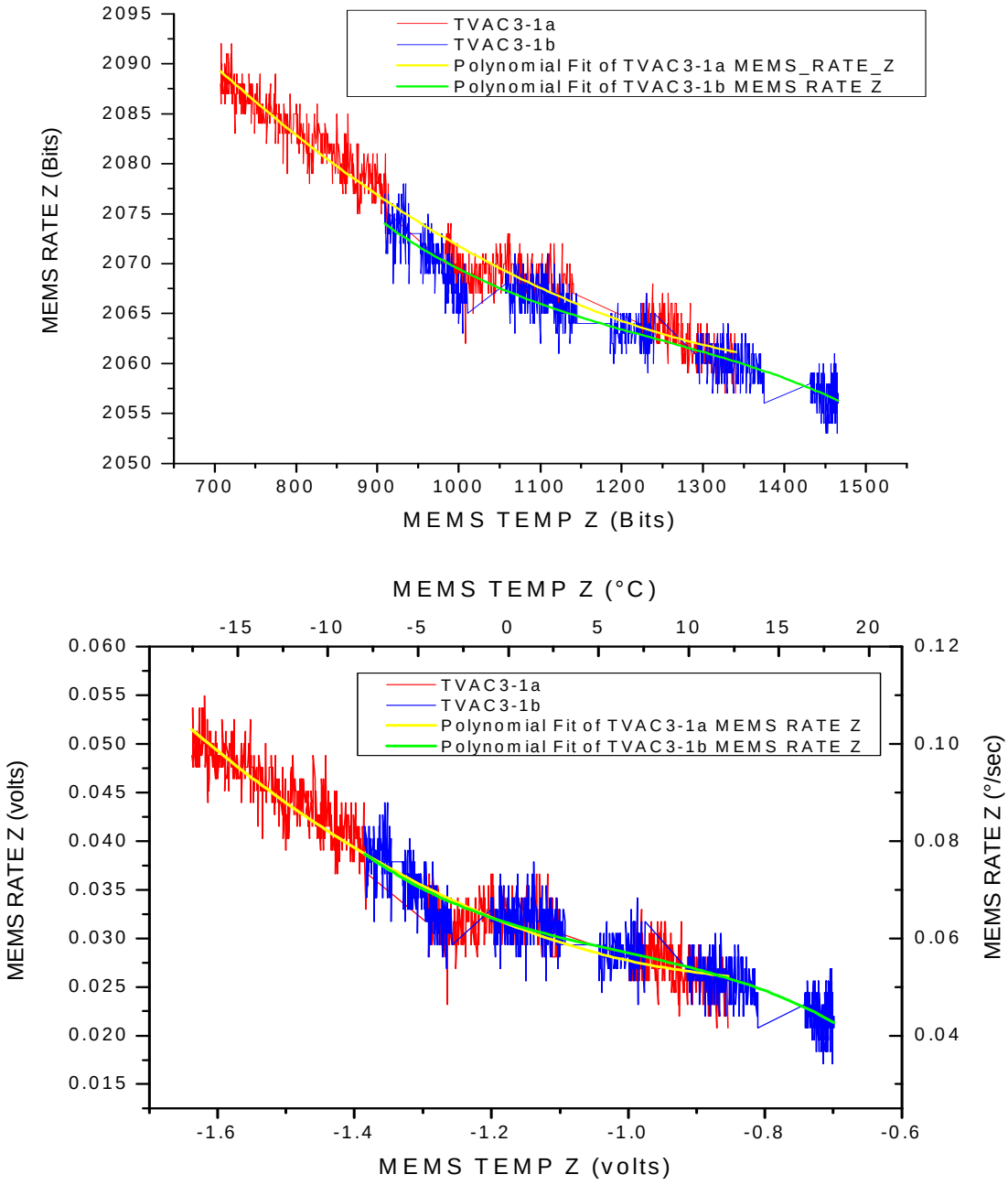

Appendix Figure 16. Hysteresis Test, TVAC3–1 (Z)

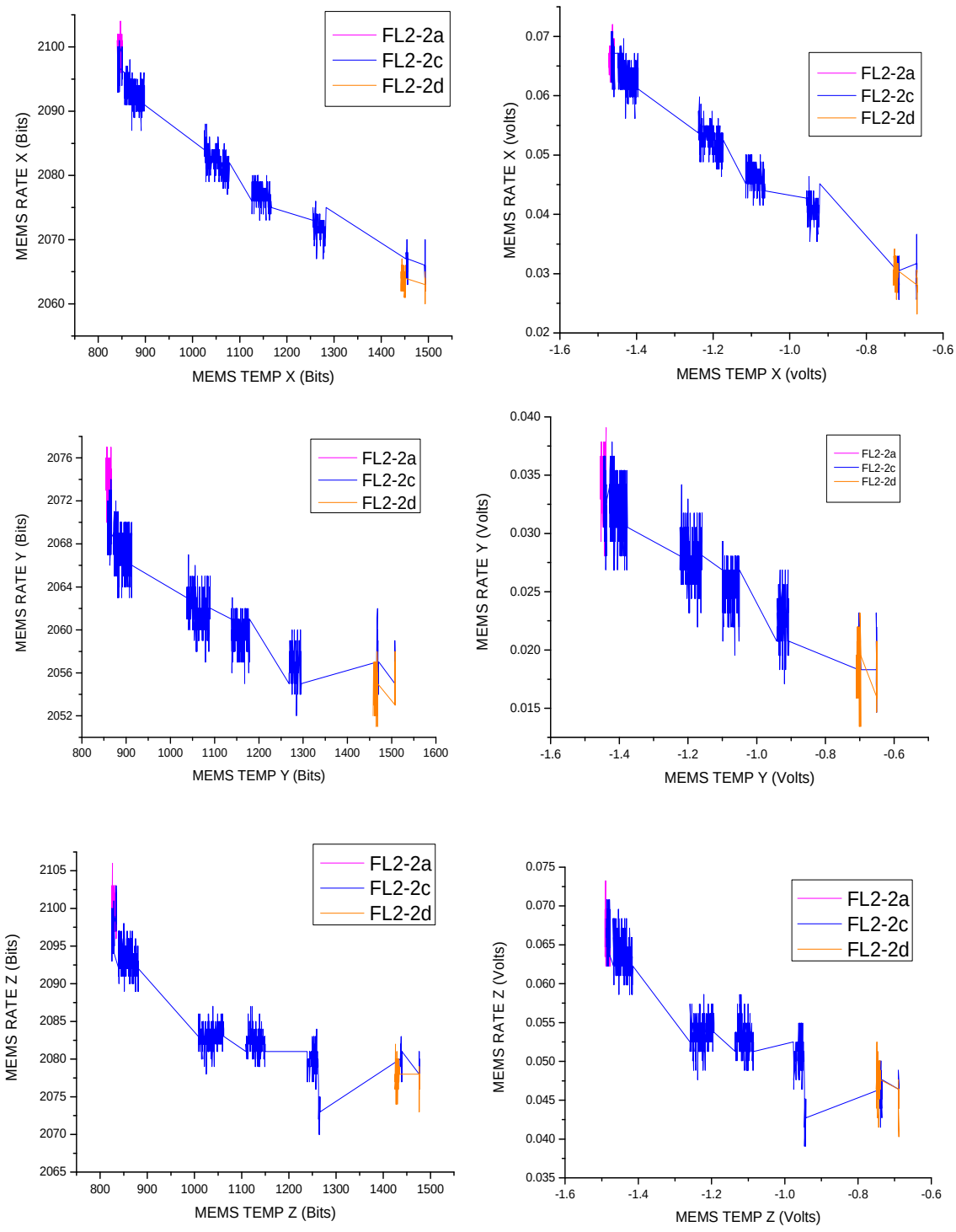

Appendix Figure 17. Hysteresis Test, FL2–1 (X,Y,Z)

Appendix Table 3. Hysteresis Summary

Test ID	Raw A/D-Bit			Converted		
	X	Y	Z	X	Y	Z
TVAC1–1a&b	unclear	yes	unclear	no	no	unclear
Recirc1–1a&b	no	no	no	no	yes	no
Recirc1–2a&b	no	no	no	no	yes	no
Recirc2–1a,b,&c	no	yes	yes	yes	no	yes
TVAC3–1a&b	no	unclear	unclear	yes	no	no

E1. S_{FX} RESULTS

Linear Fit (4/5/2011 12:10:08)

Input Data

	Input X Data Source	Input Y Data Source	Range
Sample Set 1	[Book2]Main!Test Rate	[Book2]Main!Sample Set 1	[1":62"]
Sample Set 2	[Book2]Main!Test Rate	[Book2]Main!Sample Set 2	[1":56"]

Masked Data - Values Excluded from Computations

Notes
No Masked Data

Parameters

		Value	Standard Error
Concatenate	Intercept	-8.71157E-4	4.11762E-4
	Slope	0.49979	2.09496E-4

Some input data points are missing.

Statistics

	Concatenate
Number of Points	100
Degrees of Freedom	98
Residual Sum of Squares	0.00166
Pearson's r	0.99999
Adj. R-Square	0.99998

Summary

	Intercept		Slope		Statistics
	Value	Standard Error	Value	Standard Error	Adj. R-Square
Concatenate	-8.71157E-4	4.11762E-4	0.49979	2.09496E-4	0.99998

ANOVA

		DF	Sum of Squares	Mean Square	F Value	Prob>F
Concatenate	Model	1	96.49673	96.49673	5.69142E6	0
	Error	98	0.00166	1.69548E-5		
	Total	99	96.49839			

Fitted Curves Plot

Concatenate

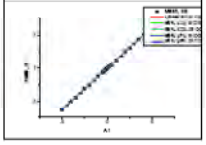

Residual vs. Independent Plot

Concatenate

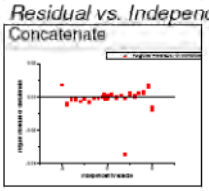

Residual vs. Predicted Values Plot

Concatenate

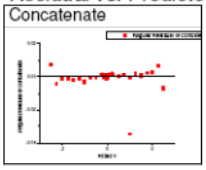

Appendix Figure 18. S_{fx} Results

E2. M_{XY} RESULTS

Linear Fit (4/5/2011 12:07:34)

Input Data

	Input X Data Source	Input Y Data Source	Range
Y Sample Set 1	[Book2]Y!X Test Rate	[Book2]Y!Y Sample Set 1	[1*:62*]
Y Sample Set 2	[Book2]Y!X Test Rate	[Book2]Y!Y Sample Set 2	[1*:56*]

Masked Data - Values Excluded from Computations

Notes
No Masked Data

Parameters

		Value	Standard Error
Concatenate	Intercept	-9.82628E-4	3.19189E-4
	Slope	5.08297E-4	1.39211E-4

Some input data points are missing.

Statistics

	Concatenate
Number of Points	24
Degrees of Freedom	22
Residual Sum of Squares	5.37935E-5
Pearson's r	0.61427
Adj. R-Square	0.34903

Summary

	Intercept		Slope		Statistics
	Value	Standard Error	Value	Standard Error	Adj. R-Square
Concatenate	-9.82628E-4	3.19189E-4	5.08297E-4	1.39211E-4	0.34903

ANOVA

		DF	Sum of Squares	Mean Square	F Value	Prob>F
Concatenate	Model	1	3.25984E-5	3.25984E-5	13.33183	0.00141
	Error	22	5.37935E-5	2.44516E-6		
	Total	23	8.63919E-5			

Fitted Curves Plot

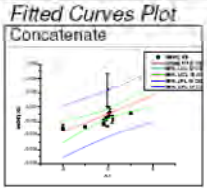

Residual vs. Independent Plot

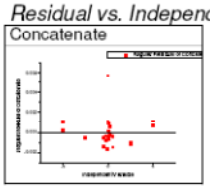

Residual vs. Predicted Values Plot

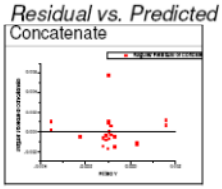

Appendix Figure 19. M_{xy} Results

E3. M_{XZ} RESULTS

Linear Fit (4/5/2011 12:05:33)

Input Data

	Input X Data Source	Input Y Data Source	Range
Z Sample Set 1	[Book2]Z!X Test Rate	[Book2]Z!Z Sample Set 1	[1":62"]
Z Sample Set 2	[Book2]Z!X Test Rate	[Book2]Z!Z Sample Set 2	[1":56"]

Masked Data - Values Excluded from Computations

Notes
No Masked Data

Parameters

		Value	Standard Error
Concatenate	Intercept	1.09605E-4	4.52441E-4
	Slope	0.00649	1.97327E-4

Some input data points are missing.

Statistics

	Concatenate
Number of Points	24
Degrees of Freedom	22
Residual Sum of Squares	1.08083E-4
Pearson's r	0.98998
Adj. R-Square	0.97915

Summary

	Intercept		Slope		Statistics
	Value	Standard Error	Value	Standard Error	Adj. R-Square
Concatenate	1.09605E-4	4.52441E-4	0.00649	1.97327E-4	0.97915

ANOVA

		DF	Sum of Squares	Mean Square	F Value	Prob>F
Concatenate	Model	1	0.00531	0.00531	1080.99414	0
	Error	22	1.08083E-4	4.91286E-6		
	Total	23	0.00542			

Fitted Curves Plot

Concatenate

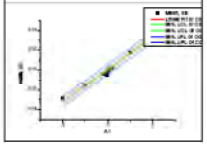

Residual vs. Independent Plot

Concatenate

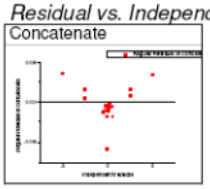

Residual vs. Predicted Values Plot

Concatenate

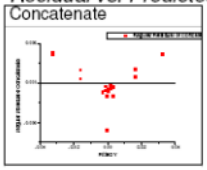

Appendix Figure 20. M_{xz} Results

F1. S_{FY} RESULTS

Linear Fit (4/5/2011 17:42:26)

Input Data

	Input X Data Source	Input Y Data Source	Range
Sample Set 1	[Book2]Main!Y Test Rate	[Book2]Main!Sample Set 1	[1":64"]
Sample Set 2	[Book2]Main!Y Test Rate	[Book2]Main!Sample Set 2	[1":64"]

Parameters

		Value	Standard Error
Concatenate	Intercept	-0.00117	3.38879E-4
	Slope	0.502	1.48321E-4

Some input data points are missing.

Statistics

	Concatenate
Number of Points	74
Degrees of Freedom	72
Residual Sum of Squares	6.11862E-4
Pearson's r	1
Adj. R-Square	0.99999

Summary

	Intercept		Slope		Statistics
	Value	Standard Error	Value	Standard Error	Adj. R-Square
Concatenate	-0.00117	3.38879E-4	0.502	1.48321E-4	0.99999

ANOVA

		DF	Sum of Squares	Mean Square	F Value	Prob>F
Concatenate	Model	1	97.34717	97.34717	1.14552E7	0
	Error	72	6.11862E-4	8.49808E-6		
	Total	73	97.34778			

Fitted Curves Plot

Concatenate

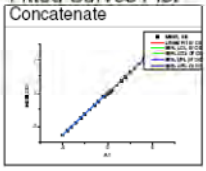

Residual vs. Independent Plot

Concatenate

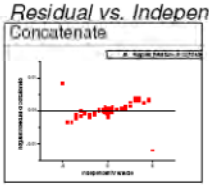

Residual vs. Predicted Values Plot

Concatenate

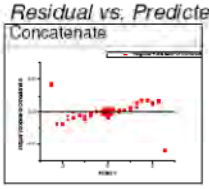

Appendix Figure 21. S_{fy} Results

F2. M_{YX} RESULTS

Linear Fit (4/5/2011 16:01:59)

Input Data

	Input X Data Source	Input Y Data Source	Range
Sample Set 1	[Book2]X!Y Test Rate	[Book2]X!Sample Set 1	[1*:64*]
Sample Set 2	[Book2]X!Y Test Rate	[Book2]X!Sample Set 2	[1*:64*]

Parameters

		Value	Standard Error
Concatenate	Intercept	0.00139	6.26923E-4
	Slope	-0.00115	2.49599E-4

Some input data points are missing.

Statistics

	Concatenate
Number of Points	20
Degrees of Freedom	18
Residual Sum of Squares	1.41492E-4
Pearson's r	-0.73498
Adj. R-Square	0.51464

Summary

	Intercept		Slope		Statistics
	Value	Standard Error	Value	Standard Error	Adj. R-Square
Concatenate	0.00139	6.26923E-4	-0.00115	2.49599E-4	0.51464

ANOVA

		DF	Sum of Squares	Mean Square	F Value	Prob>F
Concatenate	Model	1	1.66225E-4	1.66225E-4	21.14648	2.22968E-4
	Error	18	1.41492E-4	7.86064E-6		
	Total	19	3.07716E-4			

Fitted Curves Plot

Concatenate

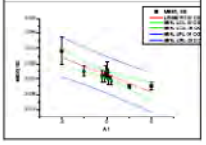

Residual vs. Independent Plot

Concatenate

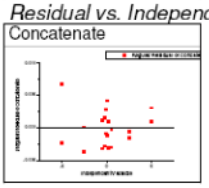

Residual vs. Predicted Values Plot

Concatenate

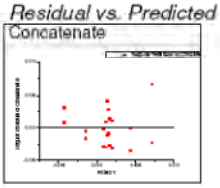

Appendix Figure 22. M_{yx} Results

F3. M_{YZ} RESULTS

Linear Fit (4/5/2011 16:05:10)

Input Data

	Input X Data Source	Input Y Data Source	Range
Sample Set 1	[Book2]Z!Y Test Rate	[Book2]Z!Sample Set 1	[1*:64*]
Sample Set 2	[Book2]Z!Y Test Rate	[Book2]Z!Sample Set 2	[1*:64*]

Parameters

		Value	Standard Error
Concatenate	Intercept	-1.15325E-6	3.19233E-4
	Slope	6.37976E-4	1.27098E-4

Some input data points are missing.

Statistics

	Concatenate
Number of Points	20
Degrees of Freedom	18
Residual Sum of Squares	3.66875E-5
Pearson's r	0.76374
Adj. R-Square	0.56015

Summary

	Intercept		Slope		Statistics
	Value	Standard Error	Value	Standard Error	Adj. R-Square
Concatenate	-1.15325E-6	3.19233E-4	6.37976E-4	1.27098E-4	0.56015

ANOVA

		DF	Sum of Squares	Mean Square	F Value	Prob>F
Concatenate	Model	1	5.13546E-5	5.13546E-5	25.19613	8.89921E-5
	Error	18	3.66875E-5	2.03819E-6		
	Total	19	8.80421E-5			

Fitted Curves Plot

Concatenate

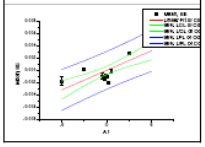

Residual vs. Independent Plot

Concatenate

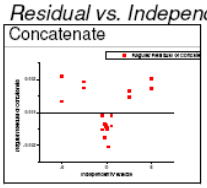

Residual vs. Predicted Values Plot

Concatenate

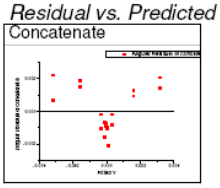

Appendix Figure 23. M_{yz} Results

G1. S_{FZ} RESULTS

Linear Fit (4/5/2011 16:14:54)

Parameters

		Value	Standard Error
Concatenate	Intercept	-3.2618E-4	2.75604E-4
	Slope	0.49747	1.50704E-4

Some input data points are missing.

Statistics

	Concatenate
Number of Points	116
Degrees of Freedom	114
Residual Sum of Squares	0.001
Pearson's r	0.99999
Adj. R-Square	0.99999

Summary

	Intercept		Slope		Statistics
	Value	Standard Error	Value	Standard Error	Adj. R-Square
Concatenate	-3.2618E-4	2.75604E-4	0.49747	1.50704E-4	0.99999

ANOVA

		DF	Sum of Squares	Mean Square	F Value	Prob>F
Concatenate	Model	1	96.01108	96.01108	1.08966E7	0
	Error	114	0.001	8.81108E-6		
	Total	115	96.01208			

Fitted Curves Plot

Concatenate

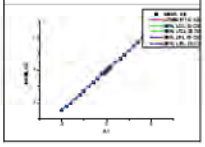

Residual vs. Independent Plot

Concatenate

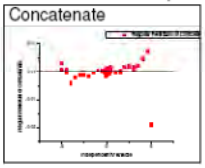

Residual vs. Predicted Values Plot

Concatenate

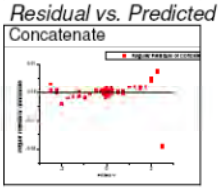

Appendix Figure 24. S_{fz} Results

G2. M_{ZX} RESULTS

Linear Fit (4/5/2011 16:19:08)

Parameters

		Value	Standard Error
Concatenate	Intercept	0.00122	2.98866E-4
	Slope	-0.001	1.18949E-4

Some input data points are missing.

Statistics

	Concatenate
Number of Points	20
Degrees of Freedom	18
Residual Sum of Squares	3.21556E-5
Pearson's r	-0.89341
Adj. R-Square	0.78697

Summary

	Intercept		Slope		Statistics
	Value	Standard Error	Value	Standard Error	Adj. R-Square
Concatenate	0.00122	2.98866E-4	-0.001	1.18949E-4	0.78697

ANOVA

		DF	Sum of Squares	Mean Square	F Value	Prob>F
Concatenate	Model	1	1.27171E-4	1.27171E-4	71.18763	1.13918E-7
	Error	18	3.21556E-5	1.78642E-6		
	Total	19	1.59327E-4			

Fitted Curves Plot

Concatenate

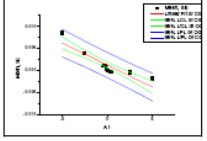

Residual vs. Independent Plot

Concatenate

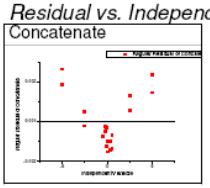

Residual vs. Predicted Values Plot

Concatenate

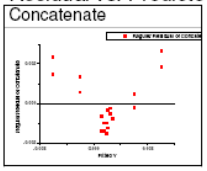

Appendix Figure 25. M_{zx} Results

G3. M_{ZY} RESULTS

Linear Fit (4/5/2011 16:21:09)

Input Data

	Input X Data Source	Input Y Data Source	Range
Y Sample Set 1 minus offset	[Book3]Y!Z Test Rate	[Book3]Y!Y Sample Set 1 minus offs	[1*:62*]
Y Sample Set 2 minus offset	[Book3]Y!Z Test Rate	[Book3]Y!Y Sample Set 2 minus offs	[1*:62*]

Parameters

		Value	Standard Error
Concatenate	Intercept	0.00111	1.98666E-4
	Slope	-6.93375E-4	7.90687E-5

Some input data points are missing.

Statistics

	Concatenate
Number of Points	20
Degrees of Freedom	18
Residual Sum of Squares	1.42085E-5
Pearson's r	-0.90018
Adj. R-Square	0.79979

Summary

	Intercept		Slope		Statistics
	Value	Standard Error	Value	Standard Error	Adj. R-Square
Concatenate	0.00111	1.98666E-4	-6.93375E-4	7.90687E-5	0.79979

ANOVA

		DF	Sum of Squares	Mean Square	F Value	Prob>F
Concatenate	Model	1	6.07019E-5	6.07019E-5	76.90018	6.47199E-8
	Error	18	1.42085E-5	7.8936E-7		
	Total	19	7.49104E-5			

Fitted Curves Plot

Concatenate

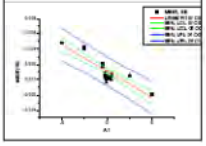

Residual vs. Independent Plot

Concatenate

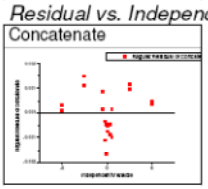

Residual vs. Predicted Values Plot

Concatenate

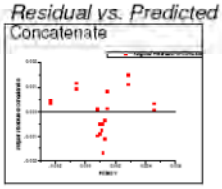

Appendix Figure 26. M_{zy} Results

H1. S_{FX} RESULTS (NO REF)

Linear Fit (4/6/2011 15:59:31)

Parameters

		Value	Standard Error
Concatenate	Intercept	0.00359	3.89144E-4
	Slope	0.49979	1.99959E-4

Some input data points are missing.

Statistics

	Concatenate
Number of Points	102
Degrees of Freedom	100
Residual Sum of Squares	0.00154
Pearson's r	0.99999
Adj. R-Square	0.99998

Summary

	Intercept		Slope		Statistics
	Value	Standard Error	Value	Standard Error	Adj. R-Square
Concatenate	0.00359	3.89144E-4	0.49979	1.99959E-4	0.99998

ANOVA

		DF	Sum of Squares	Mean Square	F Value	Prob>F
Concatenate	Model	1	96.49676	96.49676	6.24729E6	0
	Error	100	0.00154	1.54462E-5		
	Total	101	96.4983			

Fitted Curves Plot

Concatenate

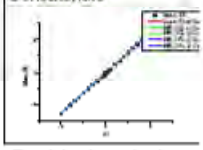

Residual vs. Independent Plot

Concatenate

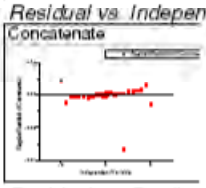

Residual vs. Predicted Values Plot

Concatenate

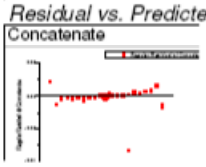

Appendix Figure 27. S_{fx} Results (No Ref)

H2. M_{XY} RESULTS (NO REF)

Linear Fit (4/6/2011 16:00:17)

Parameters

		Value	Standard Error
Concatenate	Intercept	-0.00372	2.73816E-4
	Slope	5.08297E-4	1.19422E-4

Some input data points are missing.

Statistics

	Concatenate
Number of Points	24
Degrees of Freedom	22
Residual Sum of Squares	3.95868E-5
Pearson's r	0.67201
Adj. R-Square	0.42667

Summary

	Intercept		Slope		Statistics
	Value	Standard Error	Value	Standard Error	Adj. R-Square
Concatenate	-0.00372	2.73816E-4	5.08297E-4	1.19422E-4	0.42667

ANOVA

		DF	Sum of Squares	Mean Square	F Value	Prob>F
Concatenate	Model	1	3.25984E-5	3.25984E-5	18.11627	3.22609E-4
	Error	22	3.95868E-5	1.7994E-6		
	Total	23	7.21853E-5			

Fitted Curves Plot

Concatenate

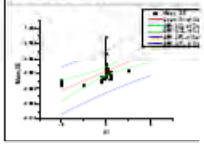

Residual vs. Independent Plot

Concatenate

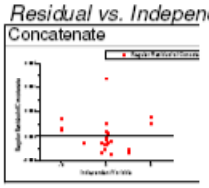

Residual vs. Predicted Values Plot

Concatenate

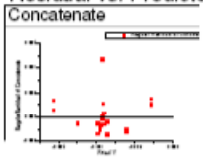

Appendix Figure 28. M_{xy} Results (No Ref)

H3. M_{XZ} RESULTS (NO REF)

Linear Fit (4/6/2011 16:02:19)

Parameters

		Value	Standard Error
Concatenate	Intercept	0.00107	3.66182E-4
	Slope	0.00649	1.59706E-4

Some input data points are missing.

Statistics

	Concatenate
Number of Points	24
Degrees of Freedom	22
Residual Sum of Squares	7.07992E-5
Pearson's r	0.9934
Adj. R-Square	0.98625

Summary

	Intercept		Slope		Statistics
	Value	Standard Error	Value	Standard Error	Adj. R-Square
Concatenate	0.00107	3.66182E-4	0.00649	1.59706E-4	0.98625

ANOVA

		DF	Sum of Squares	Mean Square	F Value	Prob>F
Concatenate	Model	1	0.00531	0.00531	1650.25744	0
	Error	22	7.07992E-5	3.21815E-6		
	Total	23	0.00538			

Fitted Curves Plot

Concatenate

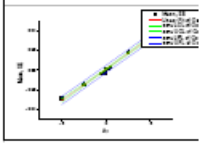

Residual vs. Independent Plot

Concatenate

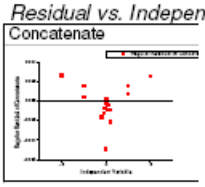

Residual vs. Predicted Values Plot

Concatenate

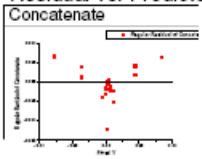

Appendix Figure 29. M_{xz} Results (No Ref)

I1. S_{FY} RESULTS (NO REF)

Linear Fit (4/6/2011 15:45:45)

Parameters

		Value	Standard Error
Concatenate	Intercept	-0.00406	3.33236E-4
	Slope	0.502	1.45851E-4

Some input data points are missing.

Statistics

	Concatenate
Number of Points	74
Degrees of Freedom	72
Residual Sum of Squares	5.91653E-4
Pearson's r	1
Adj. R-Square	0.99999

Summary

	Intercept		Slope		Statistics
	Value	Standard Error	Value	Standard Error	Adj. R-Square
Concatenate	-0.00406	3.33236E-4	0.502	1.45851E-4	0.99999

ANOVA

		DF	Sum of Squares	Mean Square	F Value	Prob>F
Concatenate	Model	1	97.34717	97.34717	1.18465E7	0
	Error	72	5.91653E-4	8.21741E-6		
	Total	73	97.34776			

Fitted Curves Plot

Concatenate

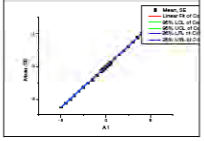

Residual vs. Independent Plot

Concatenate

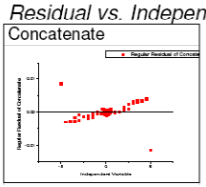

Residual vs. Predicted Values Plot

Concatenate

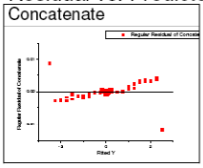

Appendix Figure 30. S_{fy} Results (No Ref)

I2. M_{YX} RESULTS (NO REF)

Linear Fit (4/6/2011 15:47:26)

Parameters

		Value	Standard Error
Concatenate	Intercept	0.00364	2.10087E-4
	Slope	-7.79646E-4	8.36426E-5

Some input data points are missing.

Statistics

	Concatenate
Number of Points	20
Degrees of Freedom	18
Residual Sum of Squares	1.58891E-5
Pearson's r	-0.91015
Adj. R-Square	0.81885

Summary

	Intercept		Slope		Statistics
	Value	Standard Error	Value	Standard Error	Adj. R-Square
Concatenate	0.00364	2.10087E-4	-7.79646E-4	8.36426E-5	0.81885

ANOVA

		DF	Sum of Squares	Mean Square	F Value	Prob>F
Concatenate	Model	1	7.66948E-5	7.66948E-5	86.88387	2.60516E-8
	Error	18	1.58891E-5	8.82727E-7		
	Total	19	9.25839E-5			

Fitted Curves Plot

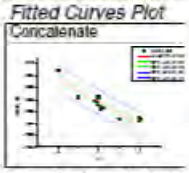

Residual vs. Independent Plot

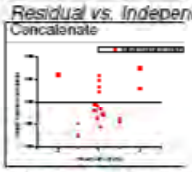

Residual vs. Predicted Values Plot

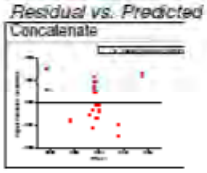

Appendix Figure 31. M_{yx} Results (No Ref)

I3. M_{YZ} RESULTS (NO REF)

Linear Fit (4/6/2011 15:49:03)

Parameters

		Value	Standard Error
Concatenate	Intercept	0.00222	4.40589E-4
	Slope	6.37976E-4	1.75414E-4

Some input data points are missing.

Statistics

	Concatenate
Number of Points	20
Degrees of Freedom	18
Residual Sum of Squares	6.98828E-5
Pearson's r	0.65084
Adj. R-Square	0.39156

Summary

	Intercept		Slope		Statistics
	Value	Standard Error	Value	Standard Error	Adj. R-Square
Concatenate	0.00222	4.40589E-4	6.37976E-4	1.75414E-4	0.39156

ANOVA

		DF	Sum of Squares	Mean Square	F Value	Prob>F
Concatenate	Model	1	5.13546E-5	5.13546E-5	13.22762	0.00189
	Error	18	6.98828E-5	3.88238E-6		
	Total	19	1.21237E-4			

Fitted Curves Plot

Concatenate

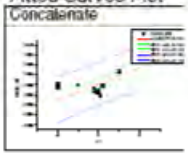

Residual vs. Independent Plot

Concatenate

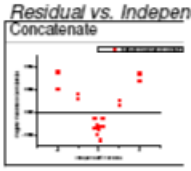

Residual vs. Predicted Values Plot

Concatenate

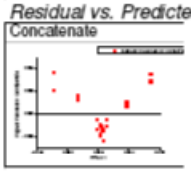

Appendix Figure 32. M_{yz} Results (No Ref)

J1 S_{FZ} RESULTS (NO REF)

Linear Fit (4/6/2011 15:02:03)

Parameters

		Value	Standard Error
Concatenate	Intercept	0.0035	2.53893E-4
	Slope	0.49747	1.38832E-4

An apparent fit is performed.
Some input data points are missing.

Statistics

	Concatenate
Number of Points	116
Degrees of Freedom	114
Residual Sum of Squares	8.52439E-4
Pearson's r	1
Adj. R-Square	0.99999

Summary

	Intercept		Slope		Statistics
	Value	Standard Error	Value	Standard Error	Adj. R-Square
Concatenate	0.0035	2.53893E-4	0.49747	1.38832E-4	0.99999

ANOVA

		DF	Sum of Squares	Mean Square	F Value	Prob>F
Concatenate	Model	1	96.01108	96.01108	1.28399E7	0
	Error	114	8.52439E-4	7.47753E-6		
	Total	115	96.01193			

Fitted Curves Plot

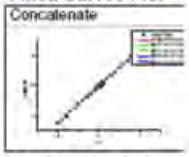

Residual vs. Independent Plot

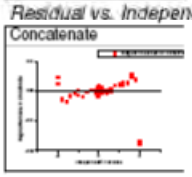

Residual vs. Predicted Values Plot

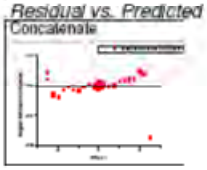

Appendix Figure 33. S_{fz} Results (No Ref)

J2. M_{ZX} RESULTS (NO REF)

Linear Fit (4/6/2011 15:20:35)

Parameters

		Value	Standard Error
Concatenate	Intercept	6.99876E-4	1.81121E-4
	Slope	-0.001	7.20861E-5

Some input data points are missing.

Statistics

	Concatenate
Number of Points	20
Degrees of Freedom	18
Residual Sum of Squares	1.18098E-5
Pearson's r	-0.95657
Adj. R-Square	0.91031

Summary

	Intercept		Slope		Statistics
	Value	Standard Error	Value	Standard Error	Adj. R-Square
Concatenate	6.99876E-4	1.81121E-4	-0.001	7.20861E-5	0.91031

ANOVA

		DF	Sum of Squares	Mean Square	F Value	Prob>F
Concatenate	Model	1	1.27171E-4	1.27171E-4	193.82923	4.45802E-11
	Error	18	1.18098E-5	6.56099E-7		
	Total	19	1.38981E-4			

Fitted Curves Plot

Concatenate

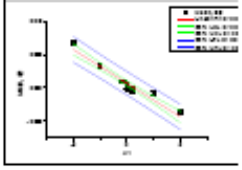

Residual vs. Independent Plot

Concatenate

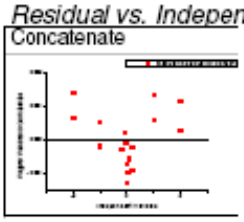

Residual vs. Predicted Values Plot

Concatenate

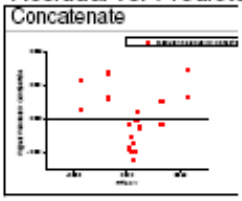

Appendix Figure 34. M_{zx} Results (No Ref)

J3. M_{ZY} RESULTS (NO REF)

Linear Fit (4/6/2011 15:23:17)

Parameters

		Value	Standard Error
Concatenate	Intercept	6.30512E-4	2.41177E-4
	Slope	-6.93375E-4	9.59884E-5

Some input data points are missing.

Statistics

	Concatenate
Number of Points	20
Degrees of Freedom	18
Residual Sum of Squares	2.09399E-5
Pearson's r	-0.86227
Adj. R-Square	0.72927

Summary

	Intercept		Slope		Statistics
	Value	Standard Error	Value	Standard Error	Adj. R-Square
Concatenate	6.30512E-4	2.41177E-4	-6.93375E-4	9.59884E-5	0.72927

ANOVA

		DF	Sum of Squares	Mean Square	F Value	Prob>F
Concatenate	Model	1	6.07019E-5	6.07019E-5	52.17945	1.01618E-6
	Error	18	2.09399E-5	1.16333E-6		
	Total	19	8.16419E-5			

Fitted Curves Plot

Concatenate

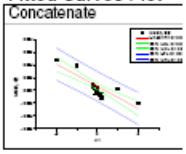

Residual vs. Independent Plot

Concatenate

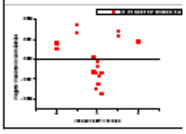

Residual vs. Predicted Values Plot

Concatenate

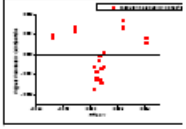

Appendix Figure 35. M_{zy} Results (No Ref)

K. ERROR OF CURVE FIT FOR MEMS ELASED TIME < 5 MINUTES

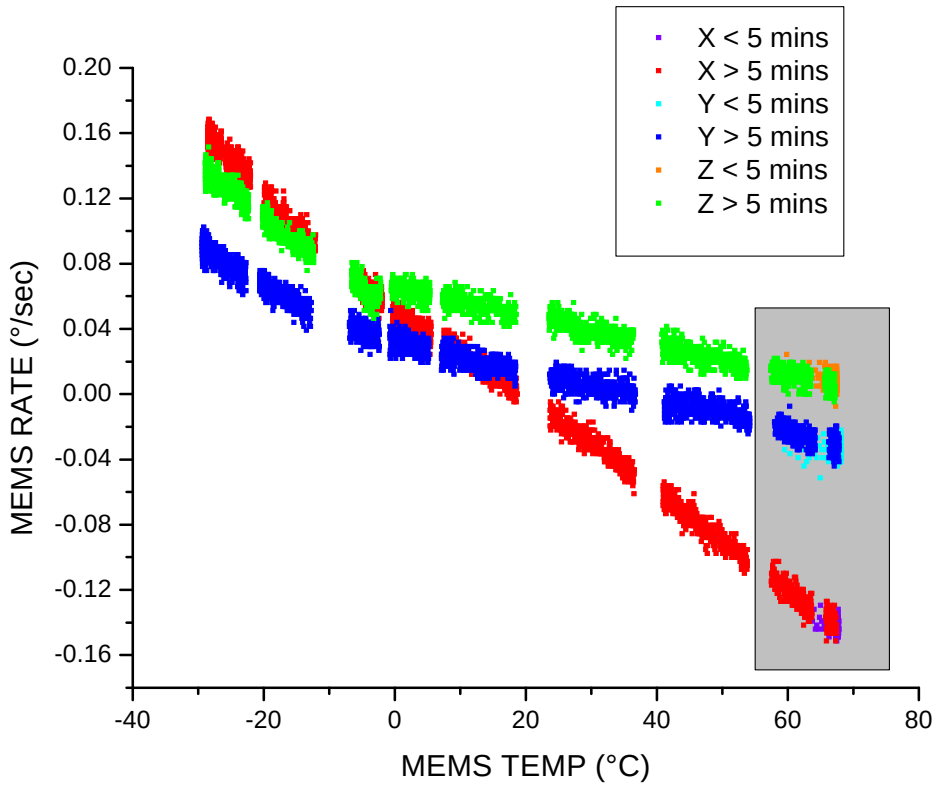

Appendix Figure 36. Ambient Pressure Thermal Ramp data with warm up data points

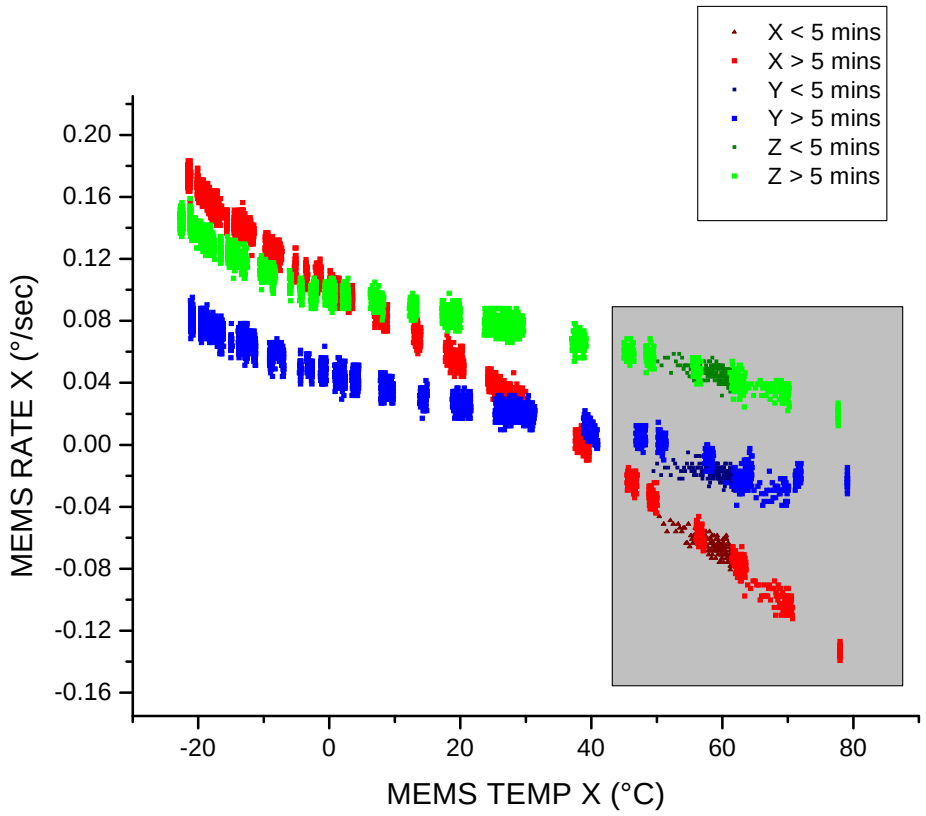

Appendix Figure 37. Vacuum Thermal Ramp data with warm up data points

L. EARTH RATE COMPONENT

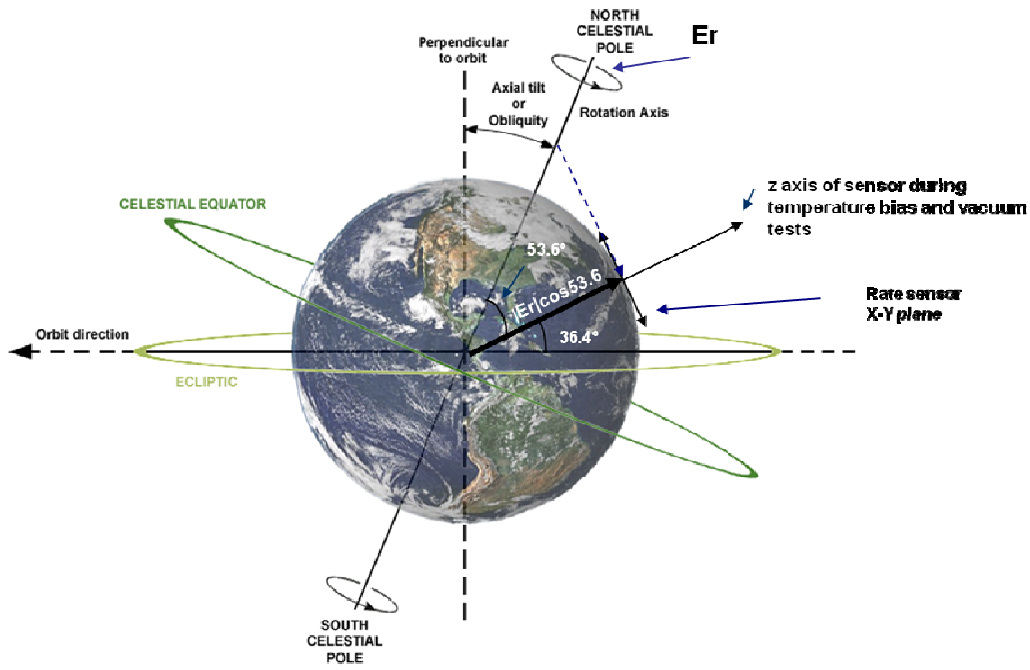

(a)

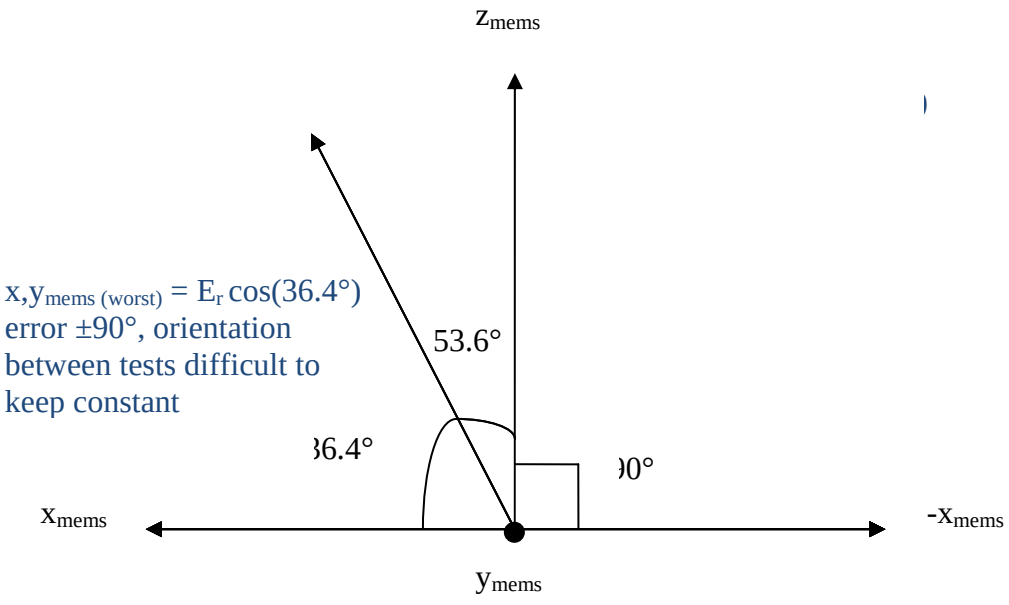

(b)

Appendix Figure 38. Earth Rate Component (a) Monterey, CA Angles (b) Worst Case Error Components

LIST OF REFERENCES

[1] S. Magnuson. (2010, July). "In orbit: Military looks to small satellites as costs for large spacecraft grow," *National Defense*, pp. 37–39.

[2] T. Pugsley, "Characterization, optimization, and test for the NPSAT1 MEMS 3-axis rate sensor suite for use in small satellite attitude control," Master's thesis, Naval Postgraduate School, Monterey, CA, 2007.

[3] C. Chi, Y. Peng and T. Chen, "Compensation of interface circuit errors for MEMS gyroscopes using state observers," in *Sensing Technology, 2008. ICST 2008 3rd International Conference on*, 2008, pp. 25–30.

[4] D. Sakoda and J.A. Horning, "Overview of the NPS Spacecraft Architecture and Technology Demonstration Satellite, NPSAT1," in *16th Annual AIAA/USU Conference on Small Satellites*, Logan, UT.

[5] M. Zager, "ACS algorithm verification using flight hardware," unpublished.

[6] E.W. Herbert, "NPSAT1 magnetic attitude control system algorithm verification, validation, and air-bearing tests," Master's thesis, Naval Postgraduate School, Monterey, CA, 2004.

[7] B. Leonard, "NPSAT1 Magnetic attitude control system," in *16th Annual AIAA/USU Conference on Small Satellites*, Logan, UT.

[8] D. Sakoda, "NPSAT1 Engineering Development Unit (EDU) Test Plan," Rep. Document Number: NPS-0001–0120, 2005.

[9] *General Environmental Verification Standard (GEVS) for GSFC Flight Programs and Projects*, NASA GSFC-STD-7000, April 2005.

[10] B. Start, "MEMS Reliability Assurance Guidelines for Space Applications," Pasadena, CA, Rep. JPL Publication 99–1, 1999.

[11] A. Cropp, C. Collingwood and S. Dussy, "The characterisation and testing of MEMS gyros for GIOVE-A," in *AIAA Guidance, Navigation, and Control Conference and Exhibit*, Keystone, Colorado, 2006.

[12] Systron Donner, "QRS11 User's Guide," 2008.

[13] B. Andresen, C. Grøn, R. Knudsen, C. Nielsen, K. Sørensen and D. Taagaard, "Attitude Control System for AAUSAT-II," Aalbord University, Institute of Electronic Systems, Rep. IAS8–05GR834, 2005.

[14] Systron Donner. *QRS11 High Performance Rate Sensor* [Online]. Available: http://www.systron.com/products/qrs11.

[15] D. Titterton and J. Weston, *Strapdown Inertial Navigation Tech Technology*, Second ed., The Institution of Engineering and Technology, 2005.

[16] E. Okano, "Microelectromechanical systems for small satellite applications," Master's thesis, Naval Postgraduate School, Monterey, CA, 2001.

[17] R.S. Figliola and D.E. Beasley, *Theory and Design for Mechanical Measurements* 4th ed., John Wiley & Sons, Inc., 2006.

[18] *IEEE Standard Specification Format Guide and Test Procedure for Coriolis Vibratory Gyros*, IEEE Std 1431–2004, 2004.

[19] P. Aggarwal, Z. Syed, A. Noureldin and N. El-Sheimy, *MEMS-Based Integrated Navigation (GNSS Technology and Applications)*, Artech House Publishers, 2010.

[20] C. Acar and A. Shkel, *MEMS Vibratory Gyroscopes: Structural Approaches to Improve Robustness (MEMS Reference Shelf)*, 2nd ed.,New York, NY:Springer, 2008.

[21] IEE Ultrasonics, Ferroelectrics, and Frequency Control Society. *Aging Mechanisms* [Online]. Available: http://www.ieee-uffc.org/frequency_control/teaching.asp?vig=agingmec.

[22] P. Groves, *Principles of GNSS, Inertial, and Multi-Sensor Integrated Navigation Systems (GNSS Technology and Applications)*, Boston/London:Artech House Publishers, 2008.

[23] R. Phelps, (Feb. 2010). *MEMS/ACS test plan description.* [Personal E-mail]. Available e-mail:rphelps@nps.edu

[24] D. Sakoda, (April 20, 2010). *Re: Orbit questions.* [Personal E-mail]. Available e-mail:dsakoda@nps.edu

[25] M. Hirata, K. Kokubun, M. Ono and K. Nakayama, "Size effect of a quartz oscillator on its characteristics as a friction vacuum gauge," *Journal of Vacuum Science & Technology A: Vacuum, Surfaces, and Films*, vol. 3, no. 3, pp. 1742–1745 1985.

[26] X. Shi, G. Zhu, Z. Gan and S. Liu, “Vacuum degree measurement of MEMS vacuum package based on DDS,” in *Electronic Packaging Technology, 2006. ICEPT ‘06. 7th International Conference on*, 2006, pp. 1–7.

[27] J. Newman, Private Communication, April 2010.

[28] Wikipedia. (11 July 2011). *Flight dynamics (spacecraft)* [Online]. Available: http://en.wikipedia.org/wiki/Flight_dynamics_(spacecraft).

[29] P. Ghibaudi, D. Fossati and S. Binda, “A three axis rate instrument sensing (TRIS) package based on solid state Coriolis vibrating gyroscopes (CVG),” in *Spacecraft Guidance, Navigation and Control Systems, Proceedings of the 4th ESA International Conference*, ESTEC, Noordwijk, the Netherlands, 2000.

[30] D. Sakoda, (June 2011). *Re: Thesis draft.* [Personal E-mail]. Available e-mail:dsakoda@nps.edu

[31] D. Sakoda, (August 12, 2011). *Re: Finalizing thesis - Questions*. [Personal E-mail]. Available e-mail: dsakoda@nps.edu

[32] H. Hou, “Modeling inertial sensors errors using allan variance,” Master’s thesis, University of Calgary, Calgary, Alberta, 2004.

[33] *IEEE Standard Specification Format Guide and Test Procedure for Single-Axis Interferometric Fiber Optic Gyros*, IEEE Std 952–1997, 1998.

[34] A. Makdissi, “Allan variance MATLAB source code,” 2003. http://www.alamath.com/index.php?option=com_content&task=view&id=19&Itemid=9.

[35] K. Lai, J. Crassidis and R. Harman, “Real-time attitude-independent gyro calibration from three-axis magnetometer measurements,” in *AIAA/AAS Astrodynamics Specialist Conference and Exhibit*, Providence, Rhode Island, 2004.

[36] HAAS Automation Inc., *Rotary Operator’s Manual*, Oxnard, CA, 2009.

[37] "Spectral density,” Wikipedia. (4 May 2011). [Online]. Available: http://en.wikipedia.org/wiki/Spectral_density.

THIS PAGE INTENTIONALLY LEFT BLANK

BIBLIOGRAPHY

[1] Anonymous, *MEMS based attitude and heading reference systems: overview and current trends/ Interview with Per Slycke* [Online]. Available: http://www.memsinvestorjournal.com/2010/12/mems-based-attitude-and-heading-reference-systems-overview-and-current-trends.html.

[2] S. F. Andrews and W. M. Morgenstern, "Initial Flight Results of the TRMM Kalman Filter," in *Proceedings of the AAS/GSFC International Symposium on Space Flight Dynamics,* Greenbelt, Maryland, 1998, pp. 393.

[3] C. Chi and T. Chen, "A gyroscope control system for unknown proof mass and interface circuit errors," in *American Control Conference (ACC), 2010*, pp. 3403–3408.

[4] C. Chi and T. Chen, "MEMS gyroscope control systems for direct angle measurements," in *Sensors, 2009 IEEE*, 2009, pp. 492–496.

[5] E. Dorveaux, D. Vissière, A.P. Martin and N. Petit, "Iterative calibration method for inertial and magnetic sensors," in *Joint 48th IEEE Conference on Decision and Control and 28th Chinese Control Conference,* Shanghai, China, 2009.

[6] N. El-Sheimy, Haiying Hou and Xiaoji Niu, "Analysis and modeling of inertial sensors using allan variance," *Instrumentation and Measurement, IEEE Transactions*, vol. 57, no. 1, pp. 140–149 2008.

[7] T. Flatley, W. Morgenstern, A. Reth and F. Bauer, "A B-Dot Acquisition Controller for the RADARSAT Spacecraft," in *NASA CONFERENCE PUBLICATION*, 1997, pp. 79–90.

[8] Z. Gan, D. Lin, X. Wang, Chenggang, H. Zhang and S. Liu, "Vacuum measurement on vacuum packaged MEMS devices," *Journal of Physics: Conference Series*, no. 48, pp. 1429–89 2006.

[9] K. M. Hangos and L. Leisztner, "The systematic error caused by random errors through data reduction," *J.Automat Chem.*, vol. 9, no. 1, pp. 25–29 1987.

[10] IEEE Aerospace and Electronic Systems Society, "IEEE Standard Specification Format Guide and Test Procedure for Single-Axis Laser Gyros," Institute of Electrical and Electronics Engineers, New York, NY, Rep. IEEE Std. 647–1995, 2006.

[11] J. Sedlak, "Iterative Magnetometer Calibration," in *AAS/AIAA Astrodynamics Specialists Conference*, Keystone, CO, 2006.

[12] B.D. Killough. *NASA LaRC Thermal Testing Philosophy* [Online]. Available: http://tfaws.nasa.gov/TFAWS03/thermal_testing_panel_discussion/tfaws03_thermal_panel_summary_larc.pdf.

[13] K. Lai, J. Crassidis and R. Harman, "Real-Time Attitude-Independent Gyro Calibration from Three-Axis Magnetometer Measurements," in *AIAA/AAS Astrodynamics Specialist Conference and Exhibit,* Providence, Rhode Island, 2004.

[14] K. L. Makovec, A. J. Turner and C.D. Hall, "Design and implementation of a nanosatellite attitude determination and control system," in *Proceedings of the 2001 AAS/AIAA Astrodynamics Specialists Conference,* Quebec City, Quebec, 2001.

[15] F. Martel, P. K. Pal and M. L. Psiaki, "Active Magnetic Control System for Gravity Gradient Stabilized Spacecraft," in *Proceedings of the 2nd Annual AIAA/USU Conf. on Small Satellites,* Logan, UT, 1988.

[16] NASA, "Payload Test Requirements,"Rep. NASA-STD-7002, 1996.

[17] R. Yafei, K. Xizheng and L. Yijie, "MEMS Gyroscope Performance Estimate Based on Allan Variance," in *Electronic Measurement and Instruments, 2007. ICEMI '07. 8th International Conference on,* 2007, pp. 1–260–1-263.

[18] S. Mattila and P. Kuosmanen, "Comparison of Kalman algorithms for MEMS based pitch and roll angle estimation," in *12th IFToMM World Congress,* Besançon, France,2007,.

[19] W. H. Steyn, "A Multimode Attitude Determination and Control System for SUNSAT," in *Small Satellite Systems and Services,* Annecy, France, 1996.

[20] W. H. Steyn and Y. Hashida, "In-orbit attitude and orbit control commissioning of UoSAT-12," *EUROPEAN SPACE AGENCY -PUBLICATIONS- ESA SP*, vol. 425, pp. 95–102 2000.

[21] W. H. Steyn, "A multi-mode attitude determination and control system for small satellites," Ph.D thesis, University of Stellenbosch, 1995.

[22] W. H. Steyn, Y. Hashida and V. Lappas, "An Attitude Control System and Commissioning Results of the SNAP-1 Nanosatellite," in *Proceedings of the 14th Annual AIAA/USU Conference on Small Satellites* Utah State University.

[23] T. Wang, “Multi-sensor extended kalman filter for attitude determination,” M.S. thesis, University of Texas, Austin, TX, 2007.

[24] J.R. Wertz, *Spacecraft Attitude Determination and Control* Dordrecht, Holland:D. Reidel Publishing Company, 1978.

[25] T. Wescott, “Compensating for gyro sensor drift (discussion thread),” Mar 2010. http://www.dsprelated.com/showmessage/124293/1.php.

THIS PAGE INTENTIONALLY LEFT BLANK

INITIAL DISTRIBUTION LIST

1. Defense Technical Information Center
   Ft. Belvoir, VA

2. Dudley Knox Library
   Naval Postgraduate School
   Monterey, CA

3. Mr. James Horning
   Code SP/Jh
   Naval Postgraduate School
   Monterey, CA

4. Professor James Newman
   Code SP/Nm
   Naval Postgraduate School
   Monterey, CA

5. Dr. Rudolph Panholzer
   Chairman of Space Systems Academic Group
   Naval Postgraduate School
   Monterey, CA

6. Mr. Ron Phelps
   Code SP/Rp
   Naval Postgraduate School
   Monterey, CA

7. Mr. Daniel Sakoda
   Code SP/SD
   Naval Postgraduate School
   Monterey, CA

8. Veronica V. Badescu
   Dayton, OH